THE FEASIBILITY OF WHOLE-BODY IN VIVO X-RAY

FLUORESCENCE OF LEAD IN BONE IN MICE

THE FEASIBILITY OF WHOLE-BODY IN VIVO X-RAY

FLUORESCENCE OF LEAD IN BONE IN MICE

By

Tsz Wing Cheung, B.Eng.

A Thesis

Submitted to the School of Graduate Studies

in Partial Fulfillment of the Requirements for the Degree

Master of Science

McMaster University

MASTER OF SCIENCE (2018)   **McMaster University**

(Radiation Sciences Graduate Program)   **Hamilton, Ontario**

TITLE: The Feasibility of Whole-body In Vivo X-ray Fluorescence of Lead in Bone in Mice

AUTHOR: Tsz Wing Cheung, B.Eng. (City University of Hong Kong)

SUPERVISOR: Dr. Fiona E. McNeill

NUMBER OF PAGES: xiv, 102

ABSTRACT

Previous studies have shown an association between Pb exposure and intelligence quotient (IQ). Up until now, there is a lack of technology and methodology to assess the effects of long-term Pb exposure (such as de-myelination) in brain in-vivo. So we are developing a mouse model that will allow us to assess in vivo Pb in bone and brain structure and myelination using magnetic resonance imaging (MRI). In this project, we will discuss the feasibility of an in vivo x-ray fluorescence (XRF) system for the Pb measurement in the skeleton of whole mice.

A review of literature is conducted in chapter 1. Health impacts of lead, measurement of lead, pre-existing bone Pb phantoms and mouse model selection are explained thoroughly.

In chapter 2, calibration and minimum detection limits (MDLs) for the XRF measurements are documented. Calibration was performed using Plaster of Paris phantoms mimicking human bone doped with Pb concentrations ranging from 0 to 100 ppm. Detection limits for the pre-existing bone Pb phantoms were found to be 1.52 μg Pb/g plaster for 1-hour measurement. For 2 strains of Pb free mice (CD-1 and C57BL/6J), which had skull and hind facing detectors respectively, MDLs of 5.66 – 7.78 μg Pb/g and 6.69 – 8.50 μg Pb/g were determined for 3-hour measurement. This detectability of MDLs by the XRF system encourages us to proceed to measure mouse-mimicking phantoms.

In order to evaluate the feasibility of a ^{109}Cd XRF system for the Pb measurement in the skeleton of whole mice, mouse-mimicking phantoms were made and measured. The effect of variations in Pb distribution across the mouse and the applicability of the normalization in mice are discussed in chapter 3.

To sum up, our system can measure Pb in whole mice in vivo at the levels of Pb in bone that are anticipated in brain de-myelination studies. Our results indicate that if multiple orientations (rotated) are measured in mice, the mean bone Pb level in whole mice will be determined accurately.

ACKNOWLEDGEMENTS

TABLE OF CONTENTS

LISTS OF FIGURES

LIST OF TABLES

CHAPTER 1

A Review of the Literature: Health Impacts and Measurement of Lead

In the following subchapters, several topics will be discussed for a better understanding of this project. Heavy metal poisoning will be introduced first with a main focus on lead poisoning. In order to show the hazards from chronic lead poisoning, sources of exposure and lead metabolism will also be mentioned.

In this study, X-ray fluorescence spectroscopy will be employed. These subchapters will highlight this particular measurement technique, e.g. the cloverleaf geometry K-XRF system will be addressed. Lastly, an introduction to existing bone Pb phantoms, and the selection of laboratory mice will be presented.

1.1 Heavy Metal Poisoning

Heavy metal poisoning is a significant public health concern (Lead, WHO Inorganic, 1995). It is defined as the ability to produce toxic effects to the body from certain kinds of metals (CDC, 2012). The lower the toxicity, the larger amount of material that is required to cause harmful effects through absorption. Some health effects can result from relatively small proportions of toxic materials being absorbed. Those metals that have no defined biological role in the body, often affect human health. Health consequences can be defined as either acute or chronic. An acute effect produces an immediate harm while a chronic effect causes a prolonged effect after consumption over a period of time.

Lead (Pb) is the metal of interest in this work and it, for example, can cause irreversible neurological damage, reproductive toxicity and cardiovascular effects in humans (Flora et al., 2012). Chemical forms are also one of the factors for metal toxicity. Lead is distributed in the environment in three main forms, including elemental lead, inorganic lead and organic lead. For example, white lead (a lead carbonate compound), yellow lead (lead chromate, lead monoxide) and red lead (lead tetroxide) are the common examples of inorganic lead (ATSDR, 2017). Absorption of inorganic lead usually takes place in the respiratory and gastrointestinal tracts (Papanikolaou et al., 2005). In comparison, organic lead, such as tetraethyl and tetramethyl lead in gasoline, can be absorbed through skin (Papanikolaou et al., 2005).

1.1.1 Lead Poisoning

Lead (Pb) is a metal that carries a toxic effect (Tong et al., 2000). According to the World Health Organization, lead is a major public health concern and identified as human carcinogen (Jarup, 2003). Other than working in the mining and smelting industries, using lead-based paint and lead pipes in older buildings increases the likelihood of human exposure (Jarup, 2003). Working in the leaded glass industry is another pathway for low or moderate exposure (Jarup, 2003). As Pb has a skeletal half-life that is estimated as more than 25 years (Hu, 1998; Behinaein et al., 2014), accumulation occurs in bone easily and likely in several organs, especially in the kidney, liver and brain (Lead, WHO Inorganic, 1995; Jarup, 2003; Tchounwou et al., 2012). As the body has a limit on its capacity to eliminate heavy metals, those metals accumulate in the body and may have

some negative effects in humans (Lead, WHO Inorganic, 2015). Previous research studies show that there is strong evidence for a link between Pb exposure and several cancers, mainly in liver, kidney, brain and bones (Jarup, 2003; Lead, WHO Inorganic, 2015). Different functional systems are affected by lead exposure, including the reproductive system, the hematopoietic system, the endocrine system and the central nervous system (ATSDR, 1990). The latter is considered the most vulnerable target of lead poisoning especially in children. Loss of memory, poor attention span and headache are early symptoms of chronic lead exposure (ATSDR, 1990; Harvey, 2002).

1.2 Sources of Lead Exposure and Risk Factors

1.2.1 Exposure Duration and Total Dose Absorbed

For the duration of exposure, it could be further classified as acute or chronic. In an acute exposure, a single event happens with dose delivery at a (usually) high concentration. Thus, rapid absorption is facilitated during an acute exposure. Acute lead exposure often results in pain, muscle weakness, coma and convulsions (Pearce, 2007).

On the other hand, if a (relatively) lower dose is delivered over a period of time, this results in chronic exposure. For example, lead-contaminated dust and lead-based paint are two of the most common sources for chronic exposure (Pearce, 2007). Chronic exposure can result in renal failure, headache, sleep disturbance, anaemia (Anderson et al., 1996) and fatigue (Pearce, 2007). Levels of exposure that result in these kinds of health effects are, thankfully, no longer 'normal' in Canada (McNeill et al., 2017).

1.2.2 Age

Age is also a factor in the different severities of toxic effects. Children are considered a sensitive or vulnerable population because of effects on intellectual performance. For example, one previous study has shown an inverse correlation between blood lead concentration (<10 µg/dL) and children's cognitive function (Jusko et al., 2008). In addition, teenagers are considered more sensitive to heavy metal poisoning than adults (Leggett, 1993; Cory-Schlecta and Schaumburg, 2000; Taylor et al, 2013). This is because the percentage of gut absorption in minerals is higher relative to adults (Harvey, 2002; Kalra et al., 2003; Lidsky et al., 2003). This higher absorption causes increased levels in blood and tissues that leads to an interruption in brain development, which is classified as a severe effect from early childhood to adolescence.

1.2.3 Route of Exposure

The route of exposure also plays a paramount role for the toxicity of a heavy metal. There are three primary routes for body entry, namely inhalation, absorption and ingestion (Mann et al., 1982). Inhalation is defined as certain substances that enter lungs through breathing. After the process of breathing in, the substance originally in the air is in ready contact with the lung blood vessels. As a result, it can be absorbed and cause detrimental effects in the person. Absorption is a term that describes physical contact between the substance and a body surface leading to entry into the body. An example is tetraethyl lead, which, as has been know for decades, can be absorbed extremely readily through the skin (Rastogi et al., 1976). Ingestion is defined as a material that enters the body by

swallowing. Eating in a working area where lead is used may then enhance the chance of toxic material ingestion.

1.3 Lead Metabolism

The metabolism of lead is complex (Leggett, 1993; Cory-Schlecta and Schaumburg, 2000). In general, in environmental exposures, Pb enters human body by absorption through ingestion or inhalation. Pb can be accidentally ingested and enter the gastrointestinal tract (GI tract). There is a possibility that lead can then enter the blood vessels of the small intestine in the lower GI tract.

On the other hand, for industrial exposures, lead contaminated dust can be inhaled, and 35 to 40% of inhaled dust can be deposited in the ends of the respiratory tree (the pulmonary alveoli) in lung (Lohiya et al., 1995). The main function of the pulmonary alveoli is the gas exchange with the blood. Approximate 95% of deposited lead in the lungs thus enters blood vessels. The remaining 5% of deposited lead particles are cleared by the lungs can be swallowed and result in further absorption from the GI tract.

Most pathways into the human body lead to the blood. However, the half-life of lead in blood is relatively short (~35 days) (Markowitz, 2000), lead is either excreted or passed to other organs for storage, and we can simply conclude that blood lead is a short-term biomarker in exposure measurement.

As opposed to the short-term biomarker of blood lead, bone lead is considered a marker of long-term exposure. Lead is a bone-seeking element, and about 40 to 50% of lead from blood ends up stored in bone. The remaining blood lead is filtered by the

kidneys and undergoes excretion. There are two ways for the excretion of absorbed (organic and inorganic) lead, in the urine and in faeces (biliary secretion) (IARC, 2006). By filtration and reabsorption, the rate of excretion in the urine is proportional to the lead concentration in plasma (IARC, 2006). Biliary excretion in human has been reported to be between 25 to 50% of urinary excretion (IARC, 2006). For organic lead, exhalation from the lung also contributes a major route of excretion. For reference, 40% of tetramethyl lead and 20% of tetraethyl lead of the dose are exhaled at 48 hours after inhalation (IARC, 2006). The resulting long-term proportions of lead burden in adults are: 95% in bone, 4% in brain, liver and kidneys and 1% in blood (Pearce, 2007).

As 95% of total lead burden in adults stored in bones (O'Flaherty, 1998), bone lead concentration becomes the focus when studying the impact of chronic lead poisoning, because it can be a marker of long-term Pb exposure. In this thesis, the focus is therefore on the measurement of bone, because we are interested in the development of a system for assessing cumulative or long-term exposure in mice. The system development started with the analysis of a set of existing human bone Pb phantoms and moved on to the development of mouse mimicking bone Pb phantoms for use in the ^{109}Cd K XRF bone Pb system. The potential application of the system will be addressed in the concluding remarks of this work.

1.3.1 Half-life and Retention of Lead in Bone

The biological half-life of lead in bone varies in different types of cortical and trabecular bones (Gerhardsson et al, 2005). Cortical and trabecular bones make up about 80% and

20% of the skeleton respectively. Trabecular bones have a shorter half-life and vary from several years in vertebrae (Schütz et al., 1987) to 16 years in calcaneus (Gerhardsson et al., 1993). In contrast, it is reported that cortical bones often have half-lives in a range of 5 to 25 years (Gerhardsson et al., 1993; Christoffersson et al., 1984 and 1986; Price et al., 1992; Nilsson et al., 1991; Börjesson et al., 1996; Todd et al., 2001). These cross-sectional studies data are summarized by Chettle, 2005 and shown in Table 1.1.

Reference	Exposure status	Bone	Half-life (years)	95% confidence interval (years)
Nilsson et al., 1991	Retired	Phalanx	16	12-23
Gerhardsson et al., 1993	Active + retired	Calcaneus	16	11-19
		Tibia	27	16-98
Börjesson et al., 1996	Active	Phalanx	5.3	3.3-13
Brito et al., 2000	Active	Tibia	15	9-55

Table 1.1. Estimates of half-lives of lead in bone (Chettle, 2005).

1.3.2 Relationships between Lead Level in Bone and Age

Participants who are older than 50 years of age have the highest Pb concentrations in tibia and calcaneus bones (Behinaein et al., 2017). Plots of average tibia Pb content and calcaneus Pb content against average age for each of the measurement age groups are also presented by McNeill et al, 2017 and shown in Figure 1.1A and Figure 1.1B. Both average tibia lead content and calcaneus lead content increase linearly above the age of 20 to the age of 60 (McNeill et al, 2017). For reference, a linear regression of tibia lead content versus age, in adults over the age of 20, suggests that the lead content of the tibia increases by 0.16 ± 0.03 μg Pb g^{-1} bone mineral per year of age ($p < 0.001$) with a y intercept of $- 3.5 \pm 1.6$ μg Pb g^{-1} bone mineral ($p = 0.03$) (McNeill et al, 2017). And a linear regression of calcaneus lead content versus age, in adults over the age of 20,

suggests that the lead content of the calcaneus increases by 0.27 ± 0.07 μg Pb g^{-1} bone mineral per year of age (p < 0.001) with a y intercept of -5.1 ± 3.5 μg Pb g^{-1} bone mineral (p = 0.14) (McNeill et al, 2017). The results from this latest study are comparable to the previous studies (Gamblin et al 1994, Roy et al 1997, McNeill et al 2000).
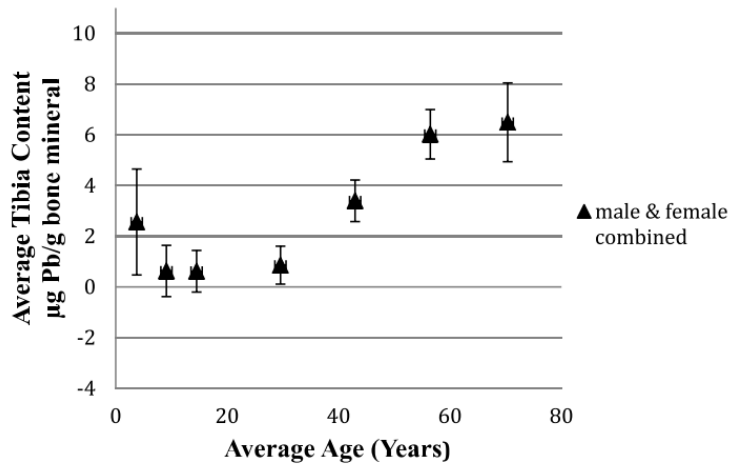
Figure 1.1A: Plots of average tibia Pb content against average age for each of the measurement age groups with data from male and female participants combined. Error bars in figure indicate standard error of the mean (McNeill et al., 2017).
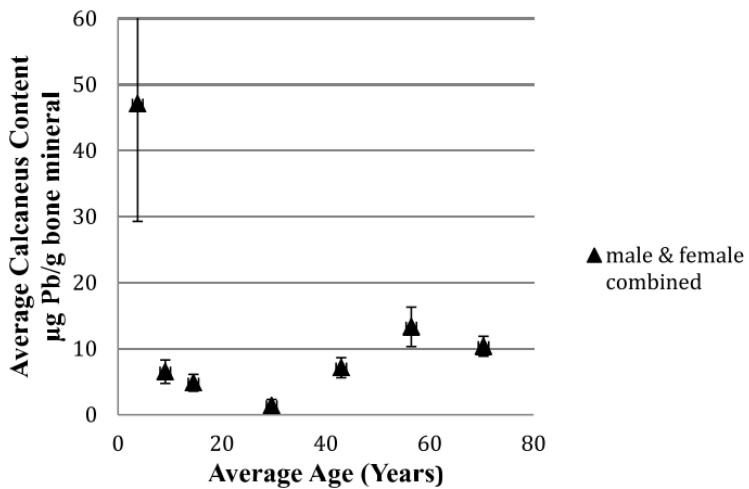
Figure 1.1B: Plots of average calcaneus Pb content against average age for each of the measurement age groups with data from male and female participants combined. Error bars in Figure indicate standard error of the mean (McNeill et al., 2017). High calcaneus Pb levels are found in children younger than 6, and possible reasons are higher bone turnover in early childhood, measurements in mixture of bones and maternal lead status (McNeill et al., 2017).

1.3.3 Endogenous Exposure and Release of Lead from Bone

Endogenous exposure refers to stored lead from bone being released back into blood. This causes an individual's current blood lead to be raised above the reference of blood lead. A significant correlation between current blood lead and bone lead has been observed in different studies among retired lead workers. These endogenous exposure findings are summarized by Chettle, 2005 and shown in Table 1.2 and Table 1.3. For example, using Fleming et al, 1997 data, current blood lead (B) could be found by the following equations,

$$\text{Current Blood Lead (B)} = 0.136 \times \text{tibia Pb} - - - (1.1)$$

$$\text{Current Blood Lead (B)} = 0.078 \times \text{calcaneus Pb} - - - (1.2)$$

Linear regressions between (endogenous) blood lead and bone lead for tibia and calcaneus are shown (Chettle, 2005). These results show important consequences that a person who has accumulated bone lead stores through working in a lead-exposed environment for two or three decades will maintain a blood lead level significantly raised compared to the general population, even after occupational exposure has ceased (Chettle, 2005).

Reference	Slope [μg Pb dl^{-1}/ μg Pb (g bone mineral) $^{-1}$]	Intercept (μg Pb dl^{-1})
Erkkila et al., 1992	0.133	5.3
Gerhardsson et al., 1993	0.138	7.7
Bleeker et al., 1995	0.170	13.0
Fleming et al., 1997	0.136	13.0

Table 1.2. Blood lead concentration versus tibia lead concentration in retired workers (Chettle, 2005).

Reference	Slope [μg Pb dl^{-1}/ μg Pb (g bone mineral) $^{-1}$]	Intercept (μg Pb dl^{-1})
Erkkila et al., 1992	0.072	4.0
Gerhardsson et al., 1993	0.062	6.9
Fleming et al., 1997	0.078	13.0

Table 1.3. Blood lead concentration versus calcaneus lead concentration in retired workers (Chettle, 2005).

1.4 Health Effects of Lead

1.4.1 Lead and Harm

Because of the high degree of toxicity, according to the International Agency for Research on Cancer and U.S. Environmental Protection Agency, lead is classified as human carcinogen. Even a chronic low-level lead exposure has been identified as harmful in human beings (Schwartz, 1994; Canfield et al., 2003; Lanphear et al., 2005; Menke et al., 2006; Jusko et al., 2008; Rasmussen et al., 2013). In general, the incidence of children with intellectual disorders and adults with cardiovascular diseases have been found to be correlated to the chronic low-level Pb exposure (Schwartz, 1994; Lanphear et al., 2005; Navas-Acien et al., 2007).

1.4.2 Lead and De-myelination

The nervous system is composed of two parts: the central nervous system (CNS) and peripheral nervous system (PNS). The CNS includes the brain and spinal cord, while PNS represents the nerves that lead to or branch off from CNS.

Lead affects the function of central nervous system and peripheral nerves. The most disruptive action of Pb is described as follows. Due to the ability to substitute for calcium ions (Ca^{2+}), lead ions (Pb^{2+}) pass through the blood-brain barrier (BBB) and concentrate in the brain (BrPb) (Sanders et al., 2009). Picomolar concentrations of Pb^{2+} replace micromolar concentrations of Ca^{2+} in a protein kinase C (PKC) enzyme assay, and this is a calcium-dependent process (Markovac et al., 1988; Bressler at al., 1991 and 1999). Because lead can mimic or mobilize calcium and PKC, behavior of endothelial cells in the immature brain may be altered and eventually BBB may be disrupted (Goldstein, 1993; Bressler et al., 1994; Finkelsten et al., 1998). Disruption of BBB can lead to impaired function of the BBB, and hence compromising the Central Nervous System (CNS) (Hawkins et al., 2005; Persidsky et al., 2006).

Other possible sites of action of lead in neurons are illustrated by Finkelstein et al., 1998 and shown in Figure 1.2. Places of lead interactions are: (1) voltage-gated channels; (2) neurotransmitters (first messenger systems); (3) second messengers; (4) protein kinases; (5) third messenger systems; (6) DNA repair. These interactions are summarized in the following table.
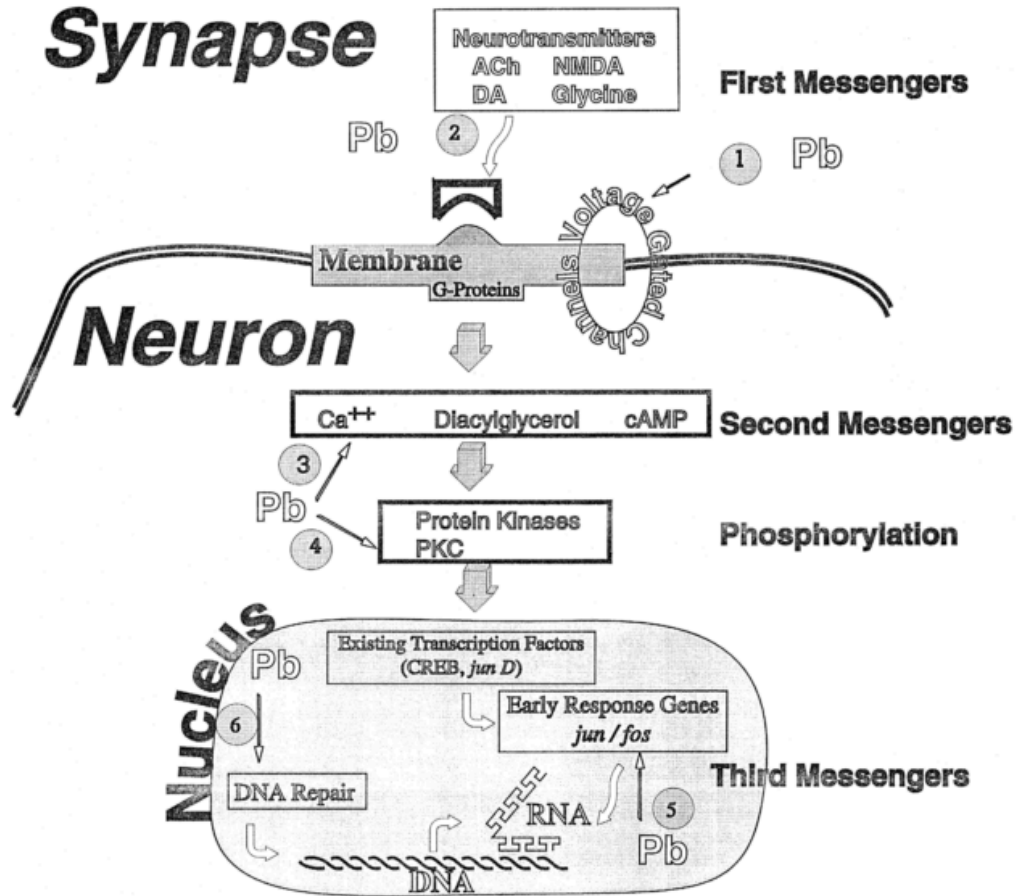
Figure 1.2: Possible sites of Pb interactions in neurons from: Finkelstein, Yoram, Morri E. Markowitz, and John F. Rosen. "Low-level lead-induced neurotoxicity in children: an update on central nervous system effects." Brain Research Reviews 27.2 (1998): 168-176, doi: https://doi.org/10.1016/S0165-0173(98)00011-3.

Possible Site of Pb Interactions		Mechanisms
1	Voltage-gated channels	Pb^{2+} directly blocks Ca^{2+} conductance. It also competes with Ca^{2+} for access to the channels.
2	Neurotransmitters (first messenger systems)	Pb acts as a chemical stressor and affects the modulation of emotional responses, memory and learning (Finkelstein et al., 1998). It also acts as a non-competitive antagonist of the glycine site

		(Ishihara et al., 1995). Previous studies have shown that animals exposed to lead were hypersensitive to systemic administration of N-methyl-D-aspartate (NMDA) (Petit et al., 1992).
3	Second messengers	Pb mimics or mobilizes calcium and activates PKC in endothelial cells (Bressler et al., 1991).
4	Protein kinases	
5	Third messenger systems	Pb alters specific metal-dependent transcription factors such as zinc-finger proteins (Cory-Slechta et al., 1995).
6	DNA repair	Pb inhibits DNA repair and exerts indirect genotoxic effect, such as acting as a co-mutagenic agent with ultraviolet radiation or alkylating agaents (Beyersman, 1994).

Table 1.4. Impacts of lead on biological activities at different intracellular levels.

Encephalopathy is the most severe situation of lead poisoning. It is neurological changes that characterized by brain edema, demyelination of the cerebral and cerebellar white matter as well as demyelinating peripheral neuropathy (Landrigan et al., 1994; Singh et al., 2009; Mani et al., 1998). It is inevitable at very high doses of exposure and is frequently seen in young children (Mason et al., 2014). Symptoms of lead encephalopathy include headaches, irritability, memory deficits and even progress to paralysis, coma and death (Kumar et al. 1987). Previous studies have shown lead encephalopathy in brain with computed tomography (CT) and magnetic resonance imaging (MRI) findings (Tüzün et al., 2002; Rao et al., 2014).

Lead exposure also causes axonal degeneration and segmental demyelination (Jeyaratnam et al., 1985). Previous researches have also shown that lead slows down the cognitive development (Koller et al., 2004) by disruption proper neuronal migration (Sibergeld, 1992), synapse formation (Bressler et al., 1991) and glial cell differentiation (Cookman et

al., 1987). In addition to the decreased brain volume found in young adults who had raised lead concentrations in their blood during childhood (Cecil et al., 2008), neurodegenerative changes have also shown on MRI (Stewart et al., 2006).

In order to detect early neurological abnormalities, measurement of the distal latency is necessary and hence nerve conduction velocities (NCV) are studied. According to the World Health Organization (WHO), reduction in human nerve conduction velocities (NCV) may occur with the blood lead level (BLL) as low as 30 µg/dL. With an increased lead absorption, reductions in peripheral nerve conduction velocities (NCV) in workers have been shown in lots of studies and indicate that the nerve conduction velocities are sensitive to lead exposure (Seppäläinen et al., 1975; Araki et al., 1976; Repko et al., 1978; Buchthal et al., 1979; Bordo et al., 1982; Seppäläinen et al., 1983; Singer et al., 1983; Zi-qiang et al., 1985).

1.5 Measurement of Lead

1.5.1 Blood Lead Levels

Lead can be measured by analysis of whole blood: the analysis of both venous blood (venipuncture) and finger stick measurements (finger puncture) have been tried. Both experiment protocols follow the recommendations of the NCCLS' and CLSI' subcommittee on collection of blood specimens, but blood from pricked fingers can get contaminated with environmental lead and hence additional procedures are required. In particular, methods such as using powder-free latex gloves, washing hands vigorously

with soap and applying a thin film of silicone are necessary to avoid potential contamination (Parsons et al., 1997).

In the 1970s, determination of Pb in blood was carried out by methods including electrothermal atomic absorption spectrometry (ETAAS) or Anodic Stripping Voltammetry (ASV) (Parsons et al., 1993 and 1998). Both methods have been validated against different national and international blood Pb reference materials, including the NIST, the Commission of the European Communities, Community Bureau of Reference, Belgium, and the CDC Blood Lead Laboratory Reference System (Parsons et al., 1997). However, the acceptability criteria for blood lead measurements were changed from ±4 μg/dL (CLIA, 1988) to ±2 μg/dL (CDCP, 2012) for individual samples. While the majority of laboratories measuring blood lead were already having errors of ±2 μg/dL (Parsons et al., 2001), newer technologies with lower method limits of detection and improved accuracy are required. Inductively coupled plasma mass spectrometry (ICP-MS) was introduced in the 1990s, and newer generations of ICP-MS have higher sensitivity and lower background levels. In 2013 to 2014 National Health and Nutrition Examination Survey (NHANES) period, the CDC's Environmental Health Laboratory in the National Center for Environmental Health (EHL-NCEH) achieved limits of detection of blood lead of 0.07 μg/dL with a combination of optimized measures (Caldwell et al., 2017). The measures include CDC's ICP-MS analytical method timing, calibrator placement, calibration regression type, sample introduction system, and reagent composition (Caldwell et al., 2017).

According to the report from Health Canada published in 2013, the blood lead levels (BLLs) in Canadians aged 6 to 79 have declined by over 70% since 1978-1979, from 4.79 μg/dL to 1.34 μg/dL (Bushnik et al., 2010). However, there are no national Canadian BLL data for children under 6 years of age currently (Health Canada, 2013). Given the BLLs similarity of BLLs between Canada and U.S. for other age groups, NHANES BLL data are a reasonable substitute for BLLs in Canadian children under 6 years of age (Health Canada, 2013). In 2007-2008 NHANES, the geometric mean and 95th percentile BLLs for children aged 1 to 5 are 1.51 μg/dL and 4.10 μg/dL respectively (U.S. CDC 2011). Study has shown that even low BLL (2 μg/dL) may raise a concern (Gilbert et al., 2006). According to Centers for Disease Control and Prevention (CDC), children with BLL of concern may result in behavioral, academic and potential cognitive problems. Lewis et al., 2018 has found that lead exposure (elevated BLL) affects the language development at early childhood. Nutrition is a factor contributing to growth. Nutritional deficiencies, such as zinc, copper, phosphorus, iron and calcium, enhance the lead absorption in blood and bone (Mahaffey, 1981; Danford, 1982). Elevated BLL results in impaired growth in children (Schwartz et al., 1986).

1.6 Interactions of X-ray with Matter

X-rays photons are particles of x-ray energy and they can be produced by an x-ray tube. In general, photons are neutral and penetrate some distances in a matter before having any interactions with atoms. Penetration distance varies with the energy of photon and interacting target matter. Photons can be absorbed or scattered after interacting with

matter. There are four primary interactions of x-ray photons with matter, and they are: photoelectric absorption; Compton scattering; Coherent scattering and pair production.

1.6.1 Photoelectric Absorption

An incoming photon interacts with an absorber atom. This incoming photon disappears completely and an energetic photoelectron is ejected from one of the bound shells of the atom. This process is called photoelectric absorption. Energy is conserved, as the total energy remains constant throughout the interaction. The ejected photoelectron with an energy E_{KE} could be described by the following equation,

$$E_{kE} = E_\gamma - E_{BE} --- (1.3)$$

where E_γ is the incident photon energy and E_{BE} is the binding energy of the photoelectron in its original shell.

In addition to the photoelectron, an ionized absorber atom also creates a vacancy in one of its bound shells. By the electrons' rearrangement from other shells of the atom, this vacancy is filled quickly and a free electron is captured from the medium. Hence, one or more characteristic x-ray photons may be generated. Kα x-ray is ejected when an electron jumps from L shell to the vacancy of K shell ($E_{K\alpha}=E_{BK}-E_{BL}$). On the other hand, when an electron jumps from M shell to the vacancy of K shell ($E_{K\beta}=E_{BK}-E_{BM}$), Kβ x-ray is ejected. Lα, Lβ, Mα and Mβ x-rays are in a similar situation to the L and M shells. X-ray energy is determined by the binding energies of atomic electron shells, which is determined by the charge on the atomic number. Hence, by measuring the energy and

activity of the characteristic x-rays, we can determine the type and concentration of the element. And this is the principle of XRF measurement.

1.6.2 Compton Scattering

Compton scattering takes place when an incident photon interacts with an electron in the absorbing materials. Incoming photon is deflected by an angle θ with respect to its original direction, and it transfers a portion of its energy to the electron. This electron is later known as a recoil electron. The energy transferred to the electron can vary from zero (when $\theta = 0$) to a portion of the photon energy (i.e. 25.6% at $\theta = 180°$ for 88 keV photons (Nie, 2001). Given an assumption that electrons are free and at rest, we can calculate the scattered photon energy/energies by the following equation (Knoll, 2010),

$$E'_\gamma = \frac{E_\gamma}{1 + \alpha(1 - \cos\theta)} \ggg hv' = \frac{hv}{1 + \frac{E_\gamma}{mc^2}(1 - \cos\theta)} ---(1.4)$$

where $E_\gamma = hv$ is the energy of incident photon, $E'_\gamma = hv'$ is the scattered photon energy, θ is the photon scattering angle, and $\alpha = \frac{E_\gamma}{mc^2}$ in which mc^2 is the electron rest mass energy.

As Compton scattering is a dominant spectral feature for the *in vivo* XRF analysis of bone, geometry and source energy should be considered for minimizing this effect.

1.6.3 Coherent Scattering

Coherent scattering is another scattering process in which a photon interacts with all the electrons of an absorber atom. Coherent scattering is more likely with low energy

photons, and the probability increases with high atomic number Z materials and at small angles with respect to the incident photon direction. The cross section of coherent scattering is determined by the following equation,

$$\partial\sigma = \frac{1}{2}r^2(1 + \cos^2\theta)|F(x,Z)^2|\partial\Omega - - - (1.5)$$

where r is the radius of classical electron, θ is the scattering angle and $F(x,Z)$ is the atomic form factor, which depends on photon energy E, scattered angle θ and atomic number Z.

At very small scattering angles, the cross section varies with Z^2. The Z dependence become dominant at large scattering angles; when the angle is between 120 and 180 degrees and in the energy range of the order of 60 to 100 keV, the cross sections can vary with Z^5 or Z^6 (Chettle et al., 1991). Hence, high Z elements contribute the major source of coherently scattered photons at large scattering angles. This is important for having normalization in determining lead concentration in bone.

1.6.4 Pair Production

Pair production occurs when gamma-ray energy is at least twice the electron rest-mass energy (1.02 MeV), $hv \geq 2mc^2$. In this interaction, the photon disappears and an electron-positron pair is created. As this interaction would never happen for [109]Cd γ-ray induced lead x-rays, details are not disclosed here.

1.6.5 Lead K-shell X-ray Characteristic

The XRF system is a [109]Cd source induced K-XRF system (Gordon et al., 1993). The source has a half-life of 461.4 ± 1.2 days and emits gamma rays of 88.034 keV through decay (Helene et al., 2007). Because the energy threshold of the K shell absorption edge in lead is 88.008 keV, 88.034 keV gamma rays are slightly above the limit. This maximizes the photoelectric cross section and, the probability of electron ejection.

In theory, incident gamma rays interact with a K-shell electron of the target lead material. This electron is then ejected and a vacancy appears in the K-shell. Hence, electrons originally from M-shell or L-shell jump and fill this vacancy. Energy is then released in the form of $K\alpha$ (from L-shell) or $K\beta$ x-rays (from M-shell) (fluorescence yield = 96.7%), or Auger electrons. Fluorescence yield ω_i is the ratio of number of emitted x-rays to the total number of ionizations, where i indicates the electronic shell involved. The fluorescence yield for K, L and M x-rays as a function of atomic number is shown in Figure 1.3.
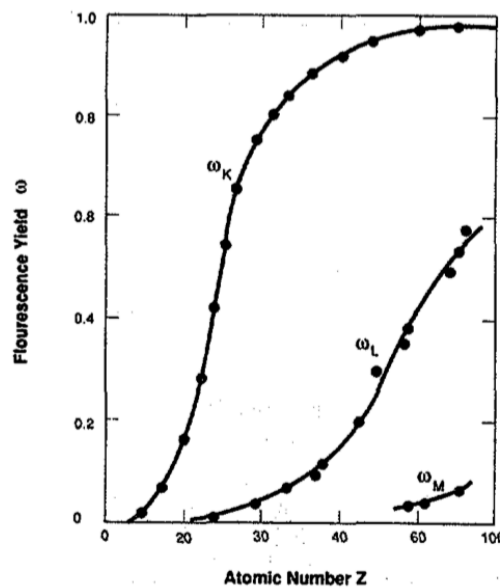
Figure 1.3: Fluorescence yield for K, L and M x-rays as a function of atomic number from Miller, M. C. X-Ray Fluorescence, www.lanl.gov/orgs/n/n1/panda/00326405.pdf. Fluorescence yield increases with atomic number and is greater than 95% for K x-rays of elements such as Pb, with atomic number greater than 78.

The energy and relative intensity of lead K x-rays are described in the following table.

K x-rays	$K\alpha_2$	$K\alpha_1$	$K\beta_3$	$K\beta_1$	$K\beta_2$
Energy (keV)	72.804	74.969	84.450	84.936	87.367
Relative intensity (%)	29.17	49.19	5.7	10.92	5.02

Table 1.5. Energy and relative intensity of the respective lead K x-rays.

As shown in Table 1.5, we can see that the $K\alpha_{1\ or\ 2}$ peaks have significantly larger relative intensities than the $K\beta$ peaks. However, as both of the Pb $K\alpha$ peaks are located closer to the main Compton feature, in our ^{109}Cd K XRF backscatter geometry, we have to take the effect of Compton scattering into account.
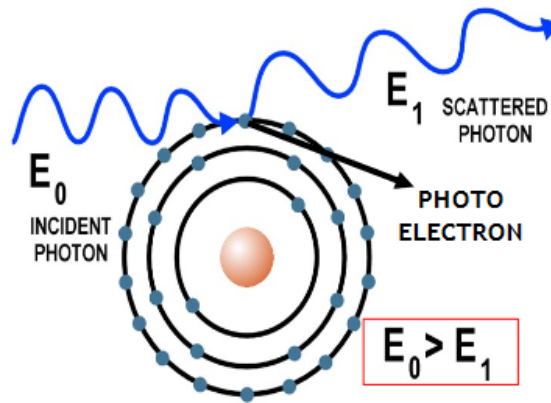
Figure 1.4: Compton scattering, adapted from Thermo Scientific Quant'X EDXRF training manual.

As mentioned in section 1.6.2 Compton scattering, we can calculate the scattered photon energy/energies, with an assumption that electrons are free and at rest (Knoll, 2010),

$$E_1 = \frac{E_0}{1 + \frac{E_0}{mc^2}(1 - \cos\theta)} \; - - - \; (1.6)$$

where E_0 is the incident photon energy, E_1 is the Compton scattering photon energy, θ is the photon scattering angle, and mc^2 is the electron rest mass energy.

As a mean scattering angle of 153.25 degree backscatter is used (Todd et al., 1992), Compton scattered photons have mean energy in the distribution of 66.5 keV. In Compton scattering, there is a momentum distribution to the bound electrons, and this feature with a mean energy of 66.5 keV peak is further broadened by Doppler effect. The Doppler broadening of the Compton scatter feature results in a relatively large background under the $K\alpha_1$ and $K\alpha_2$ peaks.

A large background under x-ray peaks is unfavorable for precise peak analysis, because it increases the uncertainty on the peak area, and the background itself is subject to Poisson statistics. While the $K\alpha$ peaks are more intense, they sit on a large background. The $K\beta_1$ and $K\beta_3$ meanwhile have smaller underlying backgrounds but also smaller peak intensities. Low intensity x-rays are also a challenging issue for peak analysis.

In our study, we analyze both the $K\alpha$ and $K\beta$ peaks in bone lead phantoms in different concentrations. This will be discussed in later Chapters. Figure 1.5 shows a spectrum of an XRF measurement with a Pb concentration of 100 ppm in a pre-existing

bone phantom. From this partial spectrum, we can readily distinguish the $K\alpha$, $K\beta$ and coherent peaks. The spectra fitting methods will be further discussed in Chapter 2.
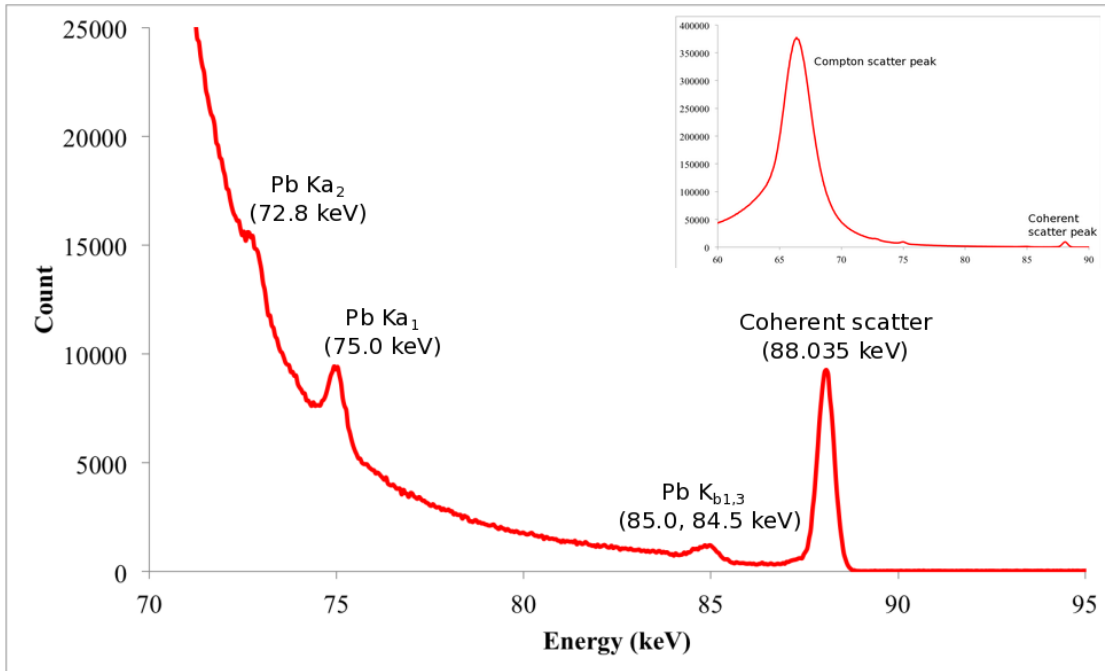
Figure 1.5: Target peaks for the XRF bone lead phantom measurement.

1.7 X-ray Fluorescence Spectroscopy (XRF)

X-ray fluorescence spectroscopy (XRF) is a well-developed technology for elemental and chemical analysis (Potts, 1987; Cesareo et al., 2010). By using this technology, elements in materials are measured and ideally shown in their proportions. Specific energy photons are emitted from unique atoms of material during analysis and the number of specific energy X-ray photons can be used to determine the respective elemental concentration.
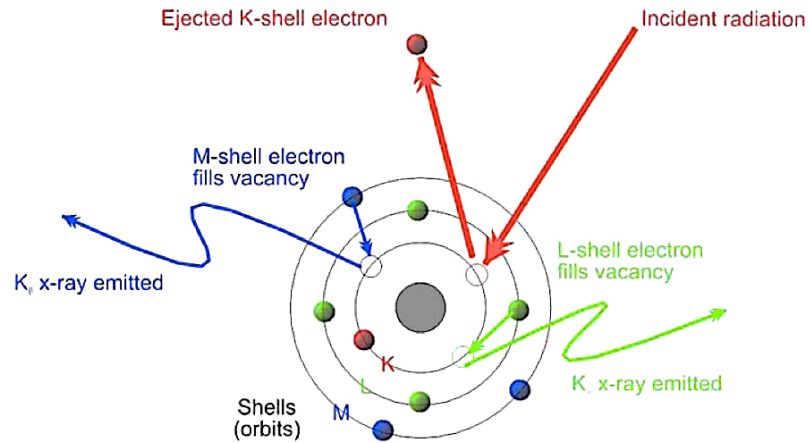
Figure 1.6: X-ray Fluorescence Spectrometry (XRF).

XRF has been used to examine various environmental and biological samples, such as rice grain (Bamford et al., 2004; Paltridge et al., 2012), fingernails (Fleming et al., 2017) and bone (Somervaille et al., 1985; Chettle et al., 1991; Todd et al., 1992; Gerhardsson et al., 1993; Todd et al., 1994; Chettle, 2005).

1.7.1 Energy Dispersive and Wavelength Dispersive

There are two types of X-ray fluorescence spectroscopies, which are energy dispersive spectrometry and wavelength dispersive spectrometry (Beckhoff et al., 2007). Wavelength and energy are measured respectively as the X-ray intensity.

For the wavelength dispersive spectrometry, a sample is irradiated with primary X-rays initially, and fluorescent X-rays are emitted and monochromated by a spectroscopic device. An analysing crystal (Bragg diffracting crystal) is used for the separation of fluorescent X-rays from sample. A detector, such as proportional counter or scintillation counter, is used to detect these monochromatic X-rays.
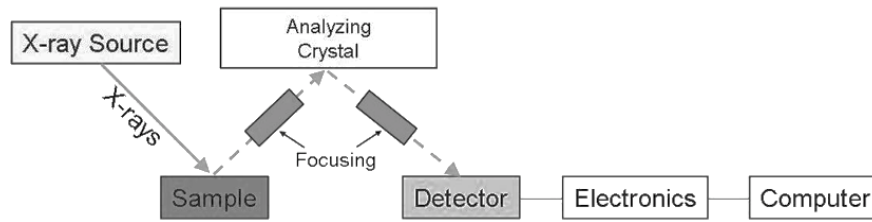
Figure 1.7: A schematic diagram of wavelength dispersive spectrometry.

For the energy dispersive spectrometry, only one area is different from the wavelength dispersive instrument. A monochromator is not used. Instead, a range of x-ray energies is detected. The energy range of the x-rays to be analysed will determine the choice of solid state detector, such as PIN diode, Si(Li), Ge(Li) and Silicon Drift Detector (SDD). The rest of the operating principles follow those of the wavelength dispersive spectrometry (Potts et al., 1987).

1.7.2 Reasons for Conducting XRF

X-ray fluorescence (XRF) is well suited in studying elemental concentrations in hard tissues like bone. It has been used to examine archaeological bones (Carvalho et al., 2000), teeth (Bloch et al., 1998; Zaichick et al., 1999; Carvalho et al., 2000) and hair (Eltayeb et al., 1989; Kolmogorov et al., 2000; Toribara et al., 2001).

There are several advantages for using XRF to study lead concentration in bone. XRF is a non-destructive technique throughout the analysis. Non-destructive means there is no sample damage throughout the measurement process. XRF can also examine various

shapes of samples and requires minimal sample preparation. It is also sensitive to other elements in bone such as strontium, iron and zinc. (Zaichick et al., 1999; Kolmogorov et al., 2000). XRF can be used also to study the heavy metals poisoning in animal tissues such as those of the liver, kidney (Shenberg et al., 1994; Börjesson et al., 1995) and muscle.

1.8 [109]Cd-based K XRF System for Measurement of Lead

1.8.1 System Setup

The system setup and design is based on an earlier optimized system, sometimes described as the 'conventional' system (Gordon et al., 1993). It consists of a HPGe detector (GL0210R/S; Canberra Industries, Canada) which is cooled with liquid nitrogen, a charge sensitive preamplifier, a linear amplifier, an analog to digital converter and a PC based Canberra System 100 multi-channel analyzer. The resolution for the HPGe detector is around 750 eV for 88.035 keV with 1 μs shaping time (Nie, 2001). The preamplifier is used to extract the signal from detector without significantly degrading the intrinsic signal-to-noise ratio. And the linear amplifier has three functions, it magnifies the amplitude of preamplifier output pulse from mV range to the 0.1 ~ 10 V range, optimizes the energy resolution and minimize the overlap between successive pulses.

1.8.2 Cloverleaf Geometry

In 2005, Huiling Nie developed an improvement upon the 'conventional' system by using a cloverleaf geometry at McMaster University. While it follows described setup for the

'conventional system', four small HPGe detectors are used instead of a single detector. The radius of each these detectors is 8 mm. A horizontal cross-section of the cloverleaf detectors system is illustrated in Figure 1.8. The source is mounted and in the center of the four detectors. The minimum detector-source distance is about 16 mm, including the detector-window distance (5 mm), source holder length (6 mm), tungsten backing on source holder (2 mm), thickness of tungsten collimator (2 mm) and the sleeve plastic cover (1 mm). More details will be discussed in next section 1.8.3 Experimental Setup.
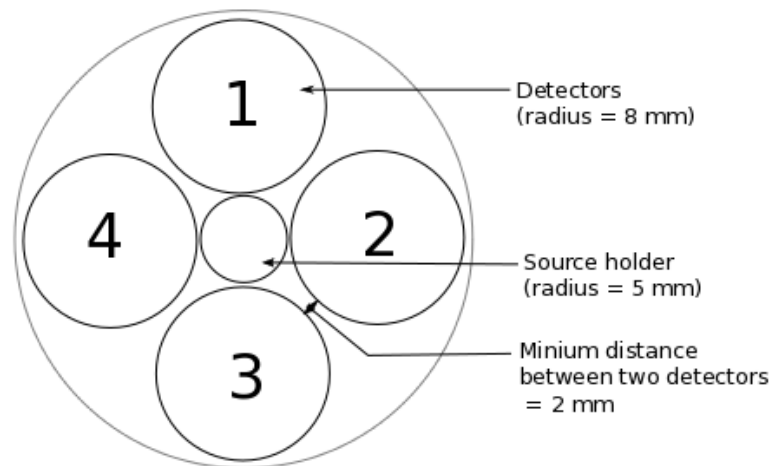
Figure 1.8: Cloverleaf system setup. 4 HPGe detectors are used in single measurement.

1.8.3 Experimental Setup

A close-up of a pre-existing 'human' bone lead phantom measurement is presented in Figure 1.9. The distance between bone lead phantom and detector is about 5 mm.

Figure 1.9: A close-up of the existing bone lead phantom measurement.

Another example photograph of a C57BL/6J mouse measurement is presented in Figure 1.10. The weight of a mouse is about 20 ± 1 grams. The length and width of a mouse are 140 mm and 20 mm respectively. Mouse measurements will be discussed in detail later in this thesis.
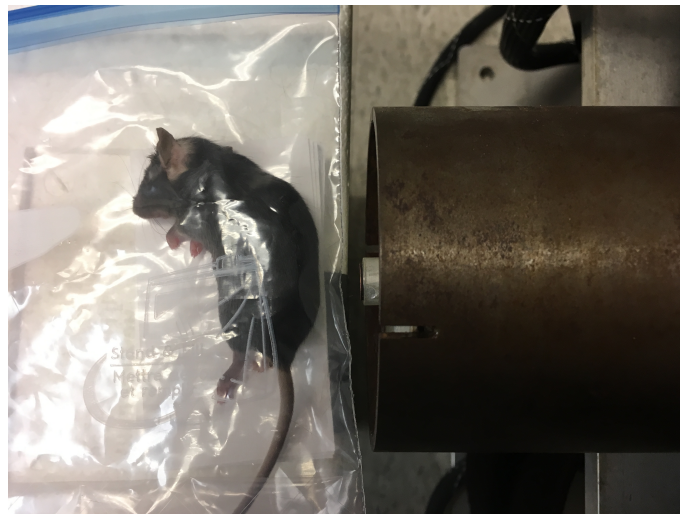
Figure 1.10: A photograph of a C57BL/6J mouse measurement. The distance between the mouse and detector is about 5 mm.

Schematic top view of mouse-mimicking phantom measurement is shown in Figure 1.11. The minimum detector-source distance is about 16 mm, and the minimum detector-phantom distance is about 21 mm. Table 1.6 shows the XRF system components.
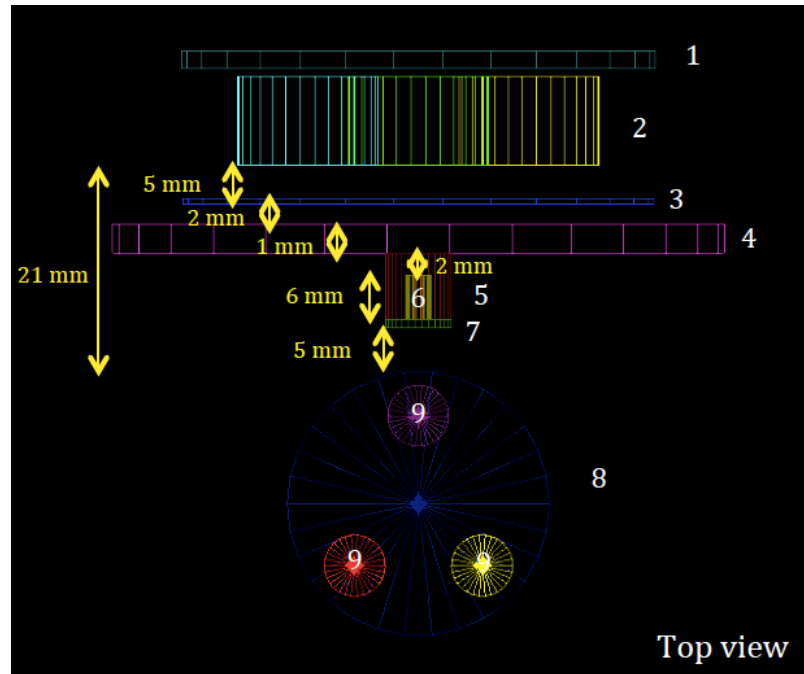
Figure 1.11: Schematic top view of mouse-mimicking phantom measurement.

No.	Components	Radius
1	Beryllium backing window	27 mm
2	Germanium detectors	8 mm each
3	Beryllium window	27 mm
4	Detector face	37.5 mm
5	Source holder // Tungsten collimator	5 mm // 3.75 mm
6	Cd-109 source	1.5 mm
7	Copper filter	3.75 mm
8	Mouse-mimicking phantom	15 mm
9	Plaster of Paris 'bones'	3.5 mm each

Table 1.6. XRF system components.

1.9 Existing Bone Pb Phantoms

A set of pre-existing bone Pb phantoms was made several years ago for calibration of the system for human bone measurements. The composition of phantom is a mixture of Plaster of Paris ($CaSO_4.2H_2O$, PoP) with specific lead concentration. The radius and height of these phantoms are 25 mm and 100 mm respectively. Figure 1.12 shows the available range of different lead concentrations in existing bone Pb phantoms. In our study, we used these pre-existing bone phantoms with 10 different lead concentrations, including 0, 4.2, 8.4, 12.6, 16.8, 21.08, 30, 70 and 100 ppm. These existing bone Pb phantoms used for x-rays peaks calibration, to develop calibration lines used for the minimum detection limits (MDLs) calculation of mice in the K-XRF system. This will be discussed in more detail later.

Figure 1.12: A series of phantoms in different lead concentrations.

1.10   Laboratory Mice

By definition, a laboratory mouse is bred and used for scientific research in different disciplines, such as medicine, genetics and psychology. This mouse species is named *Mus musculus*. It is the most commonly used mammalian research model and offers several advantages. It has a relatively high homology with humans, high reproduction rate and

also ease of handling. CD-1 and C57BL/6J mice were employed in this study, and reasons will be explained thoroughly in the following sub-sections.

1.10.1 CD-1 Mice

CD-1 mice were first used in this study to estimate the Minimum Detection Limits (MDLs) of the XRF system when applied to a mouse model.

Figure 1.13 shows the growth rate of CD-1 Mice for the different sexes. On average, a male increases its weight much faster than a female. As there is strong evidence for the connection between total weight and total number of bone counts in an XRF spectrum, because more mass means a larger skeleton, a greater growth rate should be considered for obtaining a reasonable total number of counts in XRF analysis. A male mouse is much more desirable and thus chosen in this experiment.
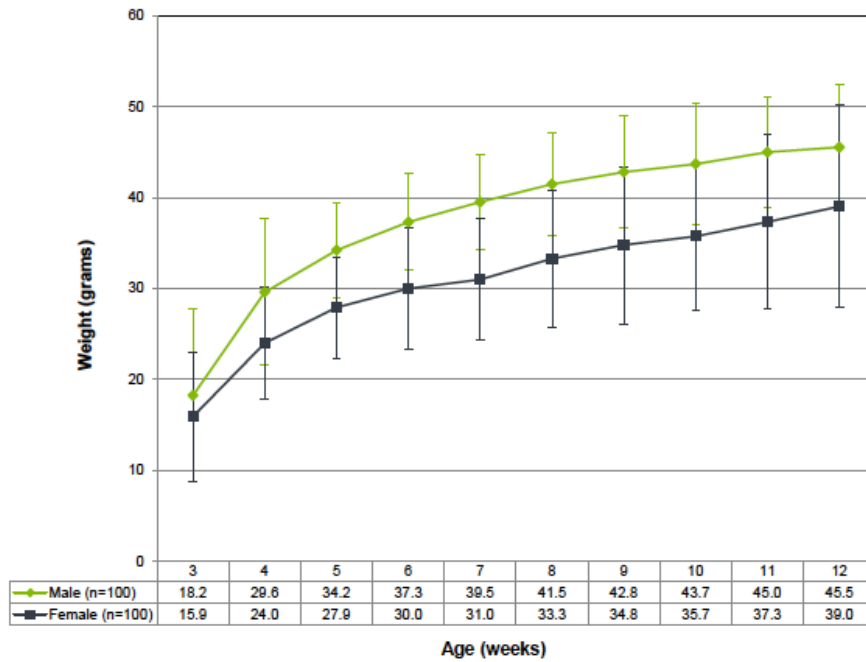
Figure 1.13: Growth rate of CD-1 mice from Envigo, available at: www.envigo.com/products-services/research-models-services/models/research-models/mice/outbred/icr-(cd-1)-outbred-mice/.

1.10.2 C57BL/6J Mice

As this study involved collaboration with Dr. Nicholas Bock's team, a smaller mouse was much preferred to fit in the system for Magnetic Resonance Imaging (MRI). After a discussion, C57BL/6J mice were chosen to replace the previous animal model of CD-1 mice. Figure 1.14 shows the growth rate of C57BL/6J Mice for the different sexes. Similar to CD-1 mice, a male increases its weight much faster than a female. The mass of this mouse model is approximately half of the previous animal model.
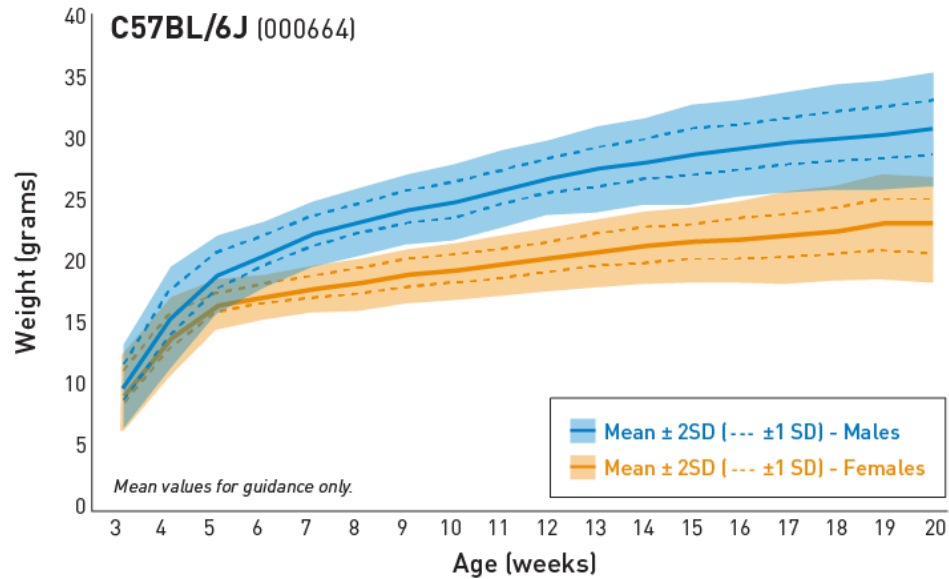
Figure 1.14: Growth rate of C57BL/6J mice from the Jackson Laboratory, available at: www.jax.org/jax-mice-and-services/strain-data-sheet-pages/body-weight-chart-000664.

1.11   Rationale for This Whole Study

The main purpose of this thesis is to study the relationship between de-myelination in brain in vivo using MRI and the cumulative Pb skeletal exposure using XRF. By developing mouse-mimicking phantoms, the feasibility of an in vivo x-ray fluorescence (XRF) system for the Pb measurement in the skeleton of whole mice will be evaluated. This will enhance a future possibility in the measurement of real mouse for Pb skeletal exposure.

CHAPTER 2

MDLs for Pre-existing Bone Pb Phantoms and Pb Free Mice

2.1 Introduction

In the previous chapter, a literature review was conducted. Several topics were included and addressed, namely health impacts of lead, measurement of lead, pre-existing bone Pb phantoms and selection of mouse model. In this chapter, XRF measurements will be taken on pre-existing bone Pb phantoms and 2 strains of Pb free mice. Calibration lines will be obtained from pre-existing bone Pb phantoms, and will be used to estimate the minimum detection limits (MDL) in mice.

2.2 Spectra Collection

2.2.1 Pre-existing Bone Pb Phantoms

Counts were first collected for each of 9 bare bone phantoms. A counting time of 1-hour for each phantom was used. To maximize the collection of counts, each pre-existing bone phantom was placed at 5 mm from the copper face of the tungsten collimator. A total number of three Pb peaks were present on the collected spectra, including Kα2 at 72.804 keV, Kα1 at 74.969 keV, and Kβ1,3 between 84.450-84.936 keV. Samples of collected 1-hour spectra are shown in Figure 2.1 and Figure 2.2.
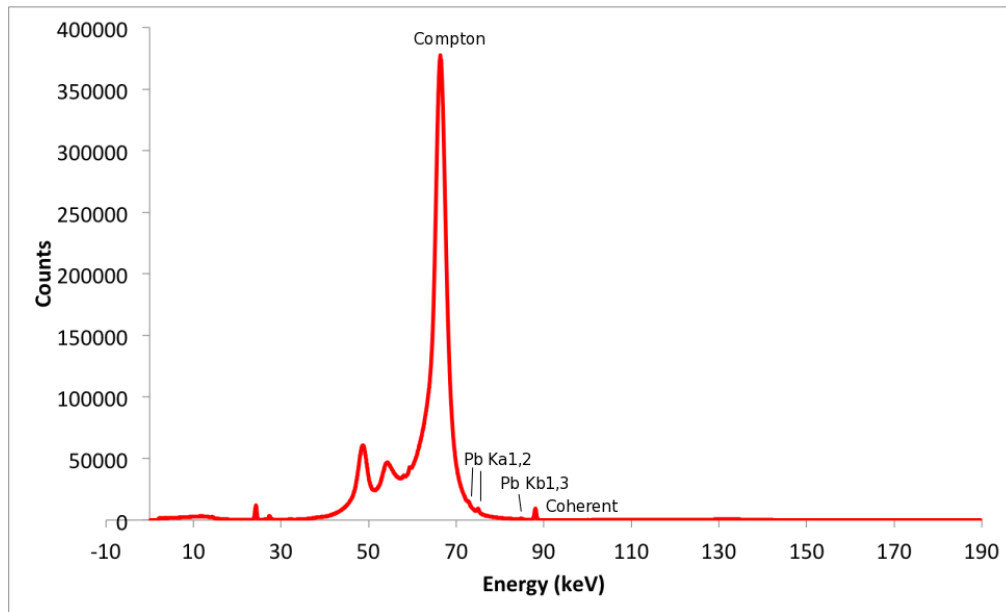
Figure 2.1: A full spectrum for 1-hour counting time of 100 ppm bare bone phantom.
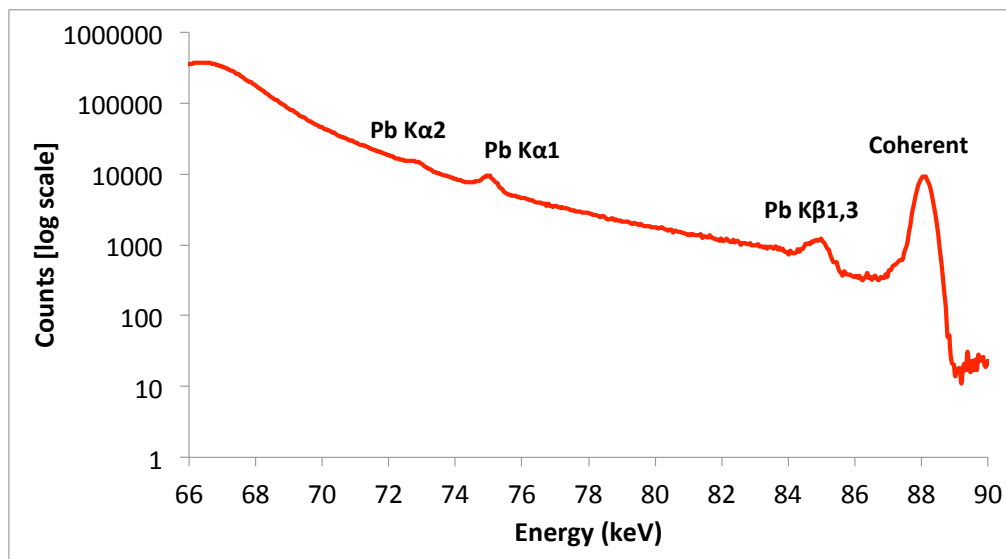
Figure 2.2: Sample spectrum for 1-hour counting time of 100 ppm bare bone phantom in an energy range of 66 - 90 keV. Lead Kα2, Kα1 and Kβ1,3 peaks are located at 72.8 keV, 75.0 keV and between 84.450-84.936 keV respectively.

2.2.2 CD-1 Mice

Three CD-1 mice were used in this experiment. Each mouse was measured in 2 positions, skull and hind, respectively. A counting time of 3 hours for each position was used and a total number of 6 measurements were taken. The source-to-mice distance was kept at 5 mm for consistency. Samples of collected 3-hour spectra are shown in Figure 2.3 and Figure 2.4 respectively.
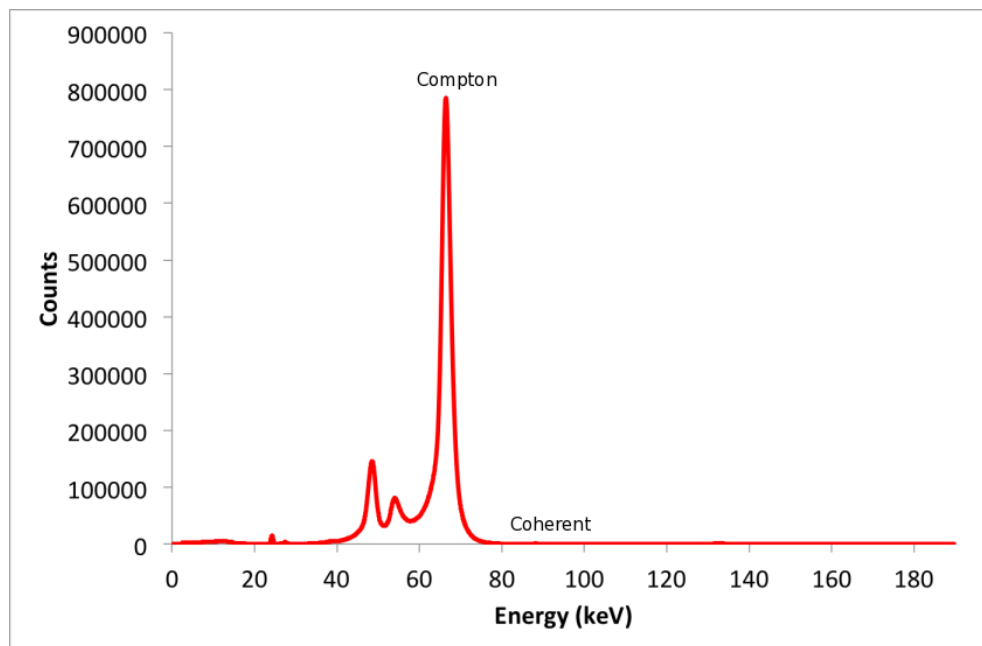
Figure 2.3: A full spectrum for 3-hour counting time of Pb free CD-1 mice.
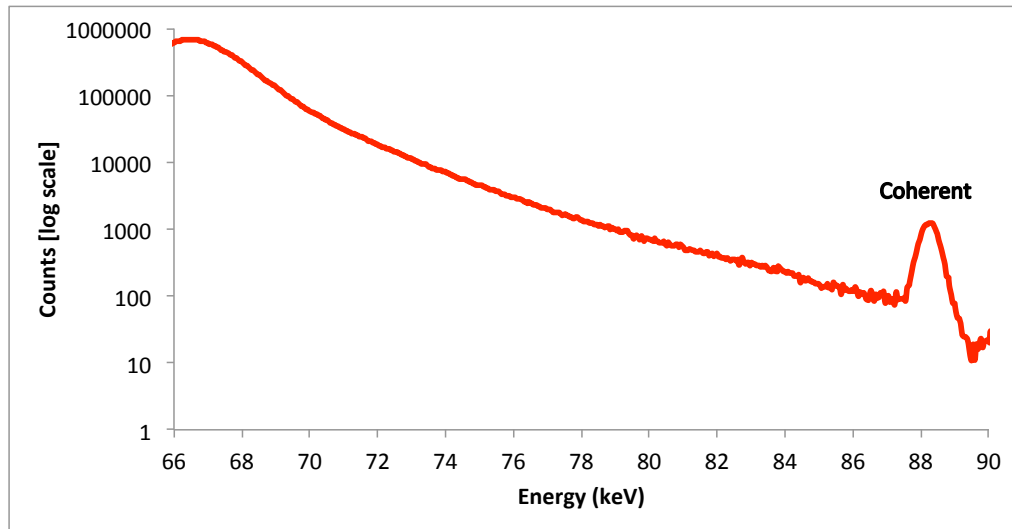
Figure 2.4: Sample spectrum for 3-hour counting time of Pb free CD-1 mouse in an energy range of 66 - 90 keV. Lead Kα2, Kα1 and Kβ1,3 peaks are not present in the spectrum.

2.2.3 C57BL/6J Mice

Four C57BL/6J mice were also used in this experiment. Similar to CD-1 mice measurement, each C57BL/6J mouse was measured in 2 positions, skull and hind, respectively. A counting time of 3 hours for each position was used and a total number of 8 measurements were taken. The source-to-mice distance remained at 5mm for consistency. A sample of a collected 3-hour spectrum is shown in Figure 2.5 and Figure 2.6.
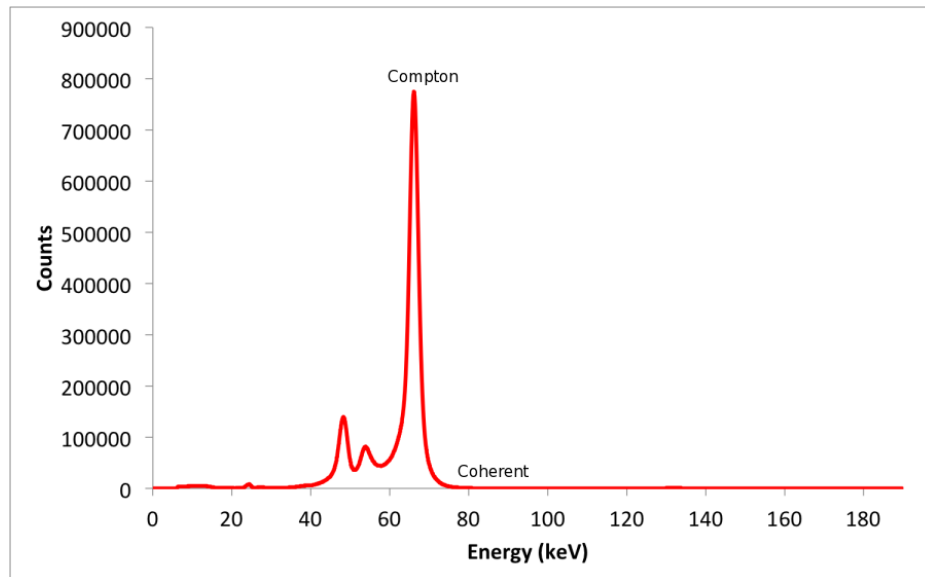
Figure 2.5: A full spectrum for 3-hour counting time of Pb free C57BL/6J mice.
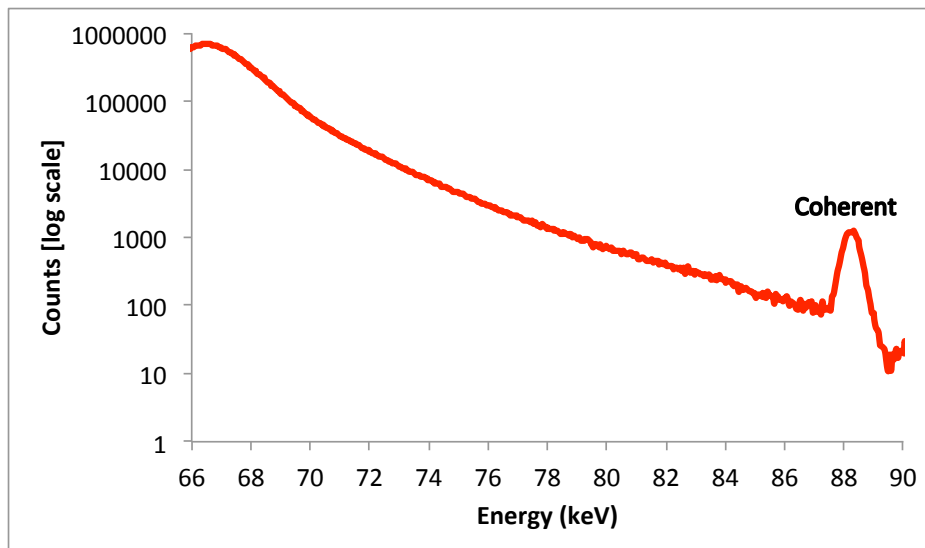
Figure 2.6: Sample spectrum for 3-hour counting time of Pb free C57BL/6J mouse in an energy range of 66 - 90 keV. Lead Kα2, Kα1 and Kβ1,3 peaks are not present in the spectrum.

2.3 Spectra Fitting

The XRF spectrum is further analyzed in order to obtain the lead concentration in bone. It has been found that the ratio of lead K x-rays to coherent peaks provided an accurate estimate of lead concentration (Somervaille et al., 1985). Hence, the concentration of lead with a unit of $\mu g\ Pb/g$ bone mineral is calculated.

As the K X-rays and coherent peaks are vital for obtaining lead concentration, it is extremely important for us to have an accurate spectrum in both phantoms and samples.

There are different energies of lead K X-rays. The main ones are $K\alpha_2$ (72.804 keV), $K\alpha_1$ (74.969 keV), $K\beta_3$ (84.450 keV), $K\beta_1$ (84.936 keV) and $K\beta_2$ (87.367 keV). As different factors such as background and edges contribute to the energy spectrum, the number of counts in K X-rays and coherent peaks cannot be obtained directly. Different peak fitting equations are applied separately to ensure accurate counts. In the following subsections, fitting routines developed by Huiling Nie for the coherent peak, $K\alpha$ peak(s) and $K\beta$ peak are explained (Nie, 2001).

2.3.1 Coherent Peak Fitting

The mono-energetic peak distribution is described by a normal function as follows,

$$f(x) = amplitude \times e^{-\left(\frac{x-channel}{\sqrt{2}\sigma}\right)^2} --- (2.1)$$

where x is the channel number and σ is the standard deviation.

88.035 keV is the coherent peak energy and it's peak center is typically 1900 in terms of channel number for the gain used in these experiments, an energy interval

starting from 86.5 keV to 89.5 keV is used in fitting. Different factors that contribute to this interval in coherent peak fitting are listed in the following,

1. Lead $K\beta_2$ X-rays contribution

The energies of $K\beta_2$ X-rays are 87.233 keV and 87.367 keV, they can be expressed by a normal distribution.

2. Background contribution

It can be expressed as exponential function as it is distributed exponentially.

3. O K edge, Ca L edge, C K edge, S L edge and P L edge contribution

These edges are the upper limit of the Doppler broadened distribution of Compton scattering. They are located in 87.504 keV, 87.65 keV, 87.752 keV, 87.8 keV and 87.9 keV.

4. Step contribution

There is a step located in $K\beta_2$ and coherent peak due to the charge collection incompleteness. A complementary error function erfc(z) is used to describe this contribution. Complementary error function is derived from error function erf(z), and z is the Gaussian parameter and equation is shown in the following,

$$z = \frac{(x - \mu)}{\sqrt{2}\sigma} - - - (2.2)$$

Considering the above contributions from different parameters, coherent peak is expressed by the following equation and fitted in MATLAB and R respectively. A Nonlinear Least Squares fitting method is used (Bevington et al., 1993).

$$f(x) = p(2) \times \left(\exp\left(-\left(\frac{x - p(1)}{p(3)} \right)^2 \right) + p(7) \times erfc\left(\frac{x - p(1)}{p(3)} \right) \right)$$

$$+ p(4) \times \left(\exp\left(-\left(\frac{x - \left(p(1) - \frac{668}{G} \right)}{p(3)} \right)^2 \right) + p(7) \times erfc\left(\frac{x - \left(p(1) - \frac{668}{G} \right)}{p(3)} \right) \right)$$

$$+ 0.509 \times \left(\exp\left(-\left(\frac{x - \left(p(1) - \frac{802}{G} \right)}{p(3)} \right)^2 \right) + p(7) \times erfc\left(\frac{x - \left(p(1) - \frac{802}{G} \right)}{p(3)} \right) \right)$$

$$+ p(5) \times \exp(p(6) \times x)$$

(2.3)

where

p(1) is the coherent peak position;

p(2) is the coherent amplitude;

p(3) is the coherent peak width, expressed as $\sqrt{2}\sigma$ and calculated by $\frac{\sqrt{2}FWHM}{2.355}$;

p(4) is the $K\beta_2$ amplitude;

p(5) is the exponential background amplitude;

p(6) is the exponential background exponent coefficient;

p(7) is the fraction of peak height and named as step height;

G is the gain and expressed in a unit of eV/channel. It can be obtained from the slope of

calibration line. The calibration line is calculated from the energy spectrum.

Two $K\beta_2$ positions are fixed with respect to the coherent peak position and described as

$\left(p(1) - \frac{608}{G} \right)$ and $(p(1) - \frac{802}{G})$ in the above fitting equations. 668 eV and 802 eV are the

energy difference between two $K\beta_2$ positions and coherent peak. The number of channels

between two $K\beta_2$ positions and coherent peak are described as $\left(\frac{608}{G}\right)$ and $\left(\frac{802}{G}\right)$ respectively.

2.3.2 Alpha Peak(s) Fitting

72.804 keV and 74.969 keV are the peak energies of $K\alpha_2$ and $K\alpha_1$. Because it is hard to fit two energy peaks that are separated far apart, $K\alpha_1$ peak becomes the fitting target with a consideration of $K\alpha_2$ and a background factor. The background factor is expressed as two exponential functions, as the background under $K\alpha_2$ and $K\alpha_1$ peaks is a factor of Compton scattering and decreases rapidly.

Hence, the $K\alpha_1$ peak fitting function is described as follows,

$$f(x) = p(2) \times \left(\exp\left(-\left(\frac{x - p(1)}{W} \right)^2 \right) + H \times erfc\left(\frac{x - p(1)}{W} \right) \right)$$

$$+ (0.593 \times p(2)) \times \left(\exp\left(-\left(\frac{x - \left(p(1) - \frac{2165}{G} \right)}{W} \right)^2 \right) \right.$$

$$\left. + H \times erfc\left(\frac{x - \left(p(1) - \frac{2165}{G} \right)}{W} \right) \right)$$

$$+ p(3) \times exp(p(4) \times x) + p(5) \times \exp(p(6) \times x)$$

$$(2.4)$$

where

p(1) is the $K\alpha_1$ peak position;

p(2) is the $K\alpha_1$ amplitude;

p(3) is the exponential background 1 amplitude;

p(4) is the exponential background 1 exponent coefficient;

p(5) is the exponential background 2 amplitude;

p(6) is the exponential background 2 exponent coefficient;

W is the peak width, a fixed parameter obtained from coherent fitting;

H is the step height, a fixed parameter obtained from coherent fitting;

The energy difference between $K\alpha_2$ and $K\alpha_1$ peaks is 2165 eV, and hence the number of channels between $K\alpha_2$ and $K\alpha_1$ peaks is described as $(\frac{2165}{G})$ in the fitting equation.

2.3.3 Beta Peak Fitting

84.450 keV, 84.936 keV and 87.300 keV are the energies of $K\beta_3$, $K\beta_1$ and $K\beta_2$ respectively. As the yield of $K\beta_2$ is relatively small and the various edges noted above under 2.3.1 point 3 are very close in energy, only the $K\beta_3$ and $K\beta_1$ energies are taken into fitting consideration. Because it is hard to fit two energy peaks that are close, $K\beta_1$ peak becomes the fitting target with a consideration of $K\beta_3$ and several factors. Various factors contribute to this energy interval, and they are listed as follows,

1. Ca K edge contribution

The energy of Ca K edge is 83.997 keV.

2. P K edge contribution, which is only used for fitting in human or other actual bone measurements.

The energy of P K edge is 85.889 keV.

3. S K edge contribution, which is only used for fitting in Plaster of Paris phantom

   measurements.

The energy of S K edge is 85.288 keV.

4. Background contribution

It can be expressed as exponential function as it is distributed exponentially.

5. Step contribution

There is a step located in every peak due to the incompleteness of charge collection.

Hence, the $K\beta_1$ fitting function in phantoms measurement is described as follows,

$$f(x) = p(1) \times \left(\exp\left(-\left(\frac{x - \left(A - \frac{3099}{G}\right)}{W} \right)^2 \right) + H \times erfc\left(\frac{x - \left(A - \frac{3099}{G}\right)}{W} \right) \right)$$

$$+ (0.523 \times P(1)) \times \left(\exp\left(-\left(\frac{x - \left(A - \frac{3585}{G}\right)}{W} \right)^2 \right) + H \times erfc\left(\frac{x - \left(A - \frac{3585}{G}\right)}{W} \right) \right)$$

$$+ p(2) \times \exp(p(3) \times x)$$

$$+ 0.03 \times B \times \left(\exp\left(p(4) \times x - \left(A - \frac{4038}{G}\right) \right) \times erfc\left(\frac{x - \left(A - \frac{4038}{G}\right)}{W} \right) \right.$$

$$+ 0.44 \times \exp\left(p(4) \times x - \left(A - \frac{2747}{G}\right) \right) \times erfc\left(\frac{x - \left(A - \frac{2747}{G}\right)}{W} \right) \bigg)$$

$$(2.5)$$

where

p(1) is the $K\beta_1$ amplitude;

p(2) is the exponential background amplitude;

p(3) is the exponential background exponent coefficient;

p(4) is the calcium and phosphorus edges exponential;

A is the coherent peak position, a fixed parameter obtained from coherent fitting;

B is the coherent peak amplitude, a fixed parameter obtained from coherent fitting;

H is the step height, which is a fixed parameter obtained from coherent fitting;

W is the peak width, which is a fixed parameter obtained from coherent fitting;

2747 eV is the energy difference between S edge and coherent peak. The number of channels between S edge and coherent peak is described as $(\frac{2747}{G})$. And 4038 eV is the energy difference between Ca edge and coherent peak. The number of channels between Ca edge and coherent peak is described as $(\frac{4038}{G})$.

Besides, the $K\beta_1$ fitting function in human or other actual bone measurement is described as follows,

$$f(x) = p(1) \times \left(\left(\exp\left(-\left(\frac{x - \left(A - \frac{3099}{G}\right)}{W} \right)^2 \right) \right) + H \times erfc\left(\frac{x - \left(A - \frac{3099}{G}\right)}{W} \right) \right)$$

$$+ (0.523 \times P(1)) \times \left(\exp\left(-\left(\frac{x - \left(A - \frac{3585}{G}\right)}{W} \right)^2 \right) + H \times erfc\left(\frac{x - \left(A - \frac{3585}{G}\right)}{W} \right) \right)$$

$$+ p(2) \times \exp(p(3) \times x)$$

$$+ 0.04 \times B \times \left(\exp\left(p(4) \times x - \left(A - \frac{4038}{G}\right) \right) \right) \times erfc\left(\frac{x - \left(A - \frac{4038}{G}\right)}{W} \right))$$

$$+0.21 \times \exp\left(p(4) \times x - \left(A - \frac{2146}{G}\right)\right) \times erfc(\frac{x - \left(A - \frac{2146}{G}\right)}{W}))$$

$$(2.6)$$

The above function shared the same parameters in the $K\beta_1$ fitting function in Plaster of Paris phantom measurements, except that 2146 eV is the energy difference between P edge and coherent peak and the ratios between the Ca and P edges and to coherent are different. The number of channels between P edge and coherent peak is described as $(\frac{2146}{G})$.

Overall, the counts among $K\beta_1$ peak area in phantoms or human measurement could be described as follows,

$Background\ contribution + K\beta_1\ contribution + K\beta_3 contribution$

$+Ca\ edge\ contribution + S\ edge\ (phantoms)\ or\ P\ edge\ (humans)\ contribution$

2.3.4 Goodness of Fit X^2 (Reduced Chi-squared Test)

The goodness of fit is used when we want to know how well a function fits a set of observations in a statistical model. In order to evaluate the discrepancy between experimental values and expected value, we have to measure the goodness of fit. A test of goodness of fit is used and it is called reduced chi-squared test.

Reduced chi-squared test is defined as chi-squared (X^2) per degree of freedom (v).

$$X_v^2 = \frac{X^2}{v} - - - (2.7A)$$

Chi-squared is defined the sum of differences between experimental outcome and expected outcome frequencies, and each squared and divided by the expectation.

$$X^2 = \sum_{i=1}^{n} \frac{(E_i - e_i)^2}{e_i} - - - (2.7B)$$

where

E_i = Observed count in channel number i;

e_i = Expected/calculated count in channel number i from fitting;

v = Degree of freedom, $v = n - m$, which is equal to the number of observations n minus the number of fitted parameters m.

Ideally, the expected value of the reduced chi-squared X_v^2 is 1, which indicates the extent of the match between observations and expectation. A value of X_v^2 much larger than 1 indicates a poor model fit, as it did not capture the data entirely. A value of X_v^2 smaller than 1 is also unacceptable and implies some misunderstanding of the experiment (Bevington et al., 1993).

2.4 Fitting Results using MATLAB

The Pb peaks were extracted from each spectrum, and were first analyzed using a MATLAB script. Spectra fitting equations have already explained in Section 2.2. In general, three peak amplitudes were obtained along with their uncertainties. Problems were encountered and will be explained in the following subsection.

2.4.1 Pre-existing Bone Pb Phantoms

As shown in Table 2.1, peak ratios were obtained using MATLAB from each spectrum in detector 1. Even though chi-squared values were in a range of 0.82 to 2.11, uncertainties obtained were not consistent from the same peak. Take coherent peak as an example, the uncertainties obtained (as shown in red color in Table 2.1) from fitting should be consistent in different Pb concentrations. This inconsistency in uncertainties was not acceptable for further analysis. Table 2.2 is an example for a summary of Pb K x-rays/coherent peak ratios. Due to the inconsistency in peak uncertainties, the relative uncertainties calculated (as shown in blue color in Table 2.2) are relatively larger than expected values (as shown in Table 2.4). Hence, we have to use another statistical computing software to replace MATLAB. And R was chosen as alternative software for calculating precise minimum detection limits (MDLs).

Detector 1									
ppm	Coherent peak	±	X^2	$K\alpha_1$ peak	±	X^2	$K\beta_1$ peak	±	X^2
100	8998.60	19.35	0.90	2583.53	171.04	1.16	564.66	19.79	1.52
70	8962.27	15.79	1.28	1841.90	127.92	0.82	414.68	20.82	1.39
30	8348.23	754.89	1.01	717.76	50.81	1.24	188.15	18.50	1.32
21.08	11295.79	2485.65	1.11	744.55	52.15	1.05	234.36	23.02	1.39
16.8	9516.58	1352.21	0.95	577.61	40.12	1.26	160.51	19.12	1.21
12.6	9592.88	5449.00	0.97	312.01	22.11	1.36	96.70	16.68	0.97
8.4	9878.31	4329.93	1.04	213.07	14.66	0.88	72.56	18.39	1.07
4.2	9966.29	5326.97	2.06	57.84	3.89	1.19	46.53	21.18	1.26
0	6876.76	216887.43	1.23	10.00	0.67	0.99	62.72	20.85	2.11

Table 2.1. Summary of MATLAB script fitting results (in amplitude) in pre-existing bone Pb phantoms of detector 1.

Detector 1				
ppm	$K\alpha_1$ peak / Coherent peak	% error	$K\beta_1$ peak / Coherent peak	% error
100	0.287	6.835	0.063	3.720

70	0.206	7.121	0.046	5.197
30	0.086	16.121	0.023	18.875
21.08	0.066	29.009	0.021	31.828
16.8	0.061	21.155	0.017	26.121
12.6	0.033	63.889	0.010	74.052
8.4	0.022	50.713	0.007	69.177
4.2	0.006	60.175	0.005	98.969
0	0.001	3160.619	0.009	3187.162

Table 2.2. Summary of Pb K X-rays/Coherent peak ratios in pre-existing bone Pb phantoms of detector 1.

Because R replaces MATLAB for all the spectrum fittings in initial stages, Table 2.1 and Table 2.2 are the examples of fitting summaries for only 1 detector. In the next section (Section 2.5), fitting results for all 4 detectors will be shown.

2.5 Fitting Results using R

Similar to Section 2.4, Pb coherent, Kα and Kβ peaks were extracted from each spectrum and analyzed using R script.

2.5.1 Pre-existing Bone Pb Phantoms

The fit for the Pb peaks agreed well with the spectra, and chi-squared values are in a range of 0.80 to 1.38 (detector 1); 0.67 to 1.48 (detector 2); 0.72 to 1.47 (detector 3); 0.82 to 1.36 (detector 4).

Detector 1									
ppm	Coherent peak	±	X^2	$K\alpha_1$ peak	±	X^2	$K\beta_1$ peak	±	X^2
100	9000.35	22.88	0.92	2563.32	48.86	1.13	589.91	18.32	1.29
70	8962.49	18.53	1.19	1806.06	51.32	1.23	401.83	17.18	1.22
30	8653.21	22.85	1.19	657.01	50.66	1.27	220.26	16.87	1.33
21.08	11828.51	26.65	1.26	808.53	50.26	1.16	227.24	16.10	1.34
16.8	9725.28	14.11	0.82	494.07	40.44	1.06	183.46	14.63	1.22
12.6	9916.22	20.25	0.80	402.68	37.92	0.98	129.97	12.05	1.28
8.4	9901.54	18.40	1.20	329.46	38.21	1.12	105.44	14.10	1.24

| 4.2 | 10154.81 | 22.02 | 1.11 | 147.19 | 44.92 | 0.97 | 87.68 | 15.05 | 1.22 |
| 0 | 7168.79 | 15.40 | 0.94 | 47.96 | 31.91 | 0.96 | 38.84 | 11.93 | 1.38 |

Table 2.3. Summary of R script fitting results (in amplitude) in pre-existing bone Pb phantoms of detector 1.

Detector 1				
ppm	Kα$_1$ peak / Coherent peak	% error	Kβ$_1$ peak / Coherent peak	% error
100	0.285	1.923	0.066	3.116
70	0.202	2.849	0.045	4.280
30	0.076	7.715	0.025	7.664
21.08	0.068	6.220	0.019	7.089
16.8	0.051	8.186	0.019	7.976
12.6	0.041	9.419	0.013	9.274
8.4	0.033	11.599	0.011	13.374
4.2	0.014	30.519	0.009	17.166
0	0.007	66.535	0.005	30.717

Table 2.4. Summary of Pb K X-rays/Coherent peak ratios in pre-existing bone Pb phantoms of detector 1.

Detector 2									
ppm	Coherent peak	±	X^2	Kα$_1$ peak	±	X^2	Kβ$_1$ peak	±	X^2
100	8156.73	21.30	1.49	2322.43	39.68	1.07	551.23	19.16	1.30
70	8169.16	20.74	1.25	1716.83	36.96	0.85	404.95	17.97	1.24
30	7941.77	21.48	1.23	682.51	32.44	0.81	222.09	16.58	1.24
21.08	10847.18	21.19	0.99	747.56	35.03	0.81	234.60	16.12	1.48
16.8	10919.56	24.24	1.22	614.00	39.79	0.95	216.26	18.00	1.27
12.6	11117.73	22.21	1.11	584.69	42.95	0.97	187.74	18.60	0.99
8.4	11008.60	19.19	0.87	339.93	40.11	1.10	144.92	16.12	1.20
4.2	11275.89	19.92	0.88	164.52	38.68	0.99	122.17	13.65	1.12
0	7894.91	17.01	1.29	31.19	36.48	1.18	21.52	12.74	1.25

Table 2.5. Summary of R script fitting results (in amplitude) in pre-existing bone Pb phantoms of detector 2.

Detector 2				
ppm	Kα$_1$ peak / Coherent peak	% error	Kβ$_1$ peak / Coherent peak	% error
100	0.285	1.728	0.068	3.486
70	0.210	2.168	0.051	4.445
30	0.086	4.761	0.028	7.470
21.08	0.069	4.690	0.022	6.874
16.8	0.056	6.484	0.020	8.326
12.6	0.053	7.348	0.017	9.909
8.4	0.031	11.801	0.013	11.125

4.2	0.015	23.511	0.011	11.174
0	0.004	116.961	0.003	59.201

Table 2.6. Summary of Pb K X-rays/Coherent peak ratios in pre-existing bone Pb phantoms of detector 2.

Detector 3									
ppm	Coherent peak	±	X^2	$K\alpha_1$ peak	±	X^2	$K\beta_1$ peak	±	X^2
100	5472.05	16.31	1.18	1485.73	30.64	1.48	380.85	10.86	1.19
70	5297.60	18.60	1.33	1068.73	31.23	1.08	270.76	21.89	1.28
30	5148.63	17.15	1.05	406.04	26.79	0.86	148.74	13.55	1.18
21.08	7117.84	18.63	1.26	480.67	29.56	1.03	171.51	17.84	1.39
16.8	11149.61	24.02	1.36	587.47	36.53	1.02	222.48	19.55	1.27
12.6	11261.35	22.95	1.28	520.49	37.69	0.96	196.25	18.75	1.16
8.4	11189.81	20.50	0.72	356.75	36.30	0.99	137.89	16.52	1.47
4.2	11403.46	18.47	0.89	119.20	33.90	0.82	133.19	17.45	1.22
0	7867.73	15.00	0.97	54.18	32.10	0.81	40.56	14.35	1.29

Table 2.7. Summary of R script fitting results (in amplitude) in pre-existing bone Pb phantoms of detector 3.

Detector 3				
ppm	$K\alpha_1$ peak / Coherent peak	% error	$K\beta_1$ peak / Coherent peak	% error
100	0.272	2.084	0.070	2.867
70	0.202	2.943	0.051	8.092
30	0.079	6.606	0.029	9.116
21.08	0.068	6.155	0.024	10.405
16.8	0.053	6.222	0.020	8.790
12.6	0.046	7.244	0.017	9.556
8.4	0.032	10.177	0.012	11.982
4.2	0.010	28.440	0.012	13.103
0	0.007	59.247	0.005	35.380

Table 2.8. Summary of Pb K X-rays/Coherent peak ratios in pre-existing bone Pb phantoms of detector 3.

Detector 4									
ppm	Coherent peak	±	X^2	$K\alpha_1$ peak	±	X^2	$K\beta_1$ peak	±	X^2
100	6473.98	17.35	0.95	1891.89	32.04	0.92	448.94	13.79	1.18
70	6418.20	21.53	1.13	1250.58	30.79	0.82	337.40	15.82	1.35
30	6282.69	23.92	1.22	536.34	39.22	1.09	162.99	10.77	0.89
21.08	8565.11	22.15	1.24	634.43	37.01	1.18	172.73	13.50	1.36
16.8	9625.05	20.30	1.22	547.38	37.89	1.07	166.67	15.60	1.25
12.6	9597.40	20.85	0.97	377.80	34.09	0.87	138.03	15.40	1.32
8.4	9410.58	12.58	0.89	325.92	36.29	1.11	138.47	15.63	1.28

| 4.2 | 9308.41 | 16.42 | 1.31 | 105.37 | 35.45 | 0.97 | 99.09 | 11.32 | 0.87 |
| 0 | 7204.23 | 25.78 | 1.16 | 50.78 | 27.21 | 0.77 | 21.70 | 16.95 | 1.28 |

Table 2.9. Summary of R script fitting results (in amplitude) in pre-existing bone Pb phantoms of detector 4.

Detector 4				
ppm	Kα_1 peak / Coherent peak	% error	Kβ_1 peak / Coherent peak	% error
100	0.290	1.715	0.070	3.083
70	0.195	2.485	0.053	4.701
30	0.085	7.322	0.026	6.619
21.08	0.074	5.839	0.020	7.820
16.8	0.057	6.925	0.017	9.362
12.6	0.039	9.026	0.014	11.159
8.4	0.035	11.135	0.015	11.288
4.2	0.008	33.644	0.011	11.425
0	0.007	53.585	0.003	78.111

Table 2.10. Summary of Pb K X-rays/Coherent peak ratios in pre-existing bone Pb phantoms of detector 4.

2.6 Comparison between MATLAB and R Fitting Results

In the previous sections, MATLAB and R scripts were run to fit pre-existing bone Pb phantom spectrums. Three amplitude ratios were obtained with respect to their uncertainties.

As shown in section 2.4, MATLAB scripts were first used to fit the pre-existing bone Pb phantoms. Table 2.1 shows a summary of MATLAB fitting results of detector 1. From Table 2.1, MATLAB analyzes peak amplitudes easily and matches to our expectation (spectrums obtained from measurements). However, the accuracy of MATLAB analysis in peak amplitude uncertainties is questionable. Based on the previous experience, we hypothesized that consistent uncertainties should be obtained by using same fitting equation. Hence, R is chosen to verify this hypothesis.

As shown in section 2.5, R scripts were used to fit the same set of pre-existing bone Pb phantoms. Compared to Table 2.1, Table 2.3 has similar amplitudes among three peaks (coherent, Kα and Kβ peaks). However, consistent uncertainties are observable in Table 2.3. This consistency in uncertainties shows that R is more suitable than MATLAB in statistical analysis. As uncertainty could significantly affect the MDLs calculation in the later part of study, we used R to replace MATLAB in all fittings.

2.7 Calibration Lines for Pre-existing Bone Pb Phantoms

In order to estimate the minimum detection limits (MDLs) of Pb free mice, X-ray peak calibration lines were obtained from same set of pre-existing bone Pb phantoms that measured thrice. The values for each calibration line are summarized in Table 2.11. The calibration lines for the pre-existing bone Pb phantoms are displayed in Figure 2.7 (a-d).

Detector	K X-rays	Slope	Standard Error of the Slope	Intercept	Standard Error of the Intercept
1	α_1	2.75E-03	5.20E-05	6.06E-03	2.24E-03
	β_1	5.90E-04	1.33E-05	5.27E-03	5.75E-04
2	α_1	2.69E-03	5.92E-05	7.47E-03	2.56E-03
	β_1	5.84E-04	1.94E-05	5.07E-03	8.38E-04
3	α_1	2.76E-03	6.56E-05	6.32E-03	2.83E-03
	β_1	6.78E-04	4.27E-05	5.28E-03	1.84E-03
4	α_1	2.80E-03	6.97E-05	4.28E-03	3.01E-03
	β_1	6.37E-04	3.16E-05	5.49E-03	1.37E-03

Table 2.11. A summary of calibration lines of cloverleaf XRF system.
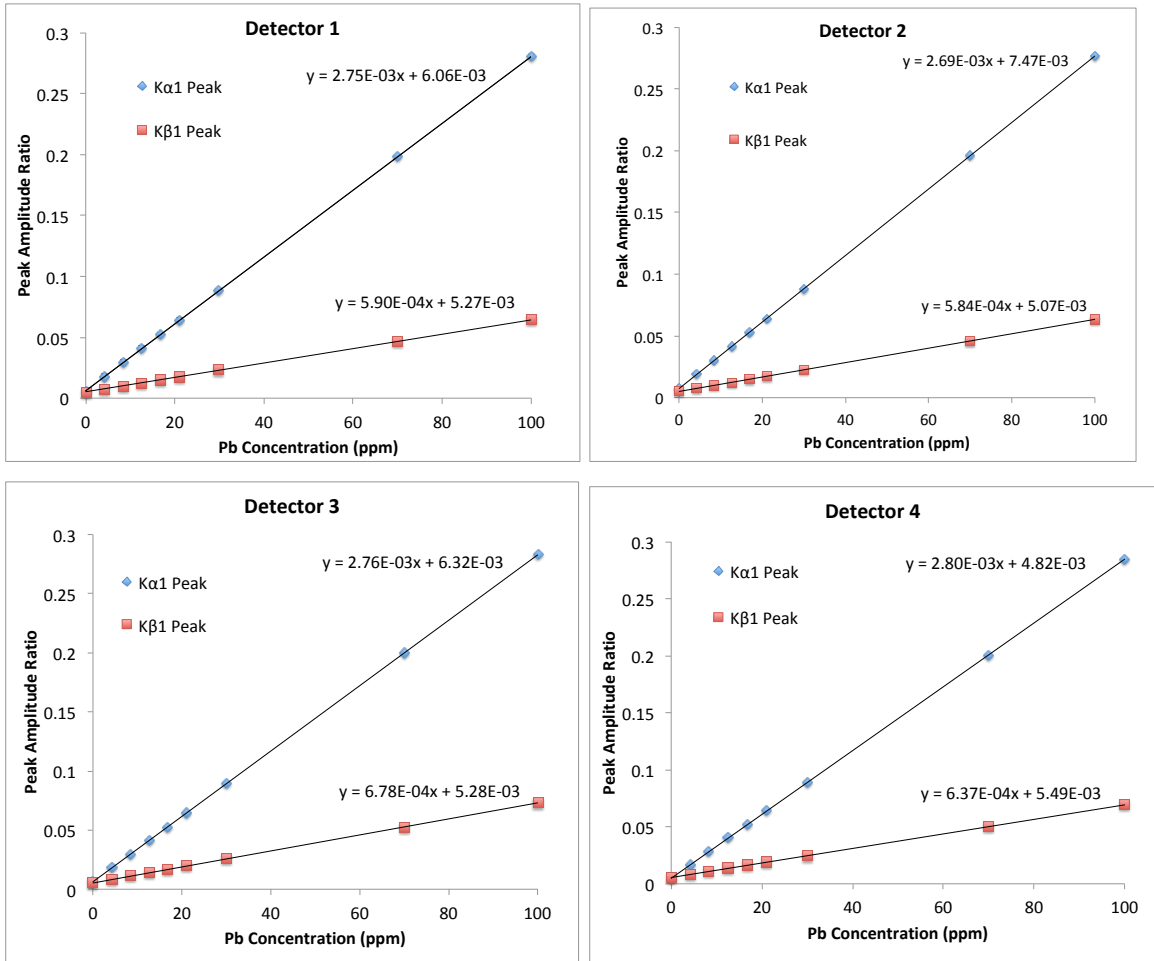
Figure 2.7. Calibration lines for the pre-existing bone Pb phantoms: (a) detector 1, (b) detector 2, (c) detector 3 and (d) detector 4.

2.8 Minimum Detection Limits (MDLs) Calculation

The minimum detection limit (MDL) is defined as two times the uncertainty of Pb concentration (2σ) and indicated as the lowest Pb concentration that our XRF system can detect. The relationship between Pb peak amplitude ratio and the respective concentration of the phantoms is plotted and fit by linear regression. The fit line (calibration line) is expressed as the following equation:

$$y_{exp} = mx + b \; - - - \; (2.9)$$

where y_{exp} is the Pb peak/coherent peak amplitude ratio, m is the slope of the calibration line, x is the Pb concentration and b is the calibration line intercept.

The standard deviation σ_x was calculated by the sum of variances from different factors, including the calibration line's slope, intercept, covariance between slope and intercept and the variance of the background under Pb Kα and Kβ peaks. Using the approach described by Shehab, (Shehab et al 2015), the σ_x was determined with the following equation:

$$\sigma_{x_{exp}}^2 = \left(\frac{\sigma_{y_{exp}}}{m}\right)^2 + \left(\frac{\sigma_b}{m}\right)^2 + \frac{\sigma_m^2(b - y_{exp})^2}{m^4} + 2\left(\frac{y_{exp} - b}{m^3}\right)\left(-\frac{\sigma_y^2 \sum_{i=1}^{N} x_i}{D}\right) \; - - - \; (2.10)$$

where

$$\sigma_y^2 = \sum_{i=1}^{N} \frac{[y_i - (mx_i + b)]^2}{N - 2} \; ; D = N \sum_{i=1}^{N} x_i^2 - \left(\sum_{i=1}^{N} x_i\right)^2 \; - - - \; (2.11)$$

where N is the number of points on the calibration line, $m \pm \sigma_m$ and $b \pm \sigma_b$ is the slope and intercept. $y_{exp} \pm \sigma_{y,exp}$ is the Pb peak/coherent peak amplitude ratio and error.

The MDL is defined as $2\sigma_x$. As the cloverleaf XRF system consists of four detectors, an inverse variance weighted mean method was used to calculate a combined MDL for both Pb peaks and an overall MDL for the system (Chamberlain et al., 2012).

$$Combined \; MDL = \left(\frac{1}{\frac{1}{MDL_{K\alpha}^2} + \frac{1}{MDL_{K\beta}^2}}\right)^{\frac{1}{2}} \; - - - \; (2.12)$$

$$Overall\ MDL = \left(\frac{1}{\frac{1}{MDL_1^2} + \frac{1}{MDL_2^2} + \frac{1}{MDL_3^2} + \frac{1}{MDL_4^2}} \right)^{\frac{1}{2}} - - - (2.13)$$

2.8.1 Pre-existing Bone Pb Phantoms

As shown in table 2.12, minimum detection limits (MDLs) from K-α and K-β are calculated. Since cloverleaf XRF system has 4 detectors, a combined MDL is also calculated by an inverse variance weighted mean method explained in section 2.8.

3 measurements of pre-existing phantoms	
MDLs	(μg Pb /g bone mineral)
From K-α	1.73
From K-β	3.20
Combined	1.52

Table 2.12. Minimum detection limits from same set pre-existing bone pb phantoms that measured thrice. These values are calculated by an inverse variance weighted mean method mentioned in section 2.8.2.

	1st	2nd	3rd	Average coherent peak area
Detector 1	116349.58	98921.95	130325.44	115198.99
Detector 2	112600.04	94183.61	121246.94	109343.53
Detector 3	94747.57	85560.18	88137.36	89481.70
Detector 4	99525.14	88955.11	101373.35	96617.86

Table 2.13. Coherent peak areas obtained from same set pre-existing bone pb phantoms that measured thrice. An average coherent peak area is calculated for each detector.

$Mean\ Coherent\ Peak\ Area\ from\ pre-existing\ bone\ Pb\ phantoms\ among\ 4\ detectors$

$$= \left(\frac{\overline{A_1} + \overline{A_2} + \overline{A_3} + \overline{A_4}}{4} \right) = 102660.52 - - - (2.14)$$

Fitting methods that mentioned in section 2.3 are not applicable for estimating MDLs directly, as there is no Pb x-rays present in two strains of Pb-free mice. Instead, MDLs of

Pb-free mice could be estimated from coherent peak area and calculated MDLs of pre-existing bone Pb phantoms. As such, coherent peak area is averaged from 4 detectors and will be used in the following subsections.

Since the MDL is proportional to the square root of the mean coherent peak area, each MDL value was calculated to estimate the amount of Pb in mice. Because of the difference in matrix between Plaster of Paris and bone mineral, we have to multiply a Pb estimate derived directly from a Plaster of Paris (bone phantoms) calibration line by a factor of 1.46.

$$\frac{MDL_{bone\ phantom}}{MDL_{mouse}} = \sqrt{\frac{Mean\ Coherent\ Peak\ Area_{mouse}}{Mean\ Coherent\ Peak\ Area_{bone\ phantom}}}$$

MDL_{mouse} (in µg Pb /g Plaster of Paris)

$$= \left(\frac{MDL_{bone\ phantom}}{\sqrt{\frac{Mean\ Coherent\ Peak\ Area_{mouse}}{Mean\ Coherent\ Peak\ Area_{bone\ phantom}}}} \right) - - - (2.15)$$

MDL_{mouse} (in µg Pb /g bone mineral)

$$= \left(\frac{MDL_{bone\ phantom}}{\sqrt{\frac{Mean\ Coherent\ Peak\ Area_{mouse}}{Mean\ Coherent\ Peak\ Area_{bone\ phantom}}}} \right) \times 1.46 - - - (2.16)$$

2.8.2 CD-1 Mice

A total number of three CD-1 mice were used. Two orientations were measured and each in a period of 3 hours. Coherent peak areas with relative uncertainties are summarized in table 2.14, and estimated MDLs are summarized in table 2.15. For a better presentation, table 2.16 shows mean MDLs in two orientations of 4 detectors.

		Detector 1		Detector 2		Detector 3		Detector 4	
		Coherent peak area	% error	Coherent peak area	% error	Coherent peak area	% error	Coherent peak area	% error
Skull to detector	1st	17895.00	0.94	11537.00	1.17	16831.00	0.93	16831.00	0.93
	2nd	6233.00	1.71	6138.00	1.64	7441.00	1.33	13644.00	0.95
	3rd	7617.00	1.56	10299.00	1.23	11956.00	1.13	12525.00	1.08
Hind to detector	1st	13159.00	1.18	9661.00	1.38	10707.00	1.30	11889.00	1.25
	2nd	4740.00	1.88	3897.00	2.09	5687.00	1.64	13760.00	0.92
	3rd	6643.00	1.76	9754.00	1.32	11373.00	1.24	11541.00	1.20

Table 2.14. Coherent peak areas with relative uncertainties obtained from CD-1 mice. The skull and hind of mice faced directly to the system.

MDLs (μg Pb /g bone mineral)		From K-α	From K-β	Combined
Skull to detector	1st	6.44	11.91	5.66
	2nd	8.85	16.37	7.78
	3rd	7.85	14.54	6.92
Hind to detector	1st	7.59	14.05	6.69
	2nd	9.67	17.87	8.50
	3rd	8.16	15.10	7.18

Table 2.15. MDLs estimated for CD-1 mice using equation (2.16).

Mean MDLs (μg Pb /g bone mineral)	From K-α	From K-β	Combined
Skull to detector	7.72	14.28	6.79
Hind to detector	8.47	15.67	7.45

Table 2.16. Mean MDLs for CD-1 mice, which their skulls and hinds faced to the system respectively.

2.8.3 C57BL/6J Mice

A total number of four C57BL/6J mice were used. Two orientations were measured and each in a period of 3 hours. Coherent peak areas with relative uncertainties are

summarized in table 2.17, and estimated MDLs are summarized in table 2.18. For a better

presentation, table 2.19 shows mean MDLs in two orientations of 4 detectors.

		Detector 1		Detector 2		Detector 3		Detector 4	
		Coherent peak area	% error	Coherent peak area	% error	Coherent peak area	% error	Coherent peak area	% error
Skull to detector	1st	10665.00	1.43	10486.00	1.13	11585.00	1.06	10318.00	1.19
	2nd	8178.00	2.26	10672.00	1.11	12635.00	0.99	10492.00	1.11
	3rd	8424.00	1.46	8291.00	1.23	9925.00	1.12	8730.00	1.23
	4th	9923.00	1.29	10546.00	1.10	12663.00	0.98	12108.00	1.02
Hind to detector	1st	7253.00	1.87	8335.00	1.24	10209.00	1.09	8187.00	1.27
	2nd	7954.00	1.92	9942.00	1.19	12183.00	1.03	9860.00	1.16
	3rd	8142.00	1.57	8569.00	1.25	8887.00	1.21	7537.00	1.35
	4th	7949.00	1.49	10745.00	1.09	13753.00	0.95	9940.00	1.17

Table 2.17. Coherent peak areas with relative uncertainties obtained from C57BL/6J mice.

MDLs (µg Pb /g bone mineral)		From K-α	From K-β	Combined
Skull to detector	1st	7.72	14.29	6.80
	2nd	7.82	14.47	6.88
	3rd	8.53	15.76	7.50
	4th	7.53	13.94	6.64
Hind to detector	1st	8.69	16.08	7.65
	2nd	8.01	14.82	7.04
	3rd	8.81	16.30	7.75
	4th	7.79	14.40	6.85

Table 2.18. MDLs estimated for C57BL/6J mice using equation (2.16).

Mean MDLs (µg Pb /g bone mineral)	From K-α	From K-β	Combined
Skull to detector	7.99	14.76	7.02
Hind to detector	8.41	15.55	7.40

Table 2.19. Mean MDLs for C57BL/6J mice, which their skulls and hinds faced to the system
respectively.

2.9 Discussion

MDLs (µg Pb /g bone mineral)	Skull to detector		Hind to detector	
	CD-1 Mice	C57BL/6J Mice	CD-1 Mice	C57BL/6J Mice
From K-α	7.72	7.99	8.47	8.41
From K-β	14.28	14.76	15.67	15.55
Combined	6.79	7.02	7.45	7.40

Table 2.20. Summary of MDLs values calculated for 2 strains of mice (CD-1 and C57BL/6J).

The mean MDLs calculated for two strains of mice in two orientations (skull and hind) are summarized in Table 2.20. For a 3-hour measurement, we determined CD-1 mice with combined MDLs of 6.79 – 7.45 µg Pb /g bone mineral (with skull and hind facing the detectors respectively). We also determined C57BL/6J mice with combined MDLs of 7.02 – 7.40 µg Pb /g bone mineral. The mean mass of CD-1 mice is 46 ± 1 g, whereas the mean mass of C57BL/6J mice is 20 ± 1 g. The differences in combined MDL between 2 strains of mice are 0.23 (skull to detectors) and 0.05 (hind to detectors) respectively. As the mass of CD-1 mice is twice than that of C57BL/6J mice, the combined MDL differences are considered as relatively small. Hence, our XRF system could detect a sample with a mass from 20 to 40 grams.

A relationship of MDL $\propto 1/\sqrt{t}$ was used (Lord et al., 2016) to scale the time from 3 hours measurement in pre-existing bone Pb phantoms.

$$Estimate\ MDL = MDL\ from\ 3\ hours\ measurement \times \sqrt{\frac{3}{16}}$$

$$Estimate\ MDL = MDL\ from\ 3\ hours\ measurement \times \frac{\sqrt{3}}{4} --- (2.17)$$

Summary of projected MDLs for 16-hour count time for Pb free mice is shown in table 2.21.

	Skull to Detector		Hind to Detector	
	CD-1 Mice	C57BL/6J Mice	CD-1 Mice	C57BL/6J Mice
From K-α	3.34	3.46	3.67	3.64
From K-β	6.18	6.39	6.78	6.73
Combined	2.94	3.04	3.23	3.20

Table 2.21. Summary of projected MDLs for 2 strains of mice (CD-1 and C57BL/6J).

As shown in table 2.21, given a longer count time, combined MDLs fall from 6.79 – 7.02 to 2.94 – 3.04 (skull to detector) and from 7.40 – 7.45 to 3.20 – 3.23 (hind to detector) respectively. These MDL values not only provide estimation for long hours count, but also show that an overnight XRF measurement (16-hour measurement) will result in a more precise detection of Pb in mice.

2.10   Conclusion

To sum up, we have performed two different measurements. A set of pre-existing bone Pb phantoms was first measured for system calibration. After that, minimum detection limits (MDLs) were calculated which indicated as the lowest Pb concentration that our XRF system can detect. Detection limits for the bone phantoms, were found to be 1.52 ppm for 1-hour measurement. By comparison, using 2 strains of Pb free mice, CD-1 and C57BL/6J, we determined MDLs of 5.66 – 7.78 ppm and 6.69 – 8.50 ppm in whole mice (with skull and hind facing the detector respectively) for a 3-hour measurement. Our results indicated that we could proceed to make mouse-mimicking bone Pb phantoms to verify whether our system is applicable to measure Pb in whole mice in vivo.

CHAPTER 3

Mouse-mimicking Bone Pb Phantoms

3.1 Introduction

In the previous chapter, I discussed the measurement of a set of pre-existing bone Pb phantoms and two strains of mice. In that work, calibration of the x-ray/coherent ratio was performed by using the pre-existing phantoms and detection limits were obtained for 3-hour measurements of the mice. In order to evaluate the feasibility of using the ^{109}Cd XRF system for the measurement of Pb in the skeleton of whole mice, mouse-mimicking Plaster of Paris phantoms were developed. This allowed me to assess the effect of potential variations in Pb distribution across the mouse and thus discuss the applicability of the x-ray to coherent normalization in mice.

3.2 Materials and Methods

In order to study any differences in signal potentially resulting from a Pb distribution across the mouse, a set of 5 mouse mimicking Plaster of Paris (PoP) and paraffin wax phantoms were prepared. Plaster of Paris was used to simulate 'bones' and paraffin wax simulated soft tissue. The outer body of the mouse was represented by clear plastic cylindrical containers (30 mL, Nalgene® FEP bottle, Sigma-Aldrich) with a length of 60 mm, a diameter of 30 mm, and a wall thickness of 1 mm. This was assumed to be a fair approximation to mice, because the masses of the two strains of mice are 44 g and 20 g respectively.

Each of the 5 cylindrical phantoms had Plaster of Paris inserts to represent 'bones' doped with specific concentrations of Pb for XRF measurement. A lead stock solution was diluted in nitric acid (Lead Standard for Atomic Absorption Spectroscopy, Sigma-Aldrich) to obtain various Pb concentrations prior to mixing with Plaster of Paris. Different concentrations: 0, 50 and 150 ppm were prepared and filled into 70 mm long pipette tips and left to set. The weight of Pb needed follows Aro et al., 1994's equation:

$$\text{Pb needed } (\mu g) = \text{ x g } (CaSO_2 \cdot 2H_2O) \times \text{ y } \mu g \text{ of } \frac{Pb}{g} \text{ of } CaSO_2 \cdot 2H_2O --- (3.1)$$

As shown in figure 3.1, a total number of 15 pipette tips ('bones') were prepared (0 ppm: 8 tips, 50 ppm: 6 tips and 150 ppm: 1 tip). The mass of each Plaster of Paris 'bone' (with plastic pipette tip) was measured and recorded in table 3.1. Four days were given for all of the 'bones' (of various Pb concentrations in Plaster of Paris) to dry thoroughly.

0 ppm 'Bones'	Mass (g)	Mean Mass (g)	50 ppm 'Bones'	Mass (g)	Mean Mass (g)	150 ppm 'Bones'	Mass (g)
1	1.91		1	1.73		1	1.57
2	2.08		2	1.53			
3	1.95		3	1.68	1.60		
4	1.92	1.94	4	1.56			
5	1.90		5	1.50			
6	1.92		6	1.60			
7	1.87						
8	1.94						

Table 3.1: The mass of each Plaster of Paris 'bone' (with plastic pipette tip) measured by a portable electronic balance (Scout[TM] Pro, OHAUS).

For the consistency and to allow comparisons, all of the 'bones' were cut after drying and kept to a length of 37 mm. Super Glue (Cyanoacrylate) was applied to the top and bottom of the 'bones' and they were inserted into the plastic container. Each plastic container

contains 3 'bones' and represents different Pb concentration distributions across a mouse (figure 3.2). This is a relatively crude and exaggerated phantom model of a mouse. It is not realistic to assume that Pb distributions would be so extremely heterogenous in a real mouse on this centimeter scale. However, these phantoms permit testing of the effect of major differences in Pb distribution on the overall calculated Pb signal. If the system can accurately estimate the average Pb level in this model, even when the distribution is so extreme, it can presumably accurately estimate the average Pb level in a mouse.

Two days were given for 'bones' to dry into place in an upright position in the plastic container. At this point, paraffin wax was melted and used to fill in the plastic container as a simulation of soft tissue. The theoretical calculations of the average concentrations in the 5 phantoms are given in the table below (Table 3.2). A photograph of all of the mouse-mimicking phantoms is shown in Figure 3.3, and as can be seen indicator of the 'bones' Pb concentration and location were marked on the outside of the containers.

Mouse-mimicking phantoms	Overall concentrations (ppm)	Total Mass (g)
3 'bones' of 50 ppm	50	40.32
1 'bone' of 150 ppm, 2 'bones' of 0 ppm	50	41.52
2 'bones' of 50 ppm, 1 'bone' of 0 ppm	33	39.22
1 'bone' of 50 ppm, 2 'bones' of 0 ppm	17	41.77
3 'bones' of 0 ppm	0	41.54

Table 3.2. 5 mouse-mimicking phantoms were made and intended to permit study of the effects of extreme heterogenous distribution of Pb in a mouse.

Figure 3.1: 15 'bones' were made; they are Plaster of Paris (PoP) with a specific Pb concentration (0 ppm, 50 ppm or 150 ppm). Each of them was cut and kept to a length of 37 mm for consistency.
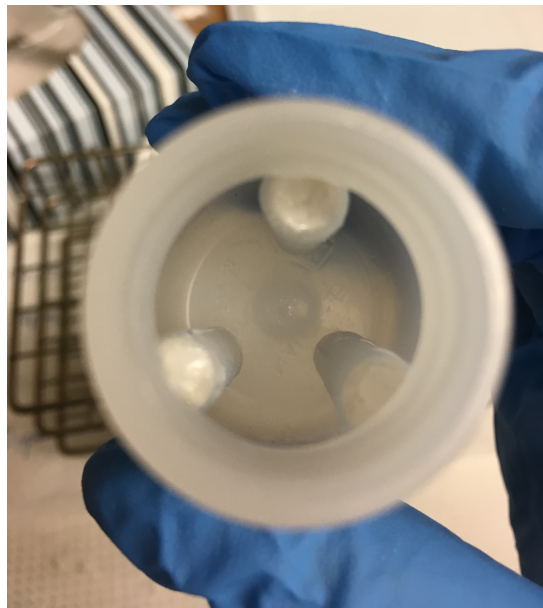
Figure 3.2: Each plastic container contains 3 'bones' of (potentially) different Pb concentrations to create extreme heterogenous distributions of Pb across a 'mouse'.

Figure 3.3: 5 mouse-mimicking bone Pb phantoms were prepared with and average concentrations of 0, 16.67, 33.33 and 50 ppm respectively.

3.3 Experimental Setup

Similar to the previously described measurements of the pre-existing bone Pb phantoms and the cadavers of two strains of mice, spectra were also collected for 5 mouse-mimicking bone phantoms. An illustration of the internal layout of a mouse-mimicking phantom is presented in Figure 3.4. Each phantom was rotated and measured in 7 positions as illustrated in Figure 3.5. A counting time of 1-hour for each position was used. There were thus 7 measurements of 5 phantoms and so a total number of 35 measurements were obtained. The source-to-sample distance remained at 5 mm as described in the previous chapter. Top view and side view of mouse-mimicking measurement are presented in Figure 3.6A and Figure 3.6B.
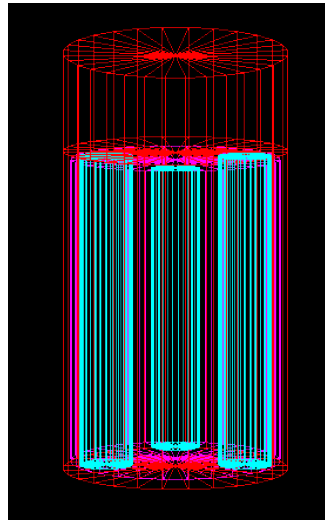
Figure 3.4: An illustration of the layout of a mouse-mimicking phantom with positions of the Plaster of Paris 'bones'.
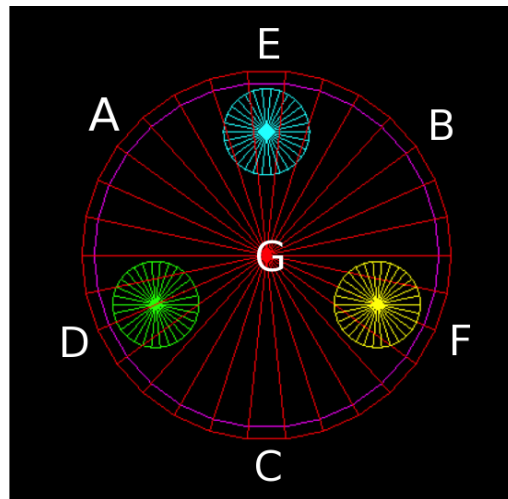
Figure 3.5: Each mouse-mimicking bone phantom was measured in 7 positions. Letters (A–G) indicate the location nearest detectors in each measurement.
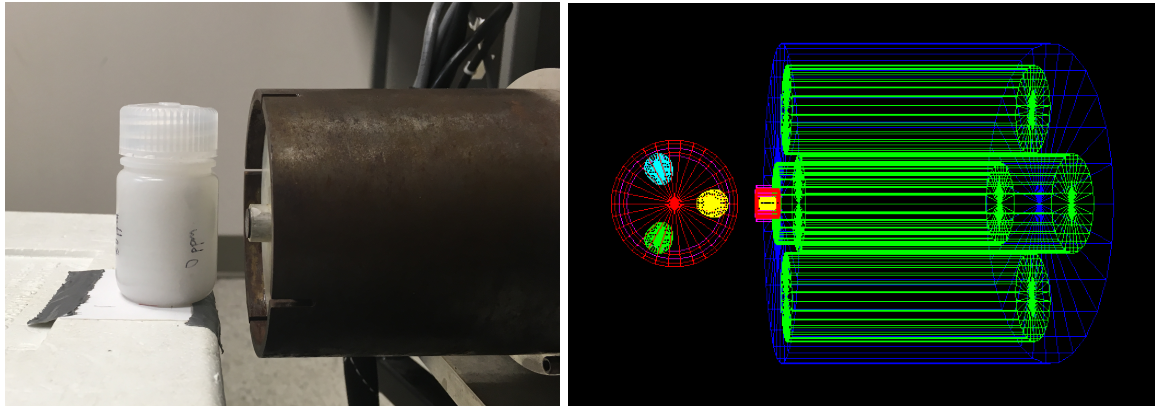
Figure 3.6A: Photograph and schematic of the side view and top view of the mouse-mimicking phantom. The source-to-phantom distance was remained at 5 mm as in earlier studies.
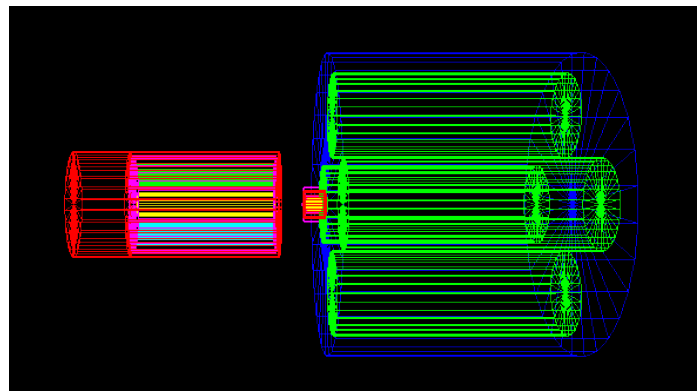
Figure 3.6B: A top view illustration of the mouse-mimicking phantom measurement with position G (shown in Figure 3.5) nearest the detector.

3.4 Fitting Results using R

3.4.1 Extreme Heterogenous Distribution of Pb

Below, in a series of five tables, are the results using the R code to fit the 5 mouse-mimicking bone Pb phantoms. As stated earlier, each phantom was measured in 7 positions and the source-to-phantom distance was kept to 5 mm. A position noted in the table with an asterisk indicates a measurement with a 'bone' located nearest the detector. There is thus a table of data for each phantom, with the $K\alpha$, $K\beta$, and coherent amplitudes obtained from the fit, for each of the four detectors in the cloverleaf system.

Position	Peak Amplitude	Detector 1	±	Detector 2	±	Detector 3	±	Detector 4	±
				3 'bones' of 50 ppm phantom					
A	Coherent	549.37	6.00	393.24	4.50	572.78	5.72	633.00	6.44
	$K\alpha_1$	172.78	17.51	108.25	12.70	145.04	15.76	123.65	18.08
	$K\beta_1$	41.70	4.60	27.02	3.69	39.65	3.23	37.04	5.14
B	Coherent	567.01	5.86	442.69	3.03	525.72	4.35	539.48	6.40
	$K\alpha_1$	175.26	19.10	132.31	16.98	110.24	14.41	153.79	16.40
	$K\beta_1$	33.00	4.69	29.04	3.55	30.74	4.50	33.74	4.34
C	Coherent	368.68	3.97	330.55	4.63	342.64	5.30	318.44	4.56
	$K\alpha_1$	106.81	19.88	104.91	13.56	110.06	11.67	85.10	16.47
	$K\beta_1$	26.05	3.26	22.47	3.67	14.45	3.63	21.21	3.35
D*	Coherent	515.19	4.59	349.10	4.26	469.08	3.69	728.17	7.37
	$K\alpha_1$	183.80	18.73	94.51	13.64	144.47	14.93	208.15	14.61
	$K\beta_1$	28.35	4.30	18.97	3.17	25.07	4.03	43.32	5.00
E*	Coherent	481.43	4.39	462.05	5.23	467.39	3.88	598.43	5.58
	$K\alpha_1$	130.09	15.49	161.14	11.45	138.06	13.42	160.87	13.92
	$K\beta_1$	28.09	3.85	31.56	3.82	36.29	2.79	36.34	3.23
F*	Coherent	593.75	5.39	632.22	5.53	479.44	4.32	611.50	5.31
	$K\alpha_1$	152.54	20.29	151.99	15.89	125.43	13.64	158.37	17.86
	$K\beta_1$	39.88	3.81	39.17	3.86	33.57	3.93	35.05	3.80
G	Coherent	620.21	4.58	459.93	4.30	457.83	2.82	511.71	4.80
	$K\alpha_1$	151.15	15.85	130.36	15.07	144.27	10.95	124.13	15.58
	$K\beta_1$	37.40	4.14	26.79	3.46	26.02	3.59	30.10	3.64

Table 3.3 Peak amplitude results obtained by using the R code to fit the data for 3 'bones' of the 50 ppm phantom.

3 'bones' of 0 ppm phantom									
Position	Peak Amplitude	Detector 1	±	Detector 2	±	Detector 3	±	Detector 4	±
A	Coherent	562.07	5.14	388.40	4.23	543.93	4.66	596.84	6.59
	$K\alpha_1$	3.93	17.43	24.63	13.06	17.74	15.38	31.99	15.85
	$K\beta_1$	1.27	2.45	0.41	2.22	0.85	2.40	-1.56	2.50
B	Coherent	615.39	5.41	386.17	3.53	506.36	4.93	649.84	4.16
	$K\alpha_1$	7.66	20.65	-6.83	16.00	-5.66	14.25	26.74	17.66
	$K\beta_1$	-1.83	2.56	3.18	2.33	0.18	2.33	3.66	2.67
C	Coherent	509.06	4.33	412.74	6.69	440.38	4.63	477.21	4.40
	$K\alpha_1$	6.75	18.81	15.40	22.79	-21.00	14.34	-9.40	15.33
	$K\beta_1$	5.20	2.49	3.18	2.25	0.06	2.12	-3.40	2.44
D	Coherent	848.92	6.57	767.14	4.51	686.59	6.53	939.00	7.36
	$K\alpha_1$	-5.20	19.77	-6.69	15.12	-25.58	13.93	6.61	15.92
	$K\beta_1$	-5.32	2.66	-0.58	2.54	-1.20	2.44	5.17	2.90
E	Coherent	805.33	7.80	750.75	5.53	661.34	6.35	940.32	7.84
	$K\alpha_1$	-26.10	20.86	-5.94	14.26	17.40	13.37	37.82	15.60
	$K\beta_1$	-2.72	2.64	2.94	2.55	0.51	2.42	1.21	2.83
F	Coherent	782.62	5.25	719.58	5.12	593.41	4.86	913.51	5.16
	$K\alpha_1$	-9.43	16.95	-25.24	14.74	-26.80	15.70	35.59	18.15
	$K\beta_1$	-2.76	2.62	-0.15	2.50	3.50	2.41	1.88	2.82
G	Coherent	604.92	4.16	422.15	5.42	402.24	4.25	651.90	4.97
	$K\alpha_1$	5.38	16.21	41.13	21.35	12.42	11.52	-14.52	18.53
	$K\beta_1$	4.63	2.53	3.96	2.28	5.03	2.24	5.37	2.59

Table 3.4. Peak amplitude results obtained by using the R code to fit the data for 3 'bones' of the 0 ppm phantom.

1 'bone' of 50 ppm, 2 'bones' of 0 ppm phantom									
Position	Peak Amplitude	Detector 1	±	Detector 2	±	Detector 3	±	Detector 4	±
A	Coherent	579.81	5.36	576.15	6.29	551.82	4.61	467.87	4.40
	$K\alpha_1$	57.42	15.72	28.21	14.45	39.26	13.30	92.99	14.54
	$K\beta_1$	19.38	4.70	6.17	3.09	19.07	3.55	15.98	3.09
B	Coherent	434.65	5.60	386.08	4.59	424.48	4.20	398.66	4.33
	$K\alpha_1$	51.82	17.66	63.29	14.27	55.17	12.59	31.77	15.78
	$K\beta_1$	11.20	3.38	14.53	3.43	15.58	3.52	1.65	3.54
C	Coherent	551.29	5.07	496.35	4.51	496.32	4.51	422.45	5.06
	$K\alpha_1$	17.10	18.79	16.21	15.14	11.51	14.71	40.46	14.92
	$K\beta_1$	9.75	4.04	5.64	2.72	6.81	3.49	5.03	3.53
D	Coherent	698.27	7.28	859.64	4.73	632.11	4.44	594.72	5.61
	$K\alpha_1$	37.29	20.22	17.50	16.87	57.69	13.24	38.48	13.92
	$K\beta_1$	8.46	4.02	10.24	3.54	14.66	2.81	12.42	3.28
E*	Coherent	586.98	5.45	653.38	5.88	530.60	3.16	595.53	6.30
	$K\alpha_1$	127.75	14.88	155.97	12.21	114.97	13.17	133.55	14.31
	$K\beta_1$	26.91	3.94	34.35	3.61	22.43	3.66	33.57	4.42
F	Coherent	647.87	4.73	433.56	3.57	570.52	5.84	930.74	8.83
	$K\alpha_1$	43.58	16.76	40.28	12.55	49.65	12.11	31.28	19.57
	$K\beta_1$	6.14	3.48	9.51	3.20	9.45	2.71	4.72	3.62
G	Coherent	696.84	4.52	636.07	5.62	298.58	3.84	588.78	4.00
	$K\alpha_1$	7.44	19.06	9.19	15.48	-2.29	14.86	-5.75	18.12
	$K\beta_1$	4.59	3.59	0.51	3.93	3.81	2.84	7.48	2.89

Table 3.5 Peak amplitude results obtained by using the R code to fit the data for 'bone' of the 50 ppm, 2 'bones' of 0 ppm phantom.

2 'bones' of 50 ppm, 1 'bone' of 0 ppm phantom									
Position	Peak Amplitude	Detector 1	±	Detector 2	±	Detector 3	±	Detector 4	±
A	Coherent	597.52	4.84	332.19	3.82	518.04	5.05	686.09	4.55
	$K\alpha_1$	43.84	18.49	75.36	14.16	63.67	15.19	46.36	15.94
	$K\beta_1$	15.66	3.12	13.53	3.80	15.48	3.05	12.48	3.51
B	Coherent	606.63	6.28	551.45	4.56	526.21	4.57	492.87	5.64
	$K\alpha_1$	99.41	17.06	22.85	12.42	80.10	13.79	85.33	17.46
	$K\beta_1$	25.62	3.73	12.33	3.45	18.98	3.71	25.61	3.97
C	Coherent	379.21	4.23	369.03	5.13	356.72	3.70	291.54	4.30
	$K\alpha_1$	73.75	19.13	96.17	13.65	86.02	13.50	87.74	12.80
	$K\beta_1$	19.59	3.48	15.25	3.62	22.44	3.01	15.46	2.96
D*	Coherent	636.60	4.12	671.97	5.08	671.97	5.08	655.64	4.40
	$K\alpha_1$	127.09	18.16	178.68	16.76	128.82	12.79	140.26	16.43
	$K\beta_1$	37.54	4.13	40.65	3.96	26.06	4.12	36.52	4.07
E	Coherent	835.89	6.47	739.91	5.32	650.03	5.83	897.83	4.33
	$K\alpha_1$	46.01	18.25	32.29	14.87	38.26	13.31	53.77	15.42
	$K\beta_1$	18.26	3.52	18.89	3.65	9.18	3.28	21.19	4.37
F*	Coherent	711.36	6.74	808.34	4.53	527.13	5.33	603.21	6.00
	$K\alpha_1$	190.27	17.28	168.11	18.11	135.48	14.36	173.27	16.52
	$K\beta_1$	36.53	4.37	38.48	4.79	29.08	3.53	39.50	4.13
G	Coherent	821.80	5.39	592.66	4.43	479.66	4.10	600.83	5.69
	$K\alpha_1$	109.60	19.68	16.46	15.50	70.36	13.07	125.46	15.69
	$K\beta_1$	29.98	5.24	5.92	3.26	21.67	3.07	22.72	3.63

Table 3.6. Peak amplitude results obtained by using the R code to fit the data for 2 'bones' of the 50 ppm, 1 'bone' of 0 ppm phantom.

| 1 'bone' of 150 ppm, 2 'bones' of 0 ppm phantom | | | | | | | | | |
Position	Peak Amplitude	Detector 1	±	Detector 2	±	Detector 3	±	Detector 4	±
A	Coherent	613.08	6.62	548.04	5.06	492.93	5.57	472.00	5.04
	$K\alpha_1$	200.01	19.50	55.25	14.04	161.06	17.29	266.46	20.23
	$K\beta_1$	46.63	4.25	14.15	3.80	40.51	3.91	60.64	4.04
B	Coherent	628.74	5.64	406.07	5.10	517.54	5.33	682.80	5.33
	$K\alpha_1$	139.85	22.75	219.44	20.93	142.45	12.52	50.68	16.83
	$K\beta_1$	37.71	3.69	42.75	3.76	35.52	3.80	9.19	4.34
C	Coherent	619.25	5.51	645.35	6.27	490.12	6.00	419.40	3.98
	$K\alpha_1$	13.96	17.84	53.79	14.78	54.04	14.22	31.83	18.04
	$K\beta_1$	10.68	4.38	15.01	3.87	18.44	3.17	26.26	3.90
D	Coherent	975.31	6.05	850.39	7.31	657.33	4.78	1020.03	5.08
	$K\alpha_1$	109.72	19.77	44.39	17.04	106.59	12.60	137.18	19.10
	$K\beta_1$	28.59	4.70	17.75	4.15	23.06	3.35	34.16	5.20
E*	Coherent	892.57	7.99	811.75	5.33	601.15	5.95	790.79	6.69
	$K\alpha_1$	526.24	39.44	595.28	18.77	364.06	14.43	524.31	31.15
	$K\beta_1$	143.63	7.08	127.80	4.65	75.97	3.99	125.31	6.91
F	Coherent	1012.94	9.14	841.14	5.34	666.31	4.12	1036.60	4.96
	$K\alpha_1$	44.07	22.86	127.94	17.41	84.16	15.69	48.13	19.38
	$K\beta_1$	18.24	4.57	27.47	5.54	19.94	3.84	14.40	4.60
G	Coherent	734.69	3.90	446.86	4.25	472.35	4.21	699.60	6.46
	$K\alpha_1$	251.02	22.87	246.50	20.78	144.91	14.74	56.23	19.76
	$K\beta_1$	59.87	5.88	58.14	3.23	26.59	3.40	15.85	4.17

Table 3.7. Peak amplitude results obtained by using the R code to fit the data for 1 'bone' of the 150 ppm, 2 'bones' of 0 ppm phantom.

3.5 Data Analysis

3.5.1 Results of Measurement of Extreme Heterogenous Distribution of Pb

The reasoning behind the construction of the set of 5 phantoms with varying Pb distribution was to test whether the system could estimate the average concentration accurately. In this instance the question is would the measured average x-ray to coherent ratio be the same for a phantom of average concentration 50 ppm, made from 3 'bones' of 50 ppm as for a phantom also of average concentration 50 ppm, made from 1 bone of 150

ppm and two bones of 0 ppm? In this section, I present the x-ray: coherent data for each

phantom. In the next section, I will compare and discuss the measurements of different

phantoms.

Phantom with 3 'bones' of 50 ppm								
Position		Detector 1	±	Detector 2	±	Detector 3	±	Detector 4	±
A	$K\alpha_1$ / Coherent	0.315	0.032	0.275	0.032	0.253	0.028	0.195	0.029
	$K\beta_1$ / Coherent	0.076	0.008	0.069	0.009	0.069	0.006	0.059	0.008
B	$K\alpha_1$ / Coherent	0.309	0.034	0.299	0.038	0.210	0.027	0.285	0.031
	$K\beta_1$ / Coherent	0.058	0.008	0.066	0.008	0.058	0.009	0.063	0.008
C	$K\alpha_1$ / Coherent	0.290	0.054	0.317	0.041	0.321	0.034	0.267	0.052
	$K\beta_1$ / Coherent	0.071	0.009	0.068	0.011	0.042	0.011	0.067	0.011
D	$K\alpha_1$ / Coherent	0.357	0.036	0.271	0.039	0.308	0.032	0.286	0.020
	$K\beta_1$ / Coherent	0.055	0.008	0.054	0.009	0.053	0.009	0.059	0.007
E	$K\alpha_1$ / Coherent	0.270	0.032	0.349	0.025	0.295	0.029	0.269	0.023
	$K\beta_1$ / Coherent	0.058	0.008	0.068	0.008	0.078	0.006	0.061	0.005
F	$K\alpha_1$ / Coherent	0.257	0.034	0.240	0.025	0.262	0.029	0.259	0.029
	$K\beta_1$ / Coherent	0.067	0.006	0.062	0.006	0.070	0.008	0.057	0.006
G	$K\alpha_1$ / Coherent	0.244	0.026	0.283	0.033	0.315	0.024	0.243	0.031
	$K\beta_1$ / Coherent	0.060	0.007	0.058	0.008	0.057	0.008	0.059	0.007

Table 3.8A The K x-rays/coherent amplitude ratios for measurements of a phantom with 3 'bones' of 50 ppm phantom. Ratios calculated from results of R fits.

Figure 3.7 A plot of the Kα/coherent ratio for each detector at various positions on the phantom. Ratios were calculated from R-fitting data. It can be seen that the ratio measured in each detector does not strongly depend on phantom position.
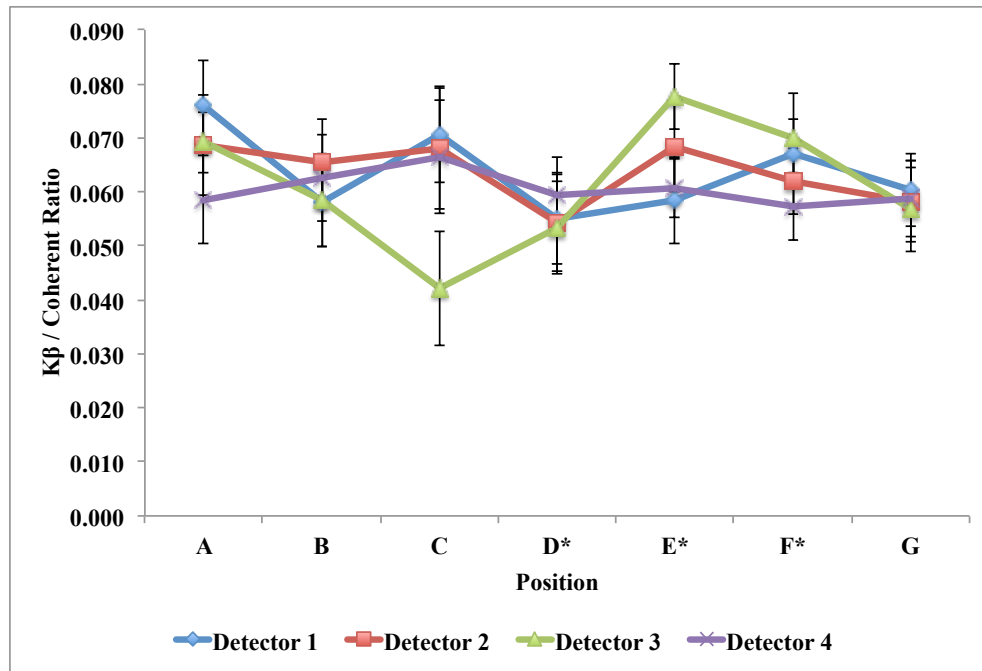
Figure 3.8 A plot of the Kβ/coherent ratio for each detector at various positions on the phantom. Ratios were calculated from R-fitting data. Similar to the Kα plot, it can be seen that the ratio measured in each detector does not strongly depend on phantom position.

Figure 3.9: The locations of 50 ppm 'bones' inside the phantom. They are located in position D, E and F respectively.

Phantom with 3 'bones' of 50 ppm		
	$K\alpha_1$ / Coherent	$K\beta_1$ / Coherent
Number of measurement	28.000	28.000
Mean	0.280	0.062
Standard Deviation	0.037	0.008
Minimum	0.195	0.042
Quartile 1 (Q1)	0.258	0.058
Median	0.279	0.061
Quartile 3 (Q3)	0.308	0.068
Maximum	0.357	0.078

Table 3.8B Calculated mean, standard deviation and quartiles for the x-ray/coherent ratios for the 3 'bones' of 50 ppm phantom using Excel's box-and-whisker plot function. The standard deviation is relatively small which again indicates that there is little variation in ratio with position.

Phantom with 3 'bones' of 0 ppm									
Position		Detector 1	±	Detector 2	±	Detector 3	±	Detector 4	±
A	$K\alpha_1$ / Coherent	0.007	0.031	0.063	0.034	0.033	0.028	0.054	0.027
	$K\beta_1$ / Coherent	0.002	0.004	0.001	0.006	0.002	0.004	-0.003	-0.004
B	$K\alpha_1$ / Coherent	0.012	0.034	-0.018	-0.041	-0.011	-0.028	0.041	0.027
	$K\beta_1$ / Coherent	-0.003	-0.004	0.008	0.006	0.000	0.005	0.006	0.004
C	$K\alpha_1$ / Coherent	0.013	0.037	0.037	0.055	-0.048	-0.033	-0.020	-0.032
	$K\beta_1$ / Coherent	0.010	0.005	0.008	0.005	0.000	0.005	-0.007	-0.005
D	$K\alpha_1$ / Coherent	-0.006	-0.023	-0.009	-0.020	-0.037	-0.020	0.007	0.017
	$K\beta_1$ / Coherent	-0.006	-0.003	-0.001	-0.003	-0.002	-0.004	0.006	0.003
E	$K\alpha_1$ / Coherent	-0.032	-0.026	-0.008	-0.019	0.026	0.020	0.040	0.017
	$K\beta_1$ / Coherent	-0.003	-0.003	0.004	0.003	0.001	0.004	0.001	0.003
F	$K\alpha_1$ / Coherent	-0.012	-0.022	-0.035	-0.020	-0.045	-0.026	0.039	0.020
	$K\beta_1$ / Coherent	-0.004	-0.003	0.000	-0.003	0.006	0.004	0.002	0.003
G	$K\alpha_1$ / Coherent	0.009	0.027	0.097	0.051	0.031	0.029	-0.022	-0.028
	$K\beta_1$ / Coherent	0.008	0.004	0.009	0.005	0.013	0.006	0.008	0.004

Table 3.9A The K x-rays/coherent amplitude ratios for measurements of a phantom with 3 'bones' of 0 ppm phantom. Ratios calculated from results of R fits.
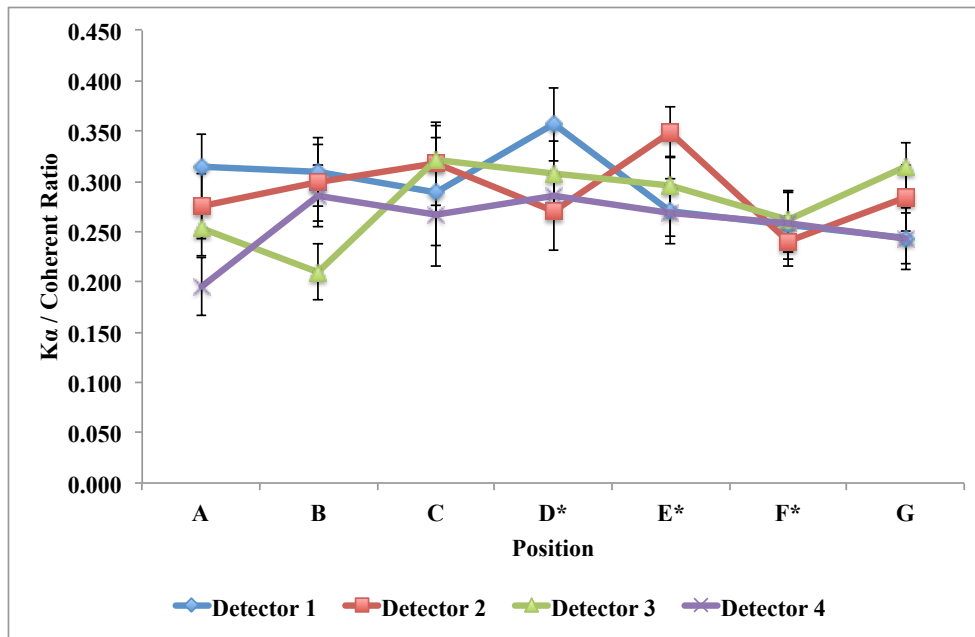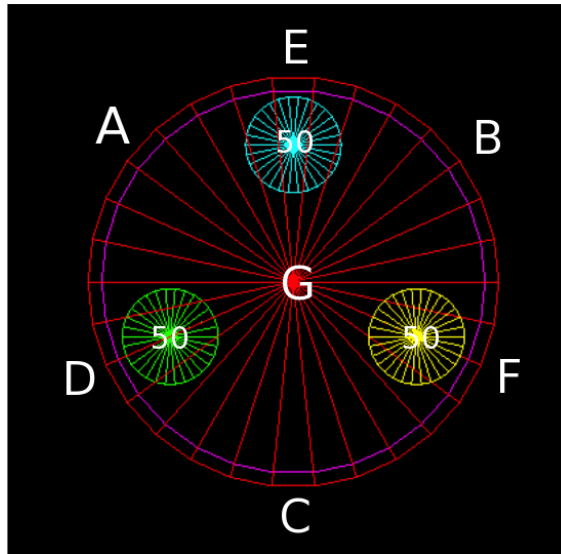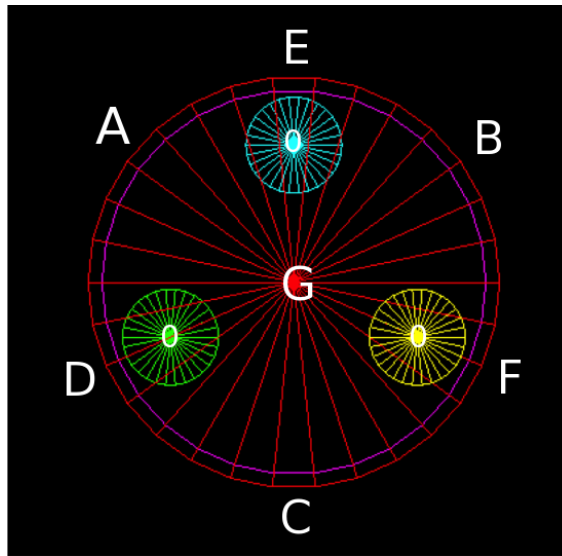

Figure 3.10: The locations of 0 ppm 'bones' inside the phantom. They are located in position D, E and F respectively.

Phantom with 3 'bones' of 0 ppm		
	$K\alpha_1$ / Coherent	$K\beta_1$ / Coherent
Number of measurement	28.000	28.000
Mean	0.007	0.002
Standard Deviation	0.035	0.005
Minimum	-0.048	-0.007
Quartile 1 (Q1)	-0.018	-0.001
Median	0.007	0.001
Quartile 3 (Q3)	0.034	0.006
Maximum	0.097	0.013

Table 3.9B Calculated mean, standard deviation and quartiles for the x-ray/coherent ratios for the 3 'bones' of 0 ppm phantom using Excel's box-and-whisker function. The standard deviation is relatively small which again indicates that there is little variation in ratio with position.

Phantom with 1 'bone' of 50 ppm and 2 'bones' of 0 ppm									
Position		Detector 1	±	Detector 2	±	Detector 3	±	Detector 4	±
A	$K\alpha_1$ / Coherent	0.099	0.027	0.049	0.025	0.071	0.024	0.199	0.031
	$K\beta_1$ / Coherent	0.033	0.008	0.011	0.005	0.035	0.006	0.034	0.007
B	$K\alpha_1$ / Coherent	0.119	0.041	0.164	0.037	0.130	0.030	0.080	0.040
	$K\beta_1$ / Coherent	0.026	0.008	0.038	0.009	0.037	0.008	0.004	0.009
C	$K\alpha_1$ / Coherent	0.031	0.034	0.033	0.031	0.023	0.030	0.096	0.035
	$K\beta_1$ / Coherent	0.018	0.007	0.011	0.005	0.014	0.007	0.012	0.008
D	$K\alpha_1$ / Coherent	0.053	0.029	0.020	0.020	0.091	0.021	0.065	0.023
	$K\beta_1$ / Coherent	0.012	0.006	0.012	0.004	0.023	0.004	0.021	0.006
E	$K\alpha_1$ / Coherent	0.218	0.025	0.239	0.019	0.217	0.025	0.224	0.024
	$K\beta_1$ / Coherent	0.046	0.007	0.053	0.006	0.042	0.007	0.056	0.007
F	$K\alpha_1$ / Coherent	0.067	0.026	0.093	0.029	0.087	0.021	0.034	0.021
	$K\beta_1$ / Coherent	0.009	0.005	0.022	0.007	0.017	0.005	0.005	0.004
G	$K\alpha_1$ / Coherent	0.011	0.027	0.014	0.024	-0.008	-0.050	-0.010	-0.031
	$K\beta_1$ / Coherent	0.007	0.005	0.001	0.006	0.013	0.010	0.013	0.005

Table 3.10A The K x-rays/coherent amplitude ratios for measurements of a phantom with 1 'bone' of 50 ppm, 2 'bones' of 0 ppm phantom. Ratios calculated from results of R fits.

Figure 3.11: The locations of 50 ppm 'bone' and 0 ppm 'bones' inside the phantom. The 50 ppm 'bone' is located in position E, whereas 0 ppm 'bones' are located in position D and F.

Phantom with 1 'bone' of 50 ppm and 2 'bones' of 0 ppm		
	$K\alpha_1$ / Coherent	$K\beta_1$ / Coherent
Number of measurement	28.000	28.000
Mean	0.090	0.022
Standard Deviation	0.074	0.015
Minimum	-0.010	0.001
Quartile 1 (Q1)	0.032	0.012
Median	0.075	0.017
Quartile 3 (Q3)	0.122	0.034
Maximum	0.239	0.056

Table 3.10B Calculated mean, standard deviation and quartiles for the x-ray/coherent ratios for the 1 'bone' of 50 ppm, 2 'bones' of 0 ppm phantom using Excel's box-and-whisker function. The standard deviation is relatively large which indicates that there is a large variation in ratio with position. Position E has the highest ratio, followed by position A and B, while position C, D and F are about the same.

Phantom with 2 'bones' of 50 ppm and 1 'bone' of 0 ppm									
Position		Detector 1	±	Detector 2	±	Detector 3	±	Detector 4	±
A	$K\alpha_1$ / Coherent	0.073	0.031	0.227	0.043	0.123	0.029	0.068	0.023
	$K\beta_1$ / Coherent	0.026	0.005	0.041	0.011	0.030	0.006	0.018	0.005
B	$K\alpha_1$ / Coherent	0.164	0.028	0.041	0.023	0.152	0.026	0.173	0.035
	$K\beta_1$ / Coherent	0.042	0.006	0.022	0.006	0.036	0.007	0.052	0.008
C	$K\alpha_1$ / Coherent	0.194	0.050	0.261	0.037	0.241	0.038	0.301	0.044
	$K\beta_1$ / Coherent	0.052	0.009	0.041	0.010	0.063	0.008	0.053	0.010
D	$K\alpha_1$ / Coherent	0.200	0.029	0.266	0.025	0.192	0.019	0.214	0.025
	$K\beta_1$ / Coherent	0.059	0.006	0.060	0.006	0.039	0.006	0.056	0.006
E	$K\alpha_1$ / Coherent	0.055	0.022	0.044	0.020	0.059	0.020	0.060	0.017
	$K\beta_1$ / Coherent	0.022	0.004	0.026	0.005	0.014	0.005	0.024	0.005
F	$K\alpha_1$ / Coherent	0.267	0.024	0.208	0.022	0.257	0.027	0.287	0.028
	$K\beta_1$ / Coherent	0.051	0.006	0.048	0.006	0.055	0.007	0.065	0.007
G	$K\alpha_1$ / Coherent	0.133	0.024	0.028	0.026	0.147	0.027	0.209	0.026
	$K\beta_1$ / Coherent	0.036	0.006	0.010	0.006	0.045	0.006	0.038	0.006

Table 3.11A The K x-rays/coherent amplitude ratios for measurements of a phantom with 2 'bones' of 50 ppm, 1 'bone' of 0 ppm phantom. Ratios calculated from results of R fits.
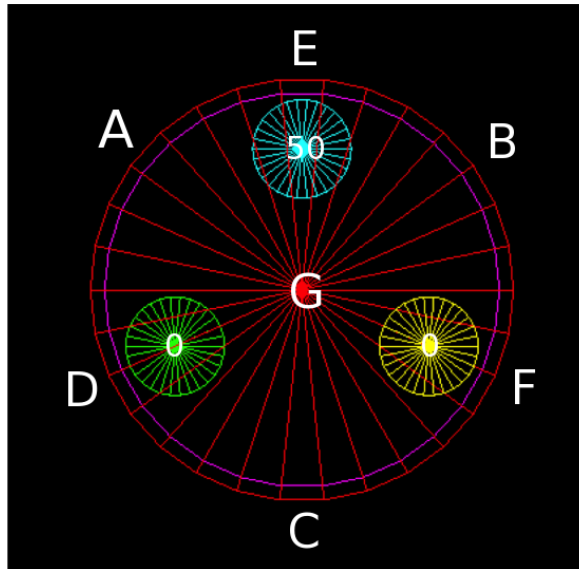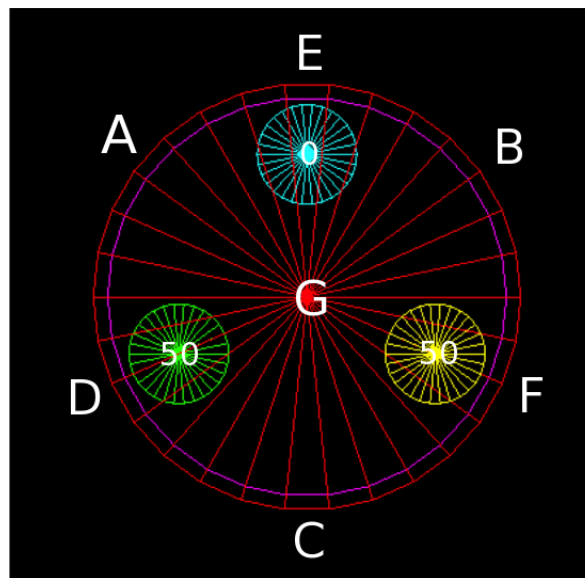

Figure 3.12: The locations of 50 ppm 'bones' and 0 ppm 'bone' inside the phantom. The 50 ppm 'bones' are located in position D and F, whereas 0 ppm 'bone' is located in position E.

Phantom with 2 'bones' of 50 ppm and 1 'bone' of 0 ppm		
	$K\alpha_1$ / Coherent	$K\beta_1$ / Coherent
Number of Measurement	28.000	28.000
Mean	0.166	0.040
Standard Deviation	0.085	0.016
Minimum	0.028	0.010
Quartile 1 (Q1)	0.072	0.026
Median	0.182	0.041
Quartile 3 (Q3)	0.230	0.052
Maximum	0.301	0.065

Table 3.11B Calculated mean, standard deviation and quartiles for the x-ray/coherent ratios for the 2 'bones' of 50 ppm, 1 'bone' of 0 ppm phantom using Excel's box-and-whisker function. The standard deviation is relatively large which again indicates that there is large variation in ratio with position.

Phantom with 1 'bone' of 150 ppm and 2 'bones' of 0 ppm									
Position		Detector 1	±	Detector 2	±	Detector 3	±	Detector 4	±
A	$K\alpha_1$ / Coherent	0.326	0.032	0.101	0.026	0.327	0.035	0.565	0.043
	$K\beta_1$ / Coherent	0.076	0.007	0.026	0.007	0.082	0.008	0.128	0.009
B	$K\alpha_1$ / Coherent	0.222	0.036	0.540	0.052	0.275	0.024	0.074	0.025
	$K\beta_1$ / Coherent	0.060	0.006	0.105	0.009	0.069	0.007	0.013	0.006
C	$K\alpha_1$ / Coherent	0.023	0.029	0.083	0.023	0.110	0.029	0.076	0.043
	$K\beta_1$ / Coherent	0.017	0.007	0.023	0.006	0.038	0.006	0.063	0.009
D	$K\alpha_1$ / Coherent	0.112	0.020	0.052	0.020	0.162	0.019	0.134	0.019
	$K\beta_1$ / Coherent	0.029	0.005	0.021	0.005	0.035	0.005	0.033	0.005
E	$K\alpha_1$ / Coherent	0.590	0.045	0.733	0.024	0.606	0.025	0.663	0.040
	$K\beta_1$ / Coherent	0.161	0.008	0.157	0.006	0.126	0.007	0.158	0.009
F	$K\alpha_1$ / Coherent	0.044	0.023	0.152	0.021	0.126	0.024	0.046	0.019
	$K\beta_1$ / Coherent	0.018	0.005	0.033	0.007	0.030	0.006	0.014	0.004
G	$K\alpha_1$ / Coherent	0.342	0.031	0.552	0.047	0.307	0.031	0.080	0.028
	$K\beta_1$ / Coherent	0.081	0.008	0.130	0.007	0.056	0.007	0.023	0.006

Table 3.12A The K x-rays/coherent amplitude ratios for measurements of a phantom with 1 'bone' of 150 ppm, 2 'bones' of 0 ppm phantom. Ratios calculated from results of R fits.

Figure 3.13 A plot of the Kα/coherent ratio for each detector at various positions on the phantom. Ratios were calculated from R-fitting data. It can be seen that the ratio does strongly depend on phantom position for this extremely heterogeneous phantom. All four detectors register the highest Kα/coherent ratio at the position where the highest Pb concentration phantom is nearest the detector.
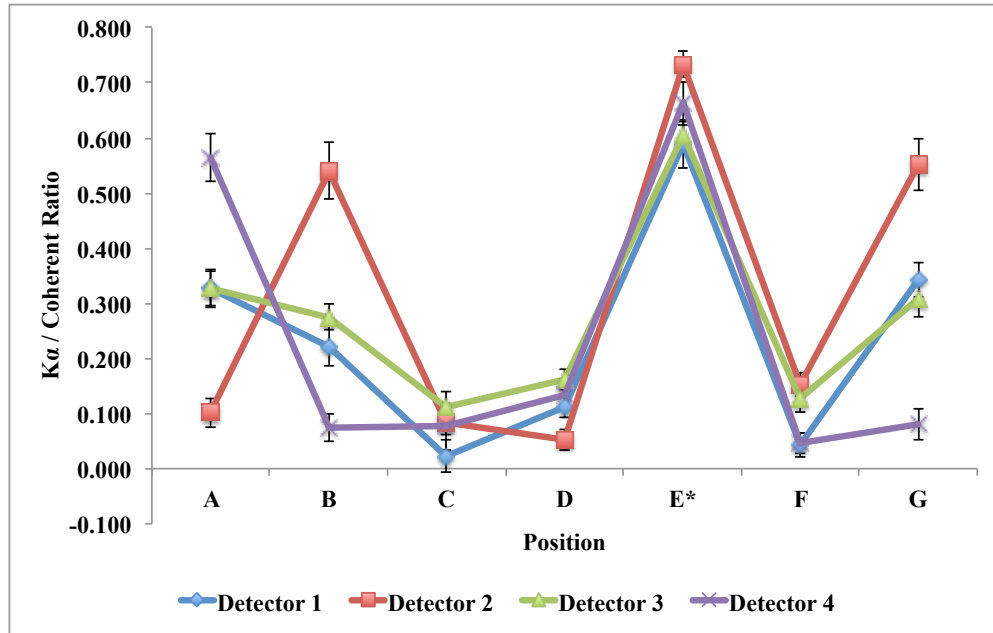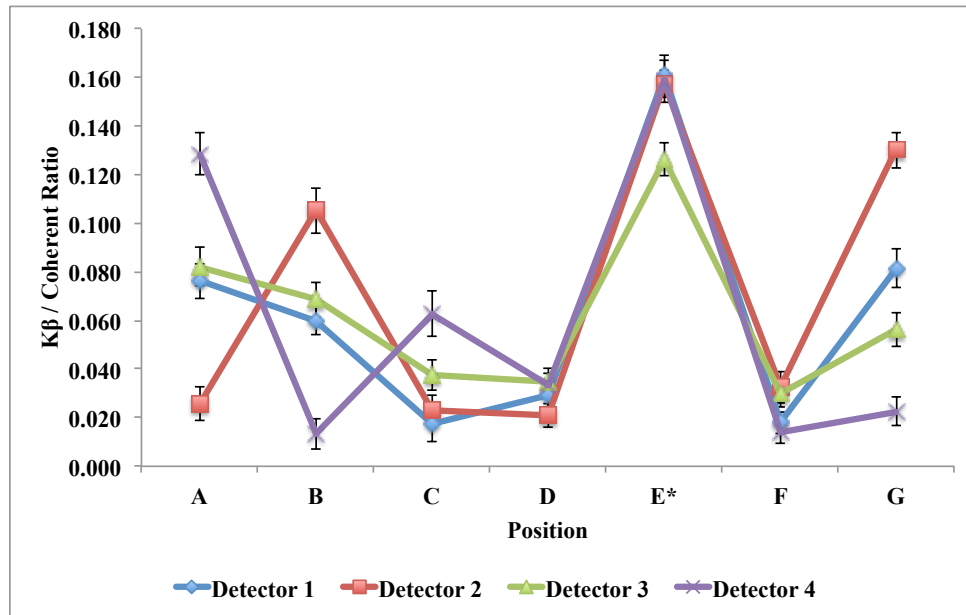
Figure 3.14 A plot of the Kβ/coherent ratio for each detector at various positions on the phantom. Ratios were calculated from R-fitting data. Similar to the Kα plot, it can be seen that the ratio does strongly depend on phantom position for this extremely heterogeneous phantom. All four detectors register the highest Kβ/coherent ratio at the position where the highest Pb concentration phantom is nearest the detector.
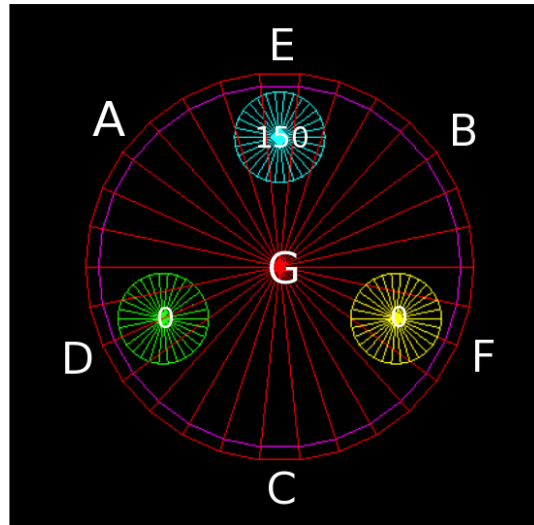

Figure 3.15: The locations of 150 ppm 'bone' and 0 ppm 'bones' inside the phantom. The 150 ppm 'bone' is located in position E, whereas 0 ppm 'bones' are located in position D and F.

1 'bone' of 150 ppm, 2 'bones' of 0 ppm phantom		
	$K\alpha_1$ / Coherent	$K\beta_1$ / Coherent
Number of Measurement	28.000	28.000
Mean	0.265	0.065
Standard Deviation	0.223	0.049
Minimum	0.023	0.013
Quartile 1 (Q1)	0.083	0.025
Median	0.157	0.047
Quartile 3 (Q3)	0.391	0.088
Maximum	0.733	0.161

Table 3.12B Calculated mean, standard deviation and quartiles for the x-ray/coherent ratios for the 1 'bone' of 150 ppm, 2 'bones' of 0 ppm phantom using Excel's box-and-whisker function. The standard deviation is the largest, which indicates that there is a huge variation in ratio with position.

3.6 Discussion

In the previous section, data were presented for each detector for each individual phantom. In this section, I now compare the signals obtained from different phantoms to each other. A box plot showing the mean peak amplitude ratios, i.e the mean x-ray to coherent ratio of the four detectors for each of the 7 positions of the 5 phantoms is displayed in figure 3.16. A comparison of the variation of the peak amplitude ratio across 7 positions of 2 phantoms that should contain the same total mass of Pb and Plaster of Paris (3 'bones' of 50 ppm; 1 'bone' of 150 ppm and 2 'bones' of 0 ppm) is shown in figure 3.18. In addition, a comparison of the variation of the peak amplitude ratio across 7 positions of 2 other phantoms that should also contain 1/3 of total mass of Pb and Plaster of Paris (1 'bone' of 150 ppm and 2 'bones' of 0 ppm; 1 'bone' of 50 ppm and 2 'bones' of 0 ppm) is shown in figure 3.21.
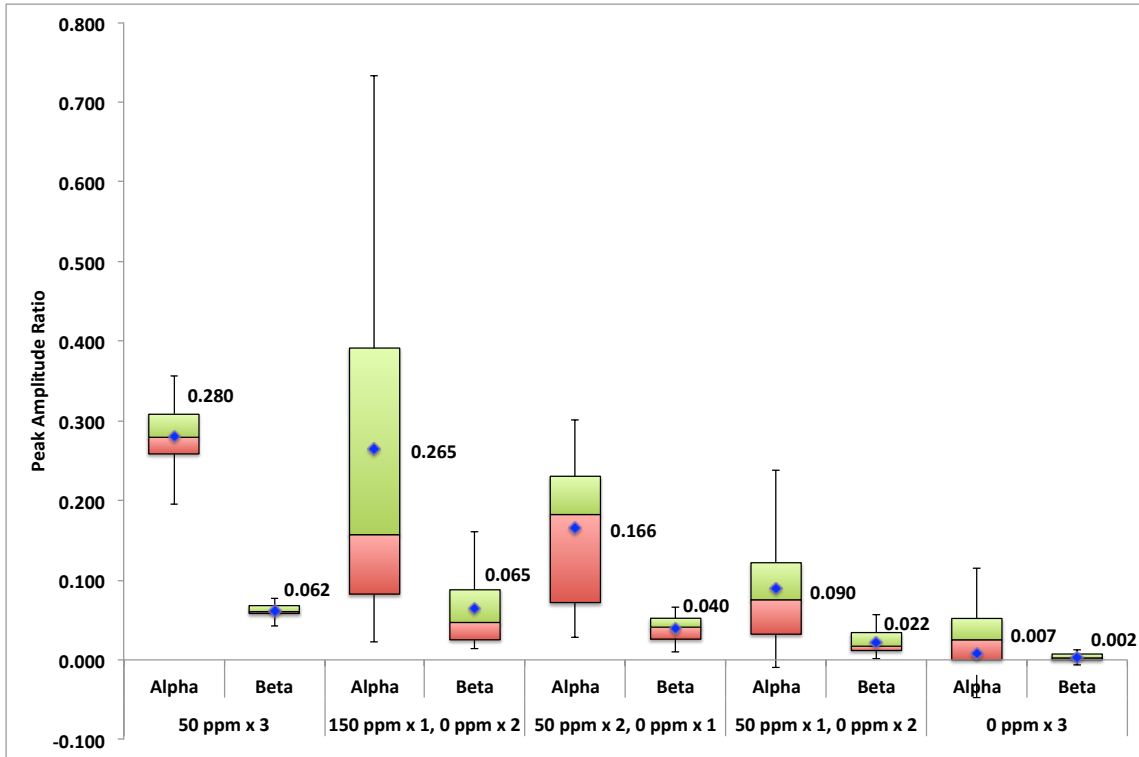
Figure 3.16: A box-and-whisker plot showing the mean peak amplitude ratios for the 7 positions of the 5 phantoms. The median for each peak amplitude ratio is represented in a blue marker.

These data are also plotted as a chart of averaged x-ray:coherent ratio versus average Pb concentration in Figure 3.17 below. This figure is included because it more clearly shows that the measured average x-ray:coherent ratios (for both α and β x-ray lines) seem to be independent of Pb distribution. All measured average ratios lie on a single straight line that is strongly predicted by the average concentration in the phantom. A linear regression of the average α:coherent ratio versus average concentration results in an R^2 value of 0.993 (p=0.0002) while linear regression of the average β:coherent ratio versus average concentration results in an R^2 value of 0.997 (p=0.0001).
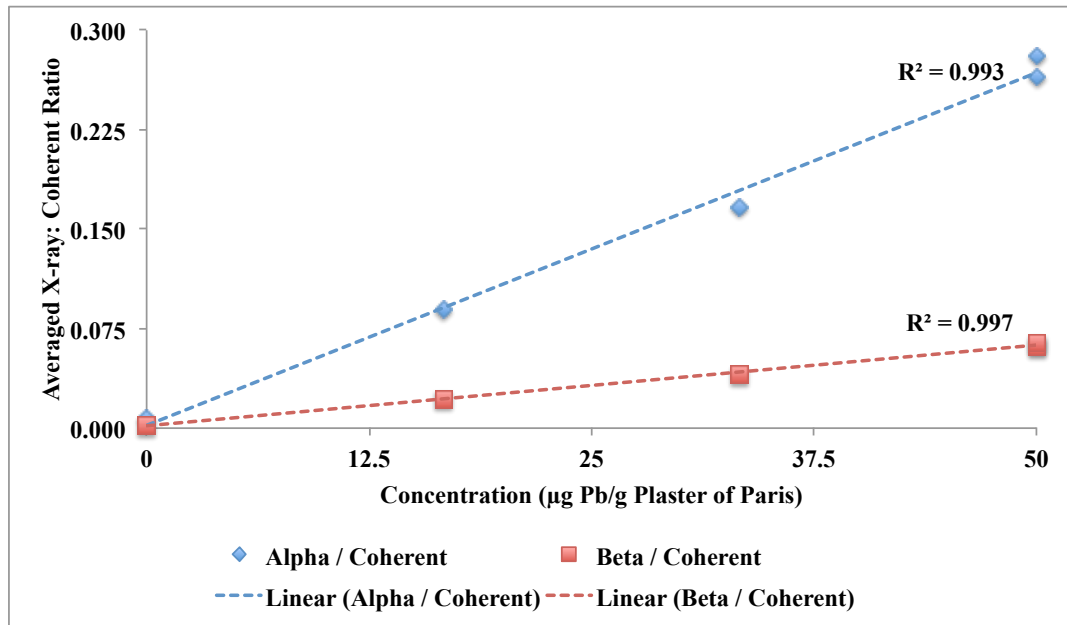
Figure 3.17: The averaged x-ray:coherent ratio versus average Pb concentration.

Figure 3.18: The Kα/coherent amplitude ratio across 7 positions for 2 phantoms with the identical mass of Pb and Plaster of Paris (3 'bones' of 50 ppm; 1 'bone' of 150 ppm and 2 'bones' of 0 ppm). By using the inverse-variance weighting method, the mean Kα x-ray to coherent ratio of '3 bones' of 50 ppm is 0.280 ± 0.037, whereas the mean Kα x-ray to coherent ratio of 1 'bone' of 150 ppm and 2 'bones' of 0 ppm is 0.265 ± 0.223. Although the variation in Kα x-ray to coherent ratio is greater across the more heterogenous phantom, the mean estimate is the same to within uncertainties.

Figure 3.19: The Kβ/coherent amplitude ratio across 7 positions for 2 phantoms with the identical mass of Pb and Plaster of Par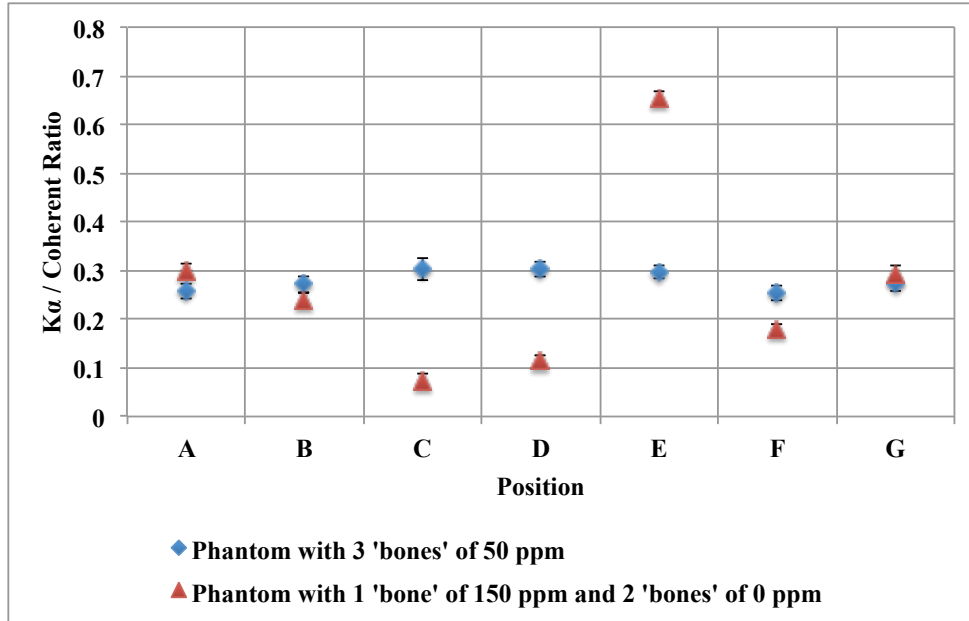is (3 'bones' of 50 ppm; 1 'bone' of 150 ppm and 2 'bones' of 0 ppm). By using the inverse-variance weighting method, the mean Kβ x-ray to coherent ratio of '3 bones' of 50 ppm is 0.062 ± 0.008, whereas the mean Kβ x-ray to coherent ratio of 1 'bone' of 150 ppm and 2 'bones' of 0 ppm is 0.065 ± 0.0049. As with the Kα ratio, although the variation in Kβ x-ray to coherent ratio is greater across the more heterogenous phantom, the mean estimate is the same to within uncertainties.
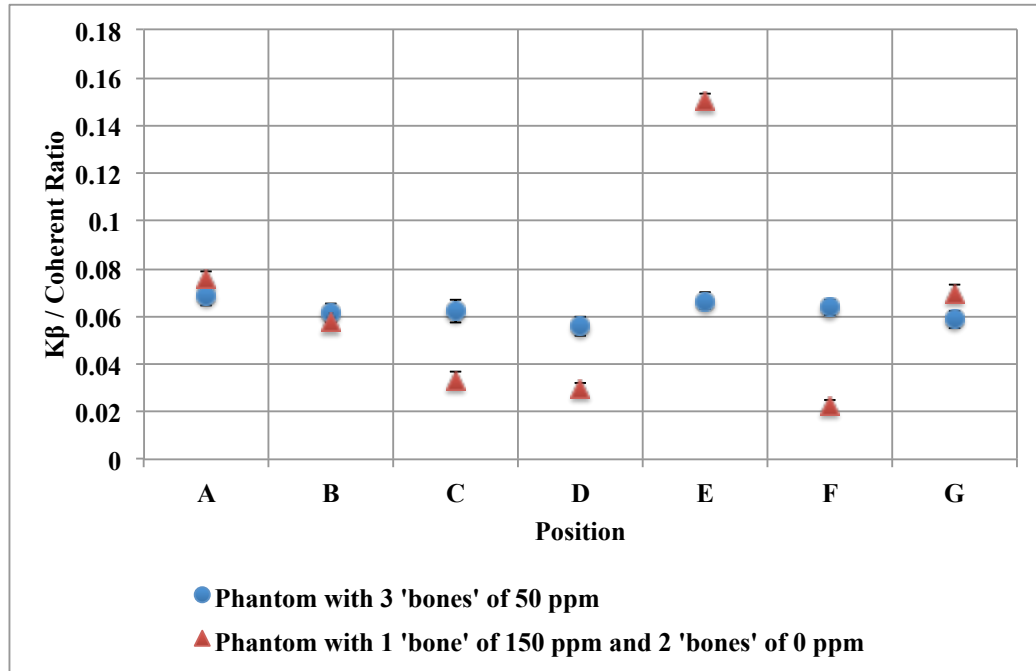
Figure 3.20: The Kα/coherent amplitude ratio across 7 positions for 2 phantoms one with 33.3% of the mass of Pb of the other but the same mass of Plaster of Paris (1 'bone' of 150 ppm and 2 'bones' of 0 ppm; 1 'bone' of 50 ppm and 2 'bones' of 0 ppm). By using the inverse-variance weighting method, the mean Kα x-ray to coherent ratio of 1 'bone' of 150 ppm and 2 'bones' of 0 ppm is 0.265 ± 0.223, whereas the mean Kα x-ray to coherent ratio of 1 'bone' of 50 ppm and 2 'bones' of 0 ppm is 0.090 ± 0.074.
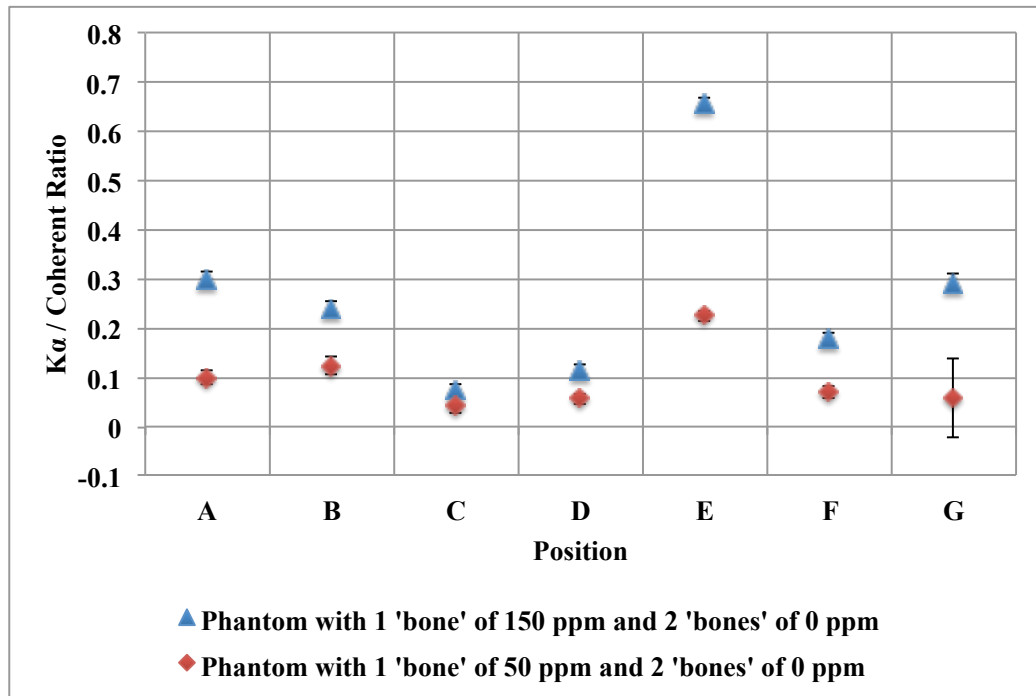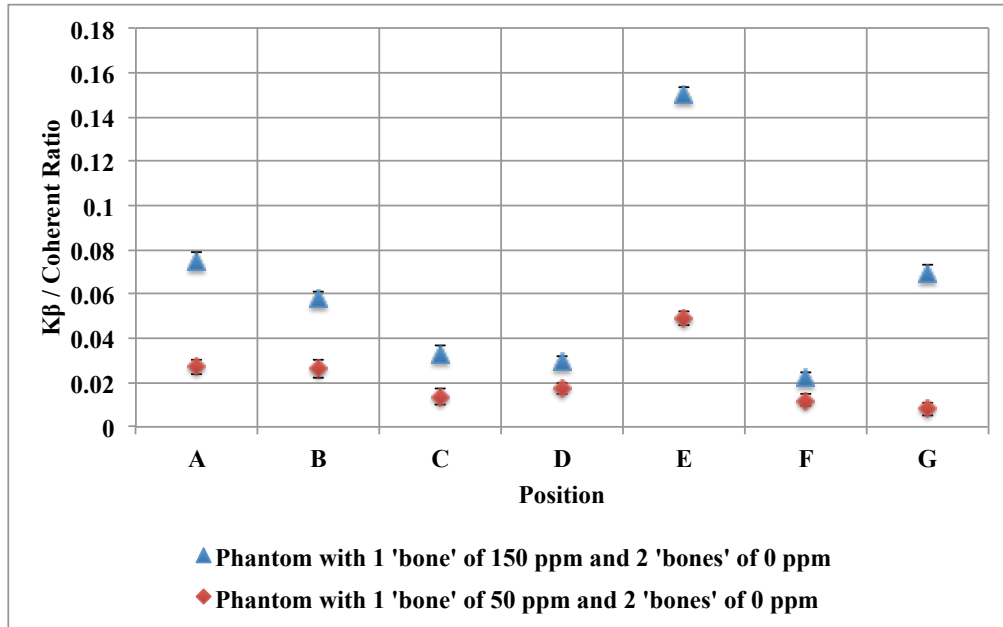
Figure 3.21: The Kβ/coherent amplitude ratio across 7 positions for 2 phantoms one with 33.3% of the mass of Pb of the other but the same mass of Plaster of Paris (1 'bone' of 150 ppm and 2 'bones' of 0 ppm; 1 'bone' of 50 ppm and 2 'bones' of 0 ppm). By using the inverse-variance weighting method, the mean Kβ x-ray to coherent ratio of 1 'bone' of 150 ppm and 2 'bones' of 0 ppm is 0.065 ± 0.049, whereas the mean Kβ x-ray to coherent ratio of 1 'bone' of 50 ppm and 2 'bones' of 0 ppm is 0.022 ± 0.015.

3.6.1 Effect of Variation in Pb Distribution Across the Mouse

The series of figures and tables presented so far in this chapter illustrate the effect of the variation in Pb distribution across the mouse. The patterns of data are those that would be expected from the distribution and geometry of the detector and phantom. For example, as shown in Figure 3.18, the Kα/coherent amplitude ratios across 7 positions for 2 phantoms with the same average Pb concentration but different Pb distribution (3 'bones' of 50 ppm and 1 'bone' of 150 ppm and 2 'bones' of 0 ppm) do vary from each other. In the phantom with 1 'bone' of 150 ppm and 2 'bones' of 0 ppm phantom, Position E has

the highest Kα/coherent amplitude ratio when compared to the signal obtained from all other phantom positions. This is because in Position E the ppm 'bone' was positioned close to the detector while the 0 ppm 'bones' were positioned further away from detectors (in position D and position F) (Figure 3.15). As there is a large Pb concentration of 'bone' in only one 'bone' in the phantom, close to the detector, geometric factors mean that the measured Kα/coherent amplitude ratio is large compared to instances when this large concentration 'bone' is in different orientations in the phantom with reference to the detector. In that same figure, it can be seen that there are only relatively small fluctuations in the ratio as the phantom with 3 'bones' of 50 ppm is turned. This phantom is of course symmetric and so the variation in signal would be expected to be less.

3.6.2 Applicability of the Normalization in Mice

This is clear when looking at data from Table 3.8B and Table 3.12B. The mean Kα x-ray to coherent ratio when measuring 3 'bones' of 50 ppm is 0.280 with a standard deviation of these 7 numbers of 0.037. The mean Kα x-ray to coherent ratio when measuring 1 'bone' of 150 ppm and 2 'bones' of 0 ppm is 0.265 with a standard deviation of 0.223. The mean Kα x-ray to coherent ratio is the same to within uncertainties, 0.280 versus 0.265, while the standard deviation is six times larger, 0.037 versus 0.223. These data suggest confirmation of our assumption: the mean phantom measurement is accurate if a sample is measured in multiple orientations. However, the uncertainty on that mean is larger due to sampled volume effects.

3.7 Conclusion

I have measured five mouse-mimicking PoP phantoms to evaluate the feasibility of accurate measurement of Pb in the skeleton of whole mice when Pb is heterogeneously distributed. My results suggest that our ^{109}Cd XRF system can measure Pb accurately in whole mice in vivo even if Pb is not distributed homogenously in the skeleton. As long as mice are measured in multiple orientations (i.e. rotated) during the measurement, the estimate of the mean bone Pb level in whole mice should be accurate. Distribution of Pb, will, however, increase the uncertainty in the estimate of Pb content.

CHAPTER 4

Conclusion

4.1 Conclusion for MDLs for Pre-existing Bone Pb Phantoms and Pb Free Mice

The MDLs for pre-existing bone Pb phantoms and Pb free mice were investigated. A set of pre-existing bone Pb phantoms was first measured to obtain the calibration lines. MDL was calculated and found to be 1.52 ppm for 1-hour measurement. This value indicated the lowest Pb concentration that our XRF cloverleaf system can detect. In order to verify whether our system is applicable to detect Pb contents in whole mice in vivo, 2 strains of Pb free mice were measured. In a 3-hour measurement, MDLs of 5.66 − 7.78 ppm and 6.69 − 8.50 ppm were determined in whole mice (CD-1 and C57BL/6J) with skull and hind facing the detector respectively.

4.2 Conclusion for Mouse-mimicking Bone Pb Phantoms

Five mouse-mimicking bone Pb phantoms were made to investigate the feasibility of accurate measurement of Pb in the skeleton of whole mice. My results found that the average x-ray:coherent ratios (for both α and β x-ray lines) are independent of Pb distribution. A linear regression of the average α:coherent ratio versus average concentration results in an R^2 value of 0.993 (p=0.0002) while linear regression of the average β:coherent ratio versus average concentration results in an R^2 value of 0.997 (p=0.0001). This suggested that our [109]Cd XRF system can measure Pb accurately in whole mice in vivo even if Pb is not distributed homogenously in the skeleton. The

estimate of the mean bone Pb level in whole mice should be accurate for multiple measurements in different orientations (i.e. rotated).

4.3 Future Work

In the first work, further investigations could be conducted to improve the MDLs of 2 strains of Pb free mice. In this study, we measured mice in two orientations (skull and hind) in 3-hour duration. Overnight XRF measurements and multiple orientations in mice are required to confirm this hypothesis. In addition, since the concentrations of the pre-existing bone Pb phantoms has not yet precisely confirmed, further analysis methods need to be used to solve this problem.

In the second work, Monte Carlo simulation is required to confirm the detection of lead in mouse-mimicking bone phantoms using in vivo XRF system. This further investigation involves collaboration with Joanna Nguyen and Dr. James Gräfe from Ryerson University and is currently undergoing data analysis.

Besides, XRF measurements of lead doped mice should also be considered. A trial measurement could be taken at the end stage of the Pb expsoure, after the lead-doped mice are sacrificed. This could provide us detailed information about whether our XRF system could measure the Pb content in real mice, and whether the lead-doping experiment is feasible not damaging mouse's metabolism. Previous research studies showed that female rats were exposed chronically to lead acetate via the drinking water

(0.5, 5, 50 and 250 ppm) from weaning through mating, gestation, and lactation (Kimmel et al., 1976). Even though all female rats estrous cycles and pregnancy rates were normal, the offspring from the 50 and 250 ppm groups weighed less at weaning and showed a latency in physical development. Reiter et al., 1975 also observed similar developmental delays in rat offspring exposed to 50 ppm lead in drinking water throughout gestation and lactation. However, the relationship between delays in development and lead on the nervous system of the offspring or reflect secondary changes such as malnutrition or hormonal imbalance is still unknown (Damstra, 1977). CD-1 mouse was also used in previous lead-doping studies (2 to 10 mg lead acetate/ml in drinking water at weaning), however, there was no observable changes in neurotransmitter metabolism in mouse brain (Silbergeld et al., 1975).

In our trial measurement, we may expose mice in 0, 10 and 50 mg lead acetate/ml in drinking water for 3 weeks to assess the feasibilities of in vivo XRF measurement of Pb in bone and MRI measurement of demyelination in brain. After verifying the possibilities in detecting Pb in bone in mice using XRF system and observing demyelination in brain using MRI system, second stage of measurements could be taken. The XRF measurements could be scheduled at every 2 or 3 weeks throughout Pb exposure, where the mice are anesthetized for 3 hours every time.

BIBLIOGRAPHY

[1] Agency for Toxic Substances and Disease Registry (ATSDR). Syracuse Research Corporation. *Toxicological profile for lead*. Agency for Toxic Substances and Disease Registry, Syracuse Research Corporation, 1990.

[2] Araki, Shunichi, and Tetsuo Honma. "Relationships between lead absorption and peripheral nerve conduction velocities in lead workers." Scandinavian journal of work, environment & health (1976): 225-231.

[3] Aro, A. C. A., et al. "Improvements in the calibration of 109Cd K x-ray fluorescence systems for measuring bone lead in vivo." Physics in Medicine & Biology 39.12 (1994): 2263.

[4] Anderson, A. C. "Pathophysiology of lead poisoning." *Lead poisoning in children* (1996).

[5] Bamford, S., et al. "Application of X-ray fluorescence techniques for the determination of hazardous and essential trace elements in environmental and biological materials." *Nukleonika* 49.3 (2004): 87-95.

[6] Beckhoff, Burkhard, et al., eds. *Handbook of practical X-ray fluorescence analysis*. Springer Science & Business Media, 2007.

[7] Behinaein, Sepideh, et al. "The estimation of the rates of lead exchange between body compartments of smelter employees." *Environmental Science: Processes & Impacts* 16.7 (2014): 1705-1715.

[8] Behinaein, S., et al. "Age and sex influence on bone and blood lead concentrations in a cohort of the general population living in Toronto." Physiological measurement 38.3 (2017): 431.

[9] Bevington, Philip R., et al. "Data reduction and error analysis for the physical sciences." *Computers in Physics* 7.4 (1993): 415-416.

[10] Bloch, P., et al. "Assessment of lead exposure of children from K-XRF measurements of shed teeth." *Applied radiation and isotopes* 49.5-6 (1998): 703-705.

[11] Bordo, Bianca M., et al. "Electrophysiological study of subjects occupationally exposed to lead and with low levels of lead poisoning." Scandinavian journal of work, environment & health (1982): 142-147.

[12] Börjesson, J., et al. "In vivo XRF analysis of mercury: the relation between concentrations in the kidney and the urine." *Physics in Medicine & Biology* 40.3 (1995): 413.

[13] Börjesson, J., et al. "In vivo measurements of lead in fingerbone in active and retired lead smelters." International archives of occupational and environmental health 69.2 (1996): 97-105.

[14] Bressler, Joseph P., and Gary W. Goldstein. "Mechanisms of lead neurotoxicity." *Biochemical pharmacology* 41.4 (1991): 479-484.

[15] Bressler, Joseph, Sheila Forman, and Gary W. Goldstein. "Phospholipid metabolism in neural microvascular endothelial cells after exposure to lead in vitro." Toxicology and applied pharmacology 126.2 (1994): 352-360.

[16] Bressler, Joseph, et al. "Molecular mechanisms of lead neurotoxicity." *Neurochemical research* 24.4 (1999): 595-600.

[17] Buchthal, F., and F. Behse. "Electrophysiology and nerve biopsy in men exposed to lead." Occupational and Environmental Medicine 36.2 (1979): 135-147.

[18] Bushnik, Tracey, et al. "Lead and bisphenol A concentrations in the Canadian population." Health Reports 21.3 (2010): 7.

[19] Caldwell, Kathleen L., et al. "Measurement challenges at low blood lead levels." Pediatrics (2017): e20170272.

[20] Canada. Health Canada. Final human health state of the science report on lead. Health Canada, 2013.

[21] Canfield, Richard L., et al. "Intellectual impairment in children with blood lead concentrations below 10 μg per deciliter." *New England journal of medicine* 348.16 (2003): 1517-1526.

[22] Carvalho, M. L., et al. "Analysis of human teeth and bones from the chalcolithic period by X-ray spectrometry." *Nuclear Instruments and Methods in Physics Research Section B: Beam Interactions with Materials and Atoms* 168.4 (2000): 559-565.

[23] Cecil, Kim M., et al. "Decreased brain volume in adults with childhood lead exposure." PLoS medicine 5.5 (2008): e112.

[24] Centers for Disease Control and Prevention. "Low level lead exposure harms children: a renewed call for primary prevention." Report to the CDCP (2012): 1-54.

[25] Cesareo, Roberto. *X-Ray Fluorescence Spectrometry*. Wiley-VCH Verlag GmbH & Co. KGaA, 2010.

[26] Clinical Laboratory Improvement Amendments (CLIA) of 1988. Pub. I. No. 100-578; 102 Stat 2903, 10 USC §263a.

[27] Chettle, D. R., M. C. Scott, and L. J. Somervaille. "Lead in bone: sampling and quantitation using K X-rays excited by 109Cd." *Environmental health perspectives* 91 (1991): 49.

[28] Chettle, D. R. "Three decades of in vivo x-ray fluorescence of lead in bone." X-Ray Spectrometry: An International Journal 34.5 (2005): 446-450.

[29] Christoffersson, J. O., et al. "Lead in finger-bone analysed in vivo in active and retired lead workers." American journal of industrial medicine 6.6 (1984): 447-457.

[30] Christoffersson, Jan Ove, et al. "Decrease of skeletal lead levels in man after end of occupational exposure." *Archives of Environmental Health: An International Journal* 41.5 (1986): 312-318.

[31] Cory-Schlecta, D. A., and H. H. Schaumburg. "Lead, inorganic." *Experimental and clinical neurotoxicology* 2 (2000): 708-20.

[32] Cory-Slechta DA and Pound JG. Lead neurotoxicity, in: L.W. Chang, R.S. Dyer Eds.., Handbook of Neurotoxicology, Chap. 2, Marcel Dekker, New York. (1995): 61–89.

[33] Damstra, Terri. "Toxicological properties of lead." Environmental health perspectives 19 (1977): 297.

[34] Danford, Darla Erhard. "Pica and nutrition." *Annual Review of Nutrition* 2.1 (1982): 303-322.

[35] Eltayeb, M., and R. Van Grieken. "Preconcentration and XRF-determination of heavy metals in hair from Sudanese populations." *Journal of radioanalytical and nuclear chemistry* 131.2 (1989): 331-342.

[36] Finkelstein, Yoram, Morri E. Markowitz, and John F. Rosen. "Low-level lead-induced neurotoxicity in children: an update on central nervous system effects." Brain Research Reviews 27.2 (1998): 168-176.

[37] Fleming, D. E., et al. "Accumulated body burden and endogenous release of lead in employees of a lead smelter." Environmental Health Perspectives 105.2 (1997): 224.

[38] Fleming, David EB, and Chris S. Ware. "Portable x-ray fluorescence for the analysis of chromium in nail and nail clippings." *Applied Radiation and Isotopes* 121 (2017): 91-95.

[39] Flora, Gagan, Deepesh Gupta, and Archana Tiwari. "Toxicity of lead: a review with recent updates." *Interdisciplinary toxicology* 5.2 (2012): 47-58.

[40] Gamblin, Carol, et al. "In vivo measurements of bone lead content in residents of southern Ontario." Applied radiation and isotopes 45.10 (1994): 1035-1038.

[41] Gerhardsson, L., et al. "In vivo measurements of lead in bone in long-term exposed lead smelter workers." *Archives of Environmental Health: An International Journal* 48.3 (1993): 147-156.

[42] Gerhardsson, Lars, et al. "Lead concentrations in cortical and trabecular bones in deceased smelter workers." Journal of Trace Elements in Medicine and Biology 19.2-3 (2005): 209-215.

[43] Gilbert, Steven G., and Bernard Weiss. "A rationale for lowering the blood lead action level from 10 to 2 µg/dL." *Neurotoxic* µg/dL *ology* 27.5 (2006): 693-701.

[44] Goldstein, G. W. "Evidence that lead acts as a calcium substitute in second messenger metabolism." Neurotoxicology 14.2-3 (1993): 97-101.

[45] Gordon, C. L., D. R. Chettle, and C. E. Webber. "An improved instrument for the in vivo detection of lead in bone." *Occupational and Environmental Medicine* 50.7 (1993): 637-641.

[46] Harvey, Birt. "Managing elevated blood lead levels among young children: Recommendations from the Advisory Committee on Childhood Lead Poisoning Prevention." *Atlanta, GA: Centers for Disease Control and Prevention* (2002).

[47] Hawkins, Brian T., and Thomas P. Davis. "The blood-brain barrier/neurovascular unit in health and disease." Pharmacological reviews 57.2 (2005): 173-185.

[48] Helene, Otaviano AM, et al. "Update of X-ray and Gamma-ray Decay Data Standards for Detector Calibration and Other Applications." *International Atomic Energy Agency: Vienna* (2007): 210.

[49] Hu, Howard. "Bone lead as a new biologic marker of lead dose: recent findings and implications for public health." *Environmental Health Perspectives* 106.Suppl 4 (1998): 961.

[50] IARC Working Group on the Evaluation of Carcinogenic Risks to Humans, World Health Organization, and International Agency for Research on Cancer. Inorganic and organic lead compounds. IARC, 2006.

[51] Ishihara, Kumatoshi, et al. "Ontogenically related properties of N-methyl-D-aspartate receptors in rat hippocampal neurons and the age-specific sensitivity of developing neurons to lead." Journal of Pharmacology and Experimental Therapeutics 273.3 (1995): 1459-1470.

[52] Jarup, Lars. "Hazards of heavy metal contamination." *British medical bulletin* 68.1 (2003): 167-182.

[53] Jusko, Todd A., et al. "Blood lead concentrations< 10 µg/dL and child intelligence at 6 years of age." *Environmental health perspectives* 116.2 (2008): 243.

[54] Kalra, Veena, et al. "Blood lead levels and risk factors for lead toxicity in children from schools and an urban slum in Delhi." *Journal of tropical pediatrics* 49.2 (2003): 121-123.

[55] Kimmel, C. A., Grant, L. D., and Sloan, C. S. Chronic lead exposure: assessment of developmental toxicity. Abstr. Teratol. Soc., Carmel, 1976.

[56] Knoll, Glenn F. *Radiation detection and measurement*. John Wiley & Sons, 2010.

[57] Kolmogorov, Yuriy, Valentina Kovaleva, and Alexandr Gonchar. "Analysis of trace elements in scalp hair of healthy people, hyperplasia and breast cancer patients with XRF method." *Nuclear Instruments and Methods in Physics Research Section A: Accelerators, Spectrometers, Detectors and Associated Equipment* 448.1-2 (2000): 457-460.

[58] Kumar, Suresh, et al. "Encephalopthy due to Inorganic Lead Exposure in an Adult." Japanese journal of medicine 26.2 (1987): 253-254.

[59]Landrigan, Philip J., and Andrew C. Todd. "Lead poisoning." Western Journal of Medicine 161.2 (1994): 153.

[60]Lanphear, Bruce P., et al. "Low-level environmental lead exposure and children's intellectual function: an international pooled analysis." *Environmental health perspectives* 113.7 (2005): 894.

[61]Lead, WHO Inorganic. "Environmental health criteria 165." *International Programme on Chemical Safety. Geneva: World Health Organization* (1995).

[62]Lead, WHO Inorganic. "Lead poisoning and health." *Fact Sheet, 379. Geneva: World Health Organization* (2015).

[63]Leggett, Richard W. "An age-specific kinetic model of lead metabolism in humans." *Environmental Health Perspectives*101.7 (1993): 598.

[64]Lidsky, Theodore I., and Jay S. Schneider. "Lead neurotoxicity in children: basic mechanisms and clinical correlates." *Brain*126.1 (2003): 5-19.

[65]Lohiya, Ghan Shyam, and Sunita Lohiya. "Lead poisoning in a radiator repairer." *Western journal of medicine* 162.2 (1995): 160.

[66]Lord, M. L., et al. "A phantom-based feasibility study for detection of gadolinium in bone in-vivo using X-ray fluorescence." Applied Radiation and Isotopes 112 (2016): 103-109.

[67]Mahaffey, Kathryn R. "Nutritional factors in lead poisoning." *Nutrition reviews* 39.10 (1981): 353-362.

[68]Mani, Jayanti, et al. "Cerebellar ataxia due to lead encephalopathy in an adult." Journal of Neurology, Neurosurgery & Psychiatry 65.5 (1998): 797-798.

[69]Mann, Thaddeus, Cecilia Lutwak Mann, and Robert L. Dixon. "Passage of chemicals into human and animal semen: mechanisms and significance." *CRC Critical Reviews in Toxicology* 11.1 (1982): 1-14.

[70]Mason, Lisa H., Jordan P. Harp, and Dong Y. Han. "Pb neurotoxicity: neuropsychological effects of lead toxicity." BioMed research international 2014 (2014).

[71]Markowitz, Morri. "Lead poisoning: a disease for the next millennium." *Current problems in pediatrics* 30.3 (2000): 62-70.

[72]Markovac, Jasna, and Gary W. Goldstein. "Picomolar concentrations of lead stimulate brain protein kinase C." Nature 334.6177 (1988): 71.

[73] McNeill, F. E., et al. "The decrease in population bone lead levels in Canada between 1993 and 2010 as assessed by in vivo XRF." *Physiological measurement* 39.1 (2017): 015005.

[74] McNeill, Fiona E., et al. "109Cd K x ray fluorescence measurements of tibial lead content in young adults exposed to lead in early childhood." Occupational and environmental medicine 57.7 (2000): 465-471.

[75]Menke, Andy, et al. "Blood lead below 0.48 µmol/L (10 µg/dL) and mortality among US adults." *Circulation* 114.13 (2006): 1388-1394.

[76]Navas-Acien, Ana, et al. "Lead exposure and cardiovascular disease—a systematic review." *Environmental health perspectives* 115.3 (2007): 472.

[77]Nie, Huiling. *The Improvement of In vivo XRF Lead Measurement System*. M.Sc. Diss. 2001.

[78]Nilsson, U., et al. "Kinetics of lead in bone and blood after end of occupational exposure." Pharmacology & toxicology 68.6 (1991): 477-484.

[79]O'Flaherty, Ellen J. "A physiologically based kinetic model for lead in children and adults." *Environmental health perspectives* 106.Suppl 6 (1998): 1495.

[80]Paltridge, Nicholas G., et al. "Energy-dispersive X-ray fluorescence analysis of zinc and iron concentration in rice and pearl millet grain." *Plant and soil* 361.1-2 (2012): 251-260.

[81] Papanikolaou, Nikolas C., et al. "Lead toxicity update. A brief review." Medical science monitor 11.10 (2005): RA329-RA336.

[82] Parsons, Patrick J., and Walter Slavin. "A rapid Zeeman graphite furnace atomic absorption spectrometric method for the determination of lead in blood." Spectrochimica Acta Part B: Atomic Spectroscopy 48.6-7 (1993): 925-939.

[83] Parsons, Patrick J., Andrew A. Reilly, and Debra Esernio-Jenssen. "Screening children exposed to lead: an assessment of the capillary blood lead fingerstick test." Clinical chemistry 43.2 (1997): 302-311.

[84] Parsons, P. J., et al. "Analytical Procedures for the Determination of Lead in Blood and Urine; Proposed Guidelines." Analytical Procedures for the Determination of Lead in Blood and Urine; Proposed Guidelines C40-P 18.Analytical Procedures for the Determination of Lead in Blood and Urine; Proposed Guidelines C40-P (1998).

[85] Parsons, Patrick J., Ciaran Geraghty, and Mary Frances Verostek. "An assessment of contemporary atomic spectroscopic techniques for the determination of lead in blood and urine matrices." Spectrochimica Acta Part B: Atomic Spectroscopy 56.9 (2001): 1593-1604.

[86] Pearce, J. M. S. "Burton's line in lead poisoning." *European neurology* 57.2 (2007): 118-119.

[87] Petit, Ted L., Janelle C. LeBoutillier, and William J. Brooks. "Altered sensitivity to NMDA following developmental lead exposure in rats." Physiology & behavior 52.4 (1992): 687-693.

[88] Potts, P. J. "X-ray fluorescence analysis: principles and practice of wavelength dispersive spectrometry." *A Handbook of Silicate Rock Analysis*. Springer, Dordrecht, 1987. 226-285.

[89] Persidsky, Yuri, et al. "Blood–brain barrier: structural components and function under physiologic and pathologic conditions." Journal of Neuroimmune Pharmacology 1.3 (2006): 223-236.

[90] Price, John, et al. "Repeated bone lead levels in Queensland, Australia—previously a high lead environment." Archives of Environmental Health: An International Journal 47.4 (1992): 256-262.

[91] Rao, Janapareddy Vijaya Bhaskara, et al. "Lead encephalopathy in adults." Journal of neurosciences in rural practice 5.2 (2014): 161.

[92] Rasmussen, Pat E., et al. "Canadian House Dust Study: Population-based concentrations, loads and loading rates of arsenic, cadmium, chromium, copper, nickel, lead, and zinc inside urban homes." *Science of the Total Environment* 443 (2013): 520-529.

[93] Rastogi, Suresh Chandra, and Jørgen Clausen. "Absorption of lead through the skin." Toxicology 6.3 (1976): 371-376.

[94] Reiter, Lawrence W., et al. "Developmental and behavioral changes in the rat during chronic exposure to lead." Environmental Health Perspectives 12 (1975): 119.

[95] Repko, J. D., et al. Effects of inorganic lead on behavioral and neurologic function, January 1978. Technical report (Final). No. PB-91-108126/XAB; DHEW/PUB/NIOSH--78-128. Arizona Univ., Tucson, AZ (USA). Dept. of Family and Community Medicine, 1978.

[96] Roy, M. M., et al. "Further experience with bone lead content measurements in residents of southern Ontario." Applied radiation and isotopes 48.3 (1997): 391-396.

[97] Sanders, Talia, et al. "Neurotoxic effects and biomarkers of lead exposure: a review." Reviews on environmental health 24.1 (2009): 15-46.

[98] Schütz, Andrejs, et al. "Lead in vertebral bone biopsies from active and retired lead workers." Archives of Environmental Health: An International Journal 42.6 (1987): 340-346.

[99] Schwartz, Joel, Carol Angle, and Hugh Pitcher. "Relationship between childhood blood lead levels and stature." *Pediatrics* 77.3 (1986): 281-288.

[100] Schwartz, Joel. "Low-level lead exposure and children′s IQ: a metaanalysis and search for a threshold." *Environmental research* 65.1 (1994): 42-55.

[101] Shenberg, Cesia, et al. "An XRF study of trace elements accumulation in kidneys of tumor-bearing mice after treatment withcis-DDP with and without selenite and selenocistamine." *Biological trace element research* 40.2 (1994): 137.

[102] Seppäläinen, Anna Maria, et al. "Subclinical neuropathy at "safe" levels of lead exposure." Archives of Environmental Health: An International Journal 30.4 (1975): 180-183.

[103] Seppäläinen, A. M., et al. "Early neurotoxic effects of occupational lead exposure: a prospective study." Neurotoxicology 4.2 (1983): 181-192.

[104] Shehab, H., et al. "Feasibility of measuring arsenic and selenium in human skin using in vivo x-ray fluorescence (XRF)—a comparison of methods." Physiological measurement 37.1 (2015): 145.

[105] Silbergeld, Ellen K., and A. M. Goldberg. "Pharmacological and neurochemical investigations of lead-induced hyperactivity." Neuropharmacology 14.5-6 (1975): 431-444.

[106] Singh, Surjit, et al. "Lead-induced peripheral neuropathy following Ayurvedic medication." (2009).

[107] Somervaille, Lillian J., David R. Chettle, and Malcolm C. Scott. "In vivo measurement of lead in bone using x-ray fluorescence." Physics in Medicine & Biology 30.9 (1985): 929.

[108] Stewart, W. F., et al. "Past adult lead exposure is linked to neurodegeneration measured by brain MRI." Neurology 66.10 (2006): 1476-1484.

[109] Taylor, Mark Patrick, et al. "Environmental lead exposure risks associated with children's outdoor playgrounds." *Environmental Pollution* 178 (2013): 447-454.

[110] Tchounwou, Paul B., et al. "Heavy metal toxicity and the environment." *Molecular, clinical and environmental toxicology*. Springer, Basel, 2012. 133-164.

[111] Todd, Andrew Christian, Fiona Ellane McNeill, and Bruce Andrew Fowler. "In vivo X-ray fluorescence of lead in bone." *Environmental research* 59.2 (1992): 326-335.

[112] Todd, Andrew C., and David R. Chettle. "In vivo X-ray fluorescence of lead in bone: review and current issues." *Environmental health perspectives* 102.2 (1994): 172.

[113] Todd, A. C., et al. "Predictors of DMSA chelatable lead, tibial lead, and blood lead in 802 Korean lead workers." Occupational and environmental medicine 58.2 (2001): 73-80.

[114] Tong, Shilu, Yasmin E. von Schirnding, and Tippawan Prapamontol. "Environmental lead exposure: a public health problem of global dimensions." *Bulletin of the World Health Organization* 78 (2000): 1068-1077.

[115] Toribara, T. Y. "Analysis of single hair by XRF discloses mercury intake." *Human & experimental toxicology* 20.4 (2001): 185-188.

[116] Tüzün, Meriç, et al. "Lead encephalopathy: CT and MR findings." Journal of computer assisted tomography 26.3 (2002): 479-481.

[117] Zaichick, V., N. Ovchjarenko, and S. Zaichick. "In vivo energy dispersive X-ray fluorescence for measuring the content of essential and toxic trace elements in teeth." *Applied radiation and isotopes* 50.2 (1999): 283-293.

[118] Zi-qiang, Chen, et al. "Peripheral nerve conduction velocity in workers occupationally exposed to lead." Scandinavian journal of work, environment & health (1985): 26-28.